Dirac-Weyl quasiparticles in external fields

I n a u g u r a l d i s s e r t a t i o n

zur

Erlangung des akademischen Grades eines

Doktors der Naturwissenschaften
(Dr. rer. nat.)

der

Mathematisch-Naturwissenschaftlichen Fakultät

der

Universität Greifswald

vorgelegt von

Alexander Filusch

Greifswald, 6. März 2023

Dekan: Prof. Dr. Gerald Kerth

1. Gutachter: Prof. Dr. Holger Fehske

2. Gutachter: Prof. Dr. Ulrich Zülicke

Tag der Promotion: 3. Juli 2023

Contents

1 Summary

1.1 Introduction

Since the discovery of graphene in 2004 [1], materials that feature Dirac-cone physics have been intensively studied because of their intriguing physical properties and potential in technological applications (see the various reviews [2–4]). Graphene is a strictly two-dimensional honeycomb lattice of carbon atoms whose low-energy charge-carrier dynamics obey the massless pseudospin-1/2 Dirac-Weyl equation (or chiral Weyl equation) where the chiral centers (or valleys) are the corners $\mathbf{K}$ and $\mathbf{K}'$ of the Brillouin zone. This linear energy spectrum near the Dirac nodal points lends graphene its exotic and ultra-relativistic properties, such as Klein Tunneling [5–7], anomalous quantum Hall effect [8], and the nonzero minimal conductivity [8–10].

Other examples of materials dominated by Dirac physics are the surface excitations of 3D topological insulators [11] and 3D Weyl semimetals [12]. However, condensed matter systems can possess fermionic excitations with linear dispersions that have no analog in high-energy physics because the energy dispersions are constrained by the crystal space group instead of the Poincare group. This permits the study of triply (multiply) degenerate fermions such as in 3D [13–15] or generalized pseudospin-s Dirac fermions in 2D [16]. Remarkably, such quasiparticles also possess strictly flat bands [17] (for a review on artificial flat bands, see Ref. [18]). Flat bands are bands of constant energy irrespective of the crystal momentum, implying that its charge carriers have zero group velocity (or infinite effective mass) and a singular density of states. In condensed matter systems, the charge carriers are then dominated by the electron-electron interaction, making flat bands ideal to study strongly-correlated many-body phenomena such as ferromagnetism [19, 20], superconductivity [17, 21] or the fractional quantum Hall effect [22, 23]. In this context, nearly flat bands have been studied in, e.g., magic-angle twisted bilayer graphene [24].

Historically perhaps the first example of such a system is the $\mathcal{T}_3$ or dice lattice [25–27], which is a honeycomb-like lattice with an additional atom C placed at the center of each hexagon and coupled to only one of the sublattices A or B [cf. Fig. 1]. The spectrum of the dice model consists of a strictly flat band that crosses the conical intersections of the two Dirac cones around the $\mathbf{K}$ and $\mathbf{K}'$ nodes inherited from graphene [cf. Fig. 1]. The chiral flat band exists due to the bipartiteness of the dice lattice and is therefore stable against perturbations of the transfer amplitudes [25, 28, 29]. The enlarged pseudospin-1 Dirac-Weyl equation describes the low-energy dynamics with striking consequences such as the super-Klein tunneling effect [30]. Although the flat band does not directly contribute to the transport, it renders the DC conductivity divergent [31] and causes unusual atomic collapse [32].

The scaling of the transfer amplitude of the additional atoms in the dice lattice with a parameter α results in the α-$\mathcal{T}_3$ lattice [cf. Fig. 1], which continuously interpolates between graphene (with a decoupled central site) and the dice lattice [33]. Of experimental relevance is the α-$\mathcal{T}_3$ lattice with intermediate $\alpha = 1/\sqrt{3}$ parameter, because it could be realized in $Hg_{1-x}Cd_xTe$ at a critical doping [33, 34]. Several suggestions have also been reported

for an optical α-$\mathcal{T}_3$ lattice that would allow tuning of α by dephasing one pair of the three counter-propagating laser beams [33, 34]. The dice lattice has also been realized in Josephson arrays [35].

In this thesis, we study the effect of external fields of Dirac-Weyl quasiparticles in α-$\mathcal{T}_3$ lattices by the tight-binding model

$$H_\alpha(t) = -\sum_{\langle ij \rangle} J_{ij}(t) a_i^\dagger b_j - \alpha \sum_{\langle ij \rangle} J_{ij}(t) c_i^\dagger b_j + \text{H.c.}, \tag{1}$$

where $a^{(\dagger)}$, $b^{(\dagger)}$, and $c^{(\dagger)}$ create (annihilate) a state centered on site A, B, and C, respectively. The transfer amplitudes that are shown in Tab. 1 incorporate the external fields. The precise controllability of Dirac-like materials lies at the heart of any technological application [36]. By applying external (static or time-dependent) electric fields via top gates or magnetic fields, local restrictions like junctions or barriers can be easily imprinted. Gate-induced quantum dots have attracted much interest in the pseudospin-1/2 and -1 case, because long-living temporally bound states emerge in the elastic [37, 38] or inelastic (driven) case [39]. Particularly, we demonstrated in an extension to my master thesis that the revival of resonant scattering and controlled forward-backward scattering is mutable in an oscillating dice-quantum dot by means of the oscillation frequency [40]. Subjected to external gauge fields, the α-dependent Berry phase and the flat band of the α-$\mathcal{T}_3$ lattice result in valley-contrasting Landau level quantization [33, 41], an unconventional quantum Hall effect [42, 43], and unusual Weiss oscillations [44] in the intermediate $0 < \alpha < 1$ regime. Particularly, the valley degree of freedom can be manipulated by the geometric valley Hall effect [45], the magnetic Fabry-Pérot interferometry [46], and the valley-polarized magnetoconductivity [44], crossed Andreev reflection [47]. Dirac-Weyl quasiparticles dressed by external irradiation can induce Floquet-topological phase transitions [48, 49]. In this
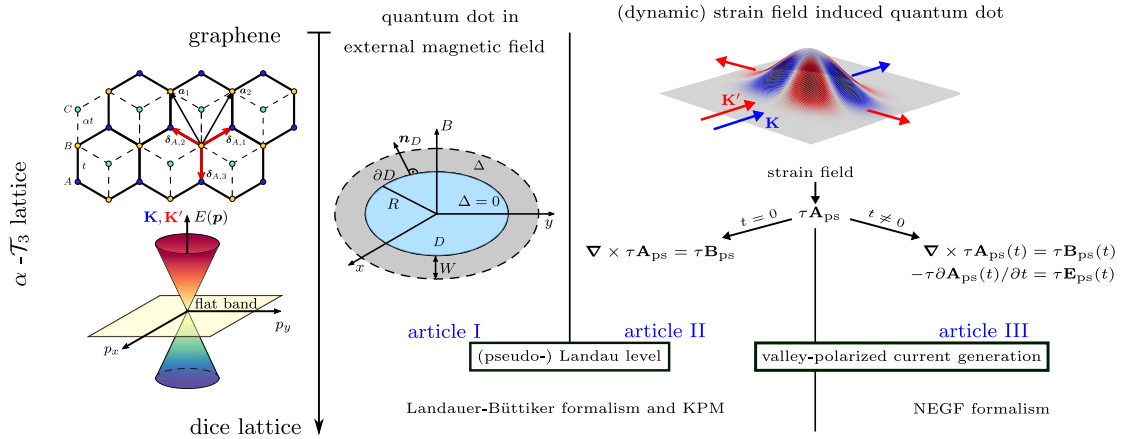

Fig. 1: Illustration of different quantum dot configurations on the α-$\mathcal{T}_3$ lattice under external magnetic or strain fields interpolating between graphene (decoupled flat band) or the dice lattice. External magnetic and strain fields quantize the energy spectrum into (pseudo-) Landau level. Quantum dots due to (dynamic) strain fields generate valley-polarized currents.

regard, the application of strain fields to graphene has remarkable consequences for its electronic and transport properties due to graphene's ability to withstand high degrees of deformation [50] and extraordinary electromechanical coupling. When deforming the honeycomb lattice, the overlap of the π-orbitals is modified, which impacts the electronic transfer amplitude. Electrons traversing the strained region effectively feel a pseudomagnetic

field (PMF) that can reach up to 300-800 T [51, 52], which is beyond the current limits for real magnetic fields in laboratory settings. As a consequence of the time-reversal symmetry, the induced PMF points in the opposite direction for electrons residing in the $\mathbf{K}$ and $\mathbf{K}'$ valley, which can be used to isolate specific valleys. This property is advantageous for the field of "valleytronics", where the valley degree of freedom is exploited to manipulate information [53–55]. Strain fields have been used to design various valleytronic devices like beam-splitters or filters [56–62].

Firstly, we study Dirac-Weyl quasiparticles in external magnetic fields and confined to circular quantum dots by opening an infinite gap outside the dot region. The energy eigenvalues in such an infinite-mass boundary condition are derived as a function of the scaling parameter. We implement a closed and open(contacted) α-$\mathcal{T}_3$ tight-binding lattice-model of the infinite-mass boundary and validate the low-energy solutions by numerical exact methods and probe the current-carrying states. Additionally, we probe the sensitivity of the eigenstates against local perturbations of the mass gap.

Secondly, we study static and dynamic deformations of the α-$\mathcal{T}_3$ lattices and show that this can generate and control valley-polarized currents. Beginning with static strain fields, we derive the pseudomagnetic fields and the pseudo-Landau levels in the low-energy continuum approximation. We investigate and assess the transmission through and valley polarization of a quantum dot imprinted by Gaussian bump deformations in a four-terminal Hall bar setup through its geometric parameters and the Fermi energy to find optimal valley-filtering conditions. Additional insight into the excited states and pseudo-Landau levels is obtained by the spatial variation of the local density of states. Furthermore, we show that an additional pseudoelectric field is induced by time-periodically driving the height of the Gaussian bump. To demonstrate the effects of such a drive, we classify the valley-filter capabilities of a α-$\mathcal{T}_3$ Hall bar within the Keldysh non-equilibrium Green's function formalism in different regimes by the geometric parameters and scaling parameter. We demonstrate that the pseudoelectric field is able to induce novel valley-filtering regimes and localized flat-band states that reach beyond the static case and are also mutable by the driving frequency. In particular, we investigate the spatial variation of the local current density inside the Gaussian bump for the different valley-filtering regimes.

Tab. 1: Comparison of the properties of the pseudo- and real magnetic field.

	magnetic field	pseudomagnetic field
TRS	✗	✓
transfer amplitude	$J \exp\left\{i2\pi/\Phi_0 \int_i^j \mathbf{A}(\mathbf{r})\,\mathrm{d}\mathbf{r}\right\}$	$J \exp\left\{-\beta(|\mathbf{r}_i' - \mathbf{r}_j'|/a - 1)\right\}$
$B_{\max}$	45.5 T [63]	300-800 T [52]
E	$\pm\hbar\omega_c\sqrt{n_\tau + \frac{1}{2}(1 - \tau\cos 2\varphi)}$	$\pm\hbar\omega_c\sqrt{n + \frac{1}{2}(1 + \mathrm{sgn}(B_{\mathrm{ps}})\cos(2\varphi))}$

1.2 Dirac-Weyl quasiparticles in magnetic fields

The electronic properties of quantum dots based on α-$\mathcal{T}_3$ lattices are frequently investigated in the massless Dirac-Weyl description to find the low-lying energy states in dependence of external perturbations such as magnetic fields. However, the analytical modeling of such nanostructures requires suitable boundary conditions beyond (simple) potential wells due to Klein tunneling [64] to spatially confine the Dirac-Weyl quasiparticles. Generally,

the presence of the edges or the precise edge configuration strongly perturbs the electron and hole states [65–68]. Perhaps the most widely used approach in graphene is the infinite-mass boundary condition (IMBC) first derived by Berry and Mondragon [69] for neutrino billiards in the pseudospin-1/2 case ($\alpha = 0$). In their proposal, a position- and sublattice-dependent on-site potential opens an effective mass gap in the spectrum outside the considered nanostructure, which cages Dirac-Weyl quasiparticles by creating perfectly reflecting boundaries. We give a brief overview of the application of the IMBC in α-$\mathcal{T}_3$ quantum dots to obtain the eigenstates of Dirac-Weyl quasiparticles under external magnetic fields before numerically verifying the solutions in closed and open (contacted) tight-binding lattice-model.

Quantum dot In article I in Sec. 2.2, we derived a generalized formulation of the IMBC for the α-$\mathcal{T}_3$ lattice around the **K** [$\tau = +1$] and **K**′ [$\tau = -1$] point,

$$\psi_{\tau,B} = i\tau \left(\cos \varphi \psi_{\tau,A} e^{i\tau\chi(\mathbf{r})} + \sin \varphi \psi_{\tau,C} e^{-i\tau\chi(\mathbf{r})} \right), \tag{2}$$

which relates the components of the wave function at the boundary. The normalized vector $\mathbf{n_r} = (\cos \chi(\mathbf{r}), \sin \chi(\mathbf{r}))$ perpendicular to the boundary inscribes the geometry.
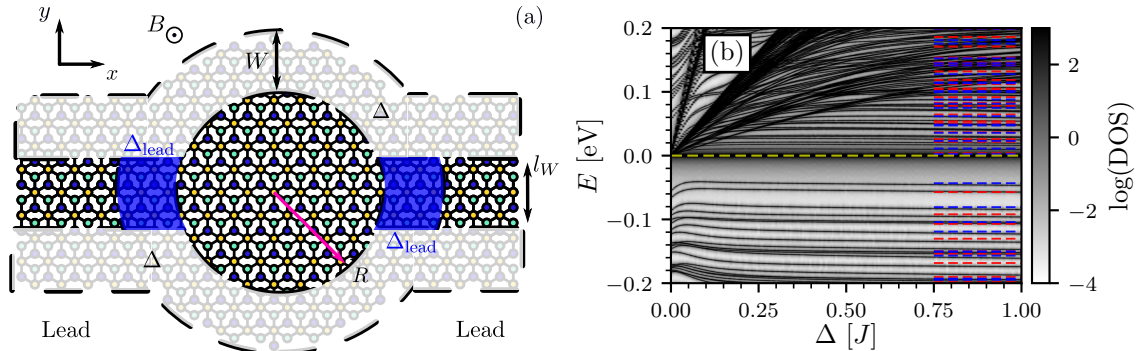

Fig. 2: (a) Depiction of an α-$\mathcal{T}_3$ quantum dot of radius R with perpendicular magnetic field B and contacted by leads of width l_W. The stripe of width W with sublattice-dependent on-site potential Δ realizes the infinite mass boundary condition. An additional mass term is placed at the lead/dot interface (blue) with strength Δ_{lead}. We use KWANT library [70] for numerical solving the tight-binding model. The used parameters are $R = 20$ nm, $W = 5$ nm and $l_W = 80\sqrt{3}a - 2W$. (b) Logarithmic density of states (black) of an isolated $1/\sqrt{3}$-$\mathcal{T}_3$ dot for $B = 2$ T as a function of the gap size Δ. Analytical solutions for $n_\rho = 1$, 2, and 3 and $-10 \leq m \leq 10$ are displayed as convergence check for $\tau = +1$ [blue dashed] and $\tau = -1$ [red dashed]. Flat bands are marked in yellow. (a) is adapted from article I.

For a simple application of the IMBC (2), we consider a circular quantum dot of radius R embedded in an infinite-mass region and subjected to a perpendicular magnetic field $\mathbf{B} = B\mathbf{e}_z$ that is related to the vector potential $\mathbf{A} = B/2(-y, x, 0)$. The Hamiltonian is given in polar coordinates by

$$H_\tau^\varphi = v_F \mathbf{S}_\tau^\varphi \cdot (\mathbf{p} + e\mathbf{A}) + \Delta U \Theta(r - R). \tag{3}$$

The detailed derivation of the eigenfunctions is given in article I Sec. 2.3. These read

$$\psi_{\tau,s}^D = N \begin{pmatrix} \tau \cos \varphi \rho^{-m+\tau} f_{\tau,A} e^{i(m-\tau)\phi} \\ i\varepsilon_\tau \rho^{-m} L_{n_\tau}^{-m}(\rho^2) e^{im\phi} \\ \tau \sin \varphi \rho^{-m-\tau} f_{\tau,C} e^{i(m+\tau)\phi} \end{pmatrix} e^{-\frac{\rho^2}{2}} \quad \psi_{\tau,0}^D = \begin{pmatrix} \sin \varphi \rho^{-m+\tau} f_{\tau,A} e^{i(m-\tau)\phi} \\ 0 \\ \cos \varphi \rho^{-m-\tau} f_{\tau,C} e^{i(m+\tau)\phi} \end{pmatrix} e^{-\frac{\rho^2}{2}}$$
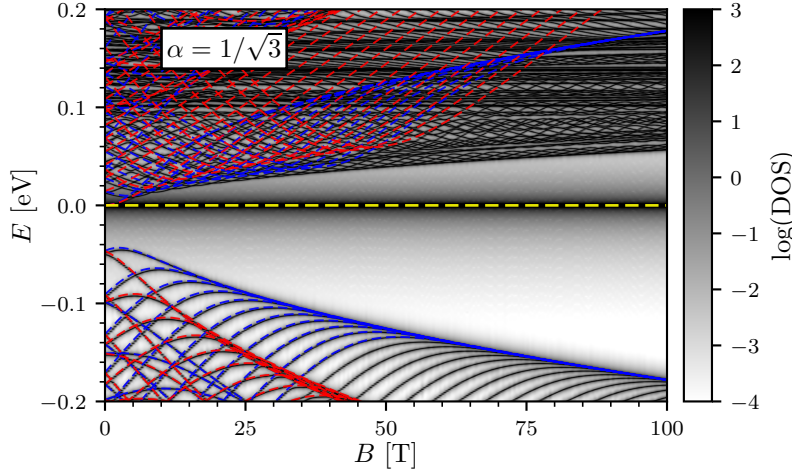
$$\tag{4}$$

Fig. 3: Logarithmic density of states (black) of an isolated $1/\sqrt{3}$-$\mathcal{T}_3$ dot ($\Delta_{\text{lead}} = \Delta$) in dependence of the external magnetic field. Analytical solutions for $n_\rho = 1$, 2, and 3 and $-10 \le m \le 10$ are incorporated for comparison with $\tau = +1$ [blue dashed] and $\tau = -1$ [red dashed], see article I. Flat bands are marked in yellow. Reproduced and adapted from article I.

for the dispersive states ($s = \text{sgn}(E)$) with normalization constant N and the flat band states, respectively. The $L_a^b(x)$ are the generalized Laguerre polynomials, and

$$f_{\tau,A} = \begin{cases} -L_{n_++1}^{-m+1}(\rho^2), & \text{if } \tau = +1 \\ (n_- + 1)L_{n_-+1}^{-m-1}(\rho^2), & \text{if } \tau = -1 \end{cases} \qquad f_{\tau,C} = f_{-\tau,A}. \qquad (5)$$

Due to the rotational symmetry, the eigenstates (and eigenvalues) are labeled by the angular momentum number m. Furthermore, we introduce the magnetic length $l_B = \sqrt{\hbar/eB}$ and the cyclotron energy $\hbar\omega_c = \sqrt{2}\hbar v_F/l_B$ to employ dimensionless units $\rho = r/l_B$ and $\epsilon_\tau = E_{\tau,s}/\hbar\omega_c$. The application of the IMBC (2) at the boundary $r = R$ with $\mathbf{n_r} = (\cos\phi, \sin\phi)$ yields for the dispersive states with $n_\tau = \epsilon_\tau^2 + (\tau\cos 2\varphi - 1)/2$

$$0 = \begin{cases} -\cos^2\varphi\rho^2 L_{n_++1}^{-m+1}(\rho^2) + \sin^2\varphi(n_+ + 1)L_{n_++1}^{-m-1}(\rho^2) - \varepsilon_+\rho L_{n_+}^{-m}(\rho) \Big|_{\rho=R/\sqrt{2}l_B} & \text{if } \tau = 1 \\ \cos^2\varphi(n_- + 1)L_{n_-+1}^{-m-1}(\rho^2) - \sin^2\varphi\rho^2 L_{n_--1}^{-m+1}(\rho^2) - \varepsilon_-\rho L_{n_-}^{-m}(\rho) \Big|_{\rho=R/\sqrt{2}l_B} & \text{if } \tau = -1 \end{cases} , \qquad (6)$$

where the zeros of these equations determine the energy eigenvalues $E_{\tau,sn_\rho,m}$ around $\tau = \pm$ with $n_\rho = 1$, 2, 3... as the radial quantum number. For $\alpha = 0$, Eq. (6) reduces to the conditional equation previously derived for graphene by replacing $m \to m - 1$ [71–73]. The flat-band states trivially fulfill the boundary condition and persist unperturbed.

The analytical results for the magnetic field dependence of the energy eigenvalues of Dirac-Weyl quasiparticles in isolated dots are presented in Fig. 2 of article I for several α values. Let us briefly summarize the main results of energy eigenvalues in the continuum approximation. As reported in Refs. [71–73] for $\alpha = 0$, the spectra is particle-hole anti-symmetric and $E_\tau = E_{-\tau}$ for $B > 0$. For intermediate scaling parameters ($0 < \alpha < 1$), we find a valley-anisotropy spectrum, i.e., $E_\tau \ne -E_{-\tau}$ when $B > 0$ due to the broken inversion and time-reversal symmetry. In the dice lattice ($\alpha = 1$), the spectra are valley-degenerate for any B. Additionally, we have a four-fold degeneracy since $E_m = E_{-m}$ when $B = 0$. Interestingly, the flat-band states are unperturbed by the IMBC and the time-reversal symmetry breaking due to the magnetic field since the anti-$\mathcal{PT}$ symmetry is intact [29]. As detailed derived in article I, the eigenvalues in the limit of large ρ, i.e., large radii or

5

Fig. 4: Conductance of the contacted $1/\sqrt{3}$-$\mathcal{T}_3$ quantum dot with $B = 2$ T and $\Delta_{\text{lead}} = 0.2$ eV. Blue [red] lines mark the analytical solution for $\tau = +1$ [$\tau = -1$], respectively. For details, see article I. Adapted from article I.
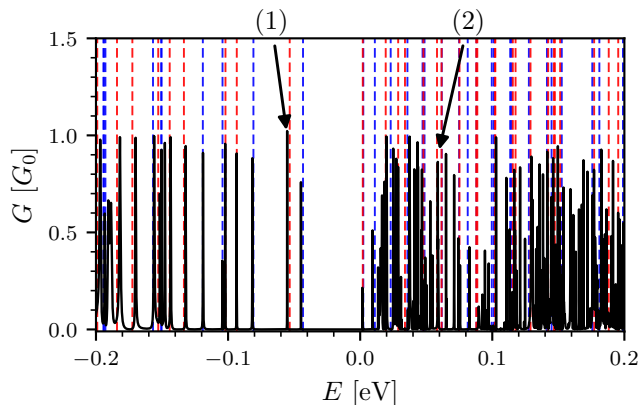
magnetic fields, converge to the Landau levels (LLs) of the α-$\mathcal{T}_3$ lattice [33],

$$E_{\tau,s,n_\tau} = \hbar\omega_c\sqrt{n_\tau + \frac{1}{2}(1 - \tau\cos 2\varphi)}, \qquad (7)$$

as expected. Note that the prominent valley-degeneracy present in graphene is lifted for intermediate scaling parameters ($0 < \alpha < 1$) due to the α-dependent Berry phase [33].

Numerical verification   We model the quantum dot of Fig. 2(a) by the tight-binding model

$$H_{\text{dot}} = H_\alpha + \Delta \sum_{i\in\text{stripe}} \left(a_i^\dagger a_i - b_i^\dagger b_i + c_i^\dagger c_i\right) + \Delta_{\text{lead}} \sum_{i\in\text{lead}} \left(a_i^\dagger a_i - b_i^\dagger b_i + c_i^\dagger c_i\right), \qquad (8)$$

where H_α describes the Hamiltonian of the α-$\mathcal{T}_3$ lattice from Eq. (1) in the magnetic field **B** via the Peierls substitution, $J_{ij} = J\exp\{i\Phi_{ij}\}$, with $\Phi_{ij} = 2\pi/\Phi_0 \int_i^j \mathbf{A}(\mathbf{r})\,d\mathbf{r}$. The sums in the sublattice-dependent on-site potentials Δ and Δ_{lead} are taken over the sheath (white) and lead (blue) parts of width W denoted in Fig. 2(a), respectively, which implement the IMBC by opening a gap of 2Δ in the band structure at the charge neutrality point. To accurately implement the IMBC, we have to approximate the infinite region of infinite mass in Eq. (3) with a finite W and Δ in the numerical implementation of the IMBC region [cf. Fig. 3(a)]. We take $W = 5$ nm to accurately represent a continuum outside the dot region. Throughout this work, we assume $\Delta > 0$ since the $\Delta < 0$ case can be obtained by reversing the sign of the energy. Note, that the on-site potential also shifts the flat band to the bottom of the conduction band, $E = \Delta$, in the sheath region.

Before comparing the full B-dependence of the isolated dot to the continuum solution, we perform a convergence check by obtaining the density of states (DOS) via the kernel polynomial method [74] of the isolated $1/\sqrt{3}$-$\mathcal{T}_3$ lattice quantum dot, i.e. $\Delta_{\text{lead}} = \Delta$ (disconnected leads), as a function of Δ [cf. Fig. 2(b)] at fixed $B = 2$ T. For very small Δ, the finite sheath region around the dot does not act as IMBC, because $\Delta < E$. Recalling the derivation of the IMBC in article I, the wave function outside the dot region decays exponentially perpendicular to the boundary when $\Delta > E$, i.e., $\psi^{\text{II}} \propto \exp(-k_\perp r)$ for $r > R$. Since stripe W is finite ($W = 5$ nm) in the numerical tight-binding model, convergence to the continuum eigenvalues cannot be reached when the wave function is not sufficiently decayed due to too small Δ. Above a threshold $\Delta \gtrsim 0.75$ eV, the DOS peaks match the continuum solution, especially for $E < 0$. Therefore we take $\Delta = 0.8$ eV throughout.

The results depend on the choice W: a larger width W could allow for smaller Δ but increases the computational demand. For positive energies, we notice an additional band of states emerging from the flat band. We will show below, that these are edge states at the infinite-mass boundary.

In the following, we exemplarily examine and compare the DOS with the analytical eigenvalue spectra in Fig. 3, where we take $\Delta = 0.8$ eV. Clearly, the continuum model yields an extremely accurate approximation of the numerical data for $E < 0$. More DOS values develop for $E < 0$ because the tight-binding model inherently involves additional, larger angular momenta than those considered in the continuum eigenvalues spectrum. Drastic differences appear however for positive energies (and $\alpha > 0$), where we observe a band of additional states that are related to the on-site potential Δ and are located at the boundary of the dot [see below]. As detailedly shown in article I, these observations are valid for any $\alpha > 0$; the band of states is absent in graphene dots, and its width scales with α.
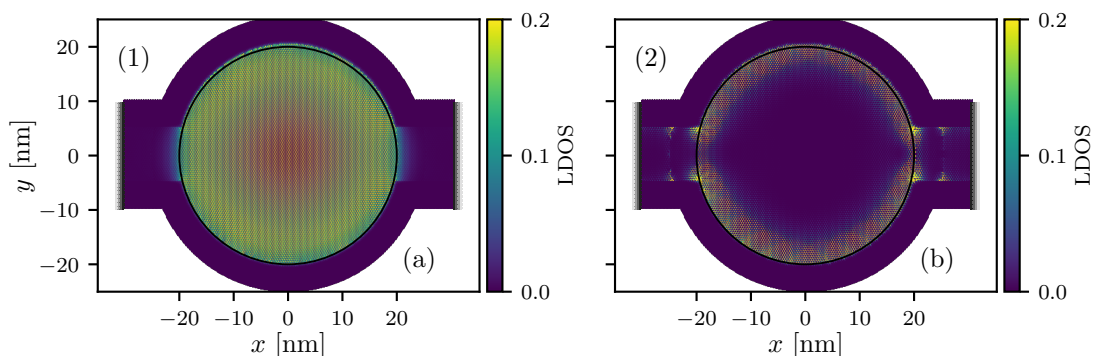

Fig. 5: LDOS of the contacted $1/\sqrt{3}$-$\mathcal{T}_3$ dot at energies marked by (1) and (2) in Fig. 4 in (a) and (b), respectively. The dashed line denotes the boundary of the quantum dot. Adapted from article I.

A perhaps more realistic situation is an open dot geometry, i.e., connecting leads to the dot region[see Fig. 2(a)]. To (partially) restore the rotational symmetry, we add lead barriers of $\Delta_{\text{lead}} = 0.2$ eV [cf. Fig. 2(a) blue region]. In the Landauer-Büttiker formalism, we obtain the differential conductance G and the local DOS (LDOS) by the python-based toolbox KWANT library [70]. For numerical details on the taken parameters and quantities, see Sec. 3.2 of article I. The conductance is proportional to the transmission and probes the extended, i.e., current-carrying states inside the dot. In Fig. 4, the conductance calculations are shown for a weak magnetic field of $B = 2$ T. For verification of the large-field case, see the discussion on Fig. 5 and Fig. 7 in article I. Again, we can accurately assign the resonances of the conductance to the analytical eigenvalues of the isolated dot for $E < 0$ as in Fig. 3(b), while we notice additional peaks in the positive energy range. The flat band with vanishing group velocity is absent in the conductance [cf. Fig. 4] because it does not carry any current.

We investigate these different transport channels by examining the spatial distribution of the LDOS for resonance (1) and (2) [see Fig. 5(a) and (b)] in the dot region. The LDOS of resonance (1) is a (nearly) rotational-symmetric bulk state corresponding to the analytical solution with quantum numbers $m = 0$, $sn_\rho = -1$, and $\tau = -1$. This is in agreement with the corresponding eigenfunction [see Eq. (4)]. For resonance (2), the situation is much different. Here, the incoming electrons are mainly transmitted along the boundary of the dot, which is not related to any bulk states from the IMBC. The origin of these "anomalous" edge states lies in the two regions of different flat-band positions: inside the dot region, the flat band is located at $E = 0$, while it is located at $E = \Delta$ outside the dot [75]

A short note on the use of the lead barrier: As demonstrated in Fig. 7 of article I, several conductance resonances are smeared out into hybridized bands and cannot be identified with the
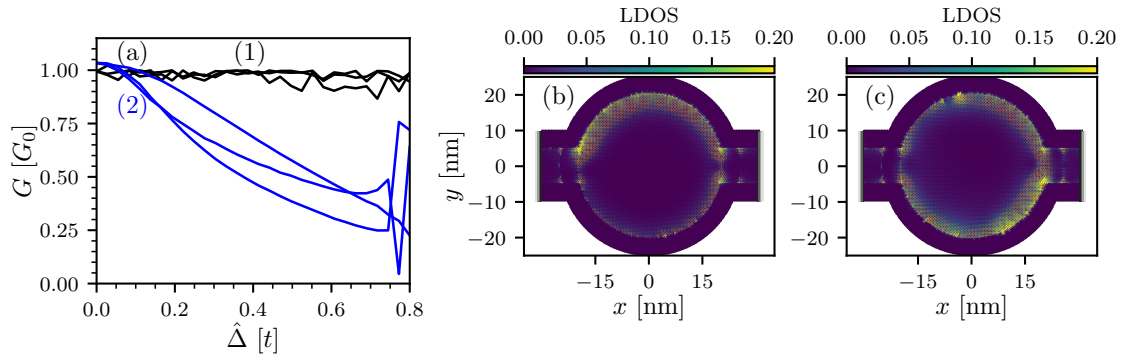
Fig. 6: (a) Conductance for the resonances (1) [black curves] and (2) [blue curves] as a function of disorder strength $\hat{\Delta}$ for three (typical) realizations. All other parameters remain as in Fig. 2. (b)(c) LDOS of the disordered $1/\sqrt{3}$-$\mathcal{T}_3$ quantum dot for the (shifted) energy (2) in Fig. 4 at disorder strength $\hat{\Delta} = 0.8t$. Adapted and extended from article I.

analytical solutions when $\Delta_{\text{Lead}} = 0$ because the attached leads break the rotational symmetry. Although $\Delta_{\text{Lead}} \neq 0$ but $\Delta \gg \Delta_{\text{Lead}}$ leads to only evanescent waves entering the quantum-dot region and suppressing the conductance resonances when $E < \Delta_{\text{Lead}}$, but the rotational symmetry is (partially) restored and the conductance resonances are assignable to their quantum numbers.

Moreover, we demonstrated in Fig. 5 and Fig. 7 of article I that the DOS and the conductance are quantized in steps of the Landau levels for large magnetic fields for every α, as predicted. The quantized quantum Hall plateaus will collapse, however, when the cyclotron diameter $d_c = 2|E|/v_{\text{F}}eB$ exceeds the lead width l_W because the electrons—moving in skipping orbits along the boundary– will pass over the right lead.

Lastly, we introduce imperfections to the IMBC by randomizing $\Delta \rightarrow \Delta_i$ in Eq. (8) where Δ_i is assumed to be evenly distributed in the interval $[\Delta - \hat{\Delta}, \Delta + \hat{\Delta}]$ and $\Delta > \hat{\Delta}$ such that $\hat{\Delta}$ gives the disorder strength. Figure 6 depicts the conductance of the (shifted) resonances (1) and (2) while continuously increasing $\hat{\Delta} = 0 \rightarrow 0.8$ for three (typical) disorder realizations. The local imperfections of the IMBC shift the resonance position due to the large local differences in the on-site energies, which modify the effective radius of the dot and the width of the sheath. While the transmission of the bulk state resonance (1) is only marginally affected by the edge disorder, scattering along the boundary notably reduces the conductance of the "edge state" (2). When $\hat{\Delta} \rightarrow 0.8t$, however, the conductance can be (partially) restored, which correlates with the local distribution of the LDOS on the dot boundary. In this case, the LDOS is spread on both (top and bottom) half of the dot [cf. Fig. 6(b) and Fig. 6(c)] and $G/G_0 > 0.5$. When $G/G_0 < 0.5$, only the top or bottom half of the dot boundary is populated [cf. Fig. 9 in article I]. This suggests that each half of the dot supports half of a transport channel. The disordered IMBC facilitates electron puddles on the boundary, which reduces the conductance by trapping the traversing electrons [cf. Fig. 6(b) and (c)]. It would be promising for future works to obtain the probability distributions for the LDOS and conductance from an ensemble of disorder realizations to pinpoint these observations.

In summary, we found good agreement between the analytical spectrum obtained by the IMBC and the numerical implementation on the α-$\mathcal{T}_3$ lattice in open and closed setups. However, deviations of the numerical results occurred for energies far away from the neutrality point and for positive energies due to lattice effects. Furthermore, the valley-anisotropic properties of the Dirac-Weyl quasiparticles under external magnetic fields suggest that α-$\mathcal{T}_3$ lattices are promising candidates for valleytronic applications.

1.3 Dirac-Weyl quasiparticles in strain fields

Deformations of α-$\mathcal{T}_3$ lattice by strain fields $\mathbf{u}(x, y, t) = [u_x, u_y, u_z \equiv h(x, y, t)]$ modify the site positions $\mathbf{r}_i'(t) = \mathbf{r}_i + \mathbf{u}(\mathbf{r})$ of the α-$\mathcal{T}_3$ lattice and, thereby, alter the bond lengths $d_{ij}(t) = |\mathbf{r}_i'(t) - \mathbf{r}_j'(t)|$ between nearest neighbors and changes the overlap of the π-orbitals, which is estimated by [76]

$$J_{ij}(t) = J \exp\{-\beta(d_{ij}(t)/a - 1)\}, \tag{9}$$

where $\beta = -\partial \ln J / \partial \ln a$ is the electron Grüneisen parameter. The effects of such deformations on the electronic properties of graphene ($\alpha = 0$ limit) are described in terms of valley-dependent pseudo-gauge fields [77]. The associated pseudomagnetic field (PMF) has been exploited to spatially divide electrons from the $\mathbf{K}$ and $\mathbf{K}'$ valleys in order to generate valley-polarized currents [59]. These properties motivated us to study the interplay of the valley-contrasting Dirac-Weyl quasiparticles in α-$\mathcal{T}_3$ lattices with strain-induced pseudo-gauge fields which could offer a pathway towards new valleytronic applications. We start by showing that strain induces pseudo-gauge fields for Dirac-Weyl quasiparticles in the more general case of α-$\mathcal{T}_3$ lattices and derive the pseudo-Landau levels (pseudo-LL) for a simple static strain.
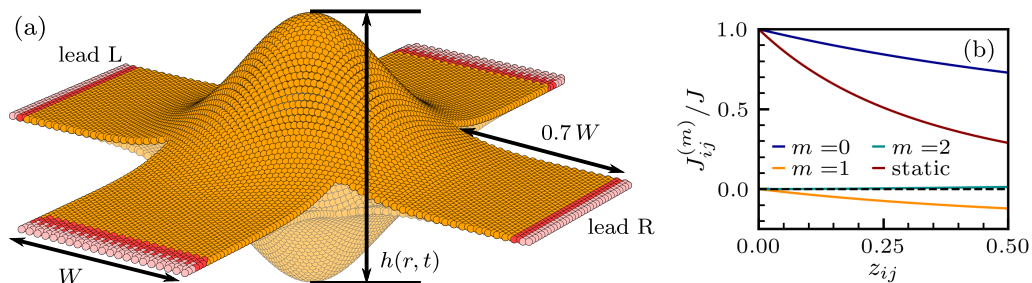

Fig. 7: (a) Hall-bar setup with four terminals based on the α-$\mathcal{T}_3$ lattice with a static/dynamic Gaussian bump (17) at the center. Leads attached to the Hall-bar region are described by the pristine tight-binding Hamiltonian in Eq. (1) with $J_{ij} = J = 2.8$ eV. (b) Fourier components of the time-dependent transfer amplitudes for realistic values of z_{ij} and $m = 0, 1, 2$. The transfer amplitude of the static bump is also shown. Adapted from article III.

Pseudo-electromagnetic fields Within the Cauchy-Born approximation and since real deformations do not involve rigid-body rotations, the strained nearest-neighbor vectors are given by [77, 78]

$$\boldsymbol{\delta}'_{A/B,i} = \boldsymbol{\delta}_{A/B,i} + \underline{\epsilon} \cdot \boldsymbol{\delta}_{A/B,i}, \tag{10}$$

where

$$(\underline{\epsilon})_{ij} = \frac{(\partial_i u_j + \partial_j u_i)}{2} + (\partial_i h)(\partial_j h), \qquad i, j = x, y \tag{11}$$

is the strain tensor and the vectors $\boldsymbol{\delta}_{A/B,i}$ are defined in article II. For small strains, we expand the strained transfer-amplitudes up to linear order in $\underline{\epsilon}$ since the tight-binding model (1) depend solely on the nearest-neighbor distances:

$$J_{ij} = J \exp\{-\beta(|\boldsymbol{\delta}_{A/B,i} + \underline{\epsilon} \cdot \boldsymbol{\delta}_{A/B,i}|/a - 1)\} \approx J(1 - \frac{\beta}{a^2} \boldsymbol{\delta}_{A/B,i} \underline{\epsilon} \, \boldsymbol{\delta}_{A/B,i}). \tag{12}$$

After inserting this expression in the Fourier-transformed Hamiltonian in Eq. (1) of article II, we find around $\mathbf{K}$ and $\mathbf{K}'$:

$$H_\tau^\varphi = \hbar v_{\mathrm{F}} \mathbf{S}_\tau^\varphi \cdot \left(\mathbf{q} + \tau \frac{e}{\hbar} \mathbf{A}_{\mathrm{ps}} \right), \tag{13}$$

with $v_{\mathrm{F}} = 3at/2\hbar$, $\mathbf{q} = -i\boldsymbol{\nabla}$, and

$$\mathbf{A}_{\mathrm{ps}} = -\frac{\hbar\beta}{2a}\begin{pmatrix}\epsilon_{xx} - \epsilon_{yy} \\ -2\epsilon_{xy}\end{pmatrix} \tag{14}$$

is the strain-induced vector potential. At first sight, the $\mathbf{q}$-space Hamiltonian in Eq. (13) appears to be formally equivalent to the Dirac-Weyl quasiparticles coupled to an external magnetic field, see Eq. (19) in article I. However, this strain-induced vector potential is not equivalent to a real vector potential associated with an electromagnetic field since it explicitly depends on the valley quantum number τ. This crucial difference arises, because strain fields are, unlike real magnetic fields, time-reversal symmetric. Consequently, the artificial (pseudo-) gauge field induces pseudomagnetic and pseudoelectric fields (PMFs and PEFs):

$$B_{\mathrm{ps}} = (\boldsymbol{\nabla} \times \mathbf{A}_{\mathrm{ps}})_z\,, \qquad\qquad \mathbf{E}_{\mathrm{ps}} = -\frac{\partial}{\partial t}\mathbf{A}_{\mathrm{ps}}. \tag{15}$$

The main influence of PMFs can be obtained by considering a spatially uniform PMF with corresponding pseudo-gauge field $\mathbf{A}_{\mathrm{ps}} = -\tau\gamma B_{\mathrm{ps}}y\mathbf{e}_x$ due to a static triaxial strain [79] and deriving the pseudo-LL, focusing on the scaling parameter α, field direction $\gamma = \pm 1$ and the valley number τ. This yields (for details, see Eq. (13) in article II) [80]

$$E_{\tau,\gamma} = \pm\hbar\omega_c\sqrt{n + \frac{1}{2}(1 + \gamma\cos(2\varphi))}. \tag{16}$$

In comparison to the LL from Eq. (7) induced by a real magnetic field, the sign γ in Eq. (16) takes over the role of the valley quantum number, i.e., $\gamma = -\tau$, which makes the pseudo-LL in Eq. (16) valley-degenerate as a consequence of the time-reversal symmetry. The flat band of the α-$\mathcal{T}_3$ lattice remains unperturbed for any strain configuration, just as the LL from magnetic fields.
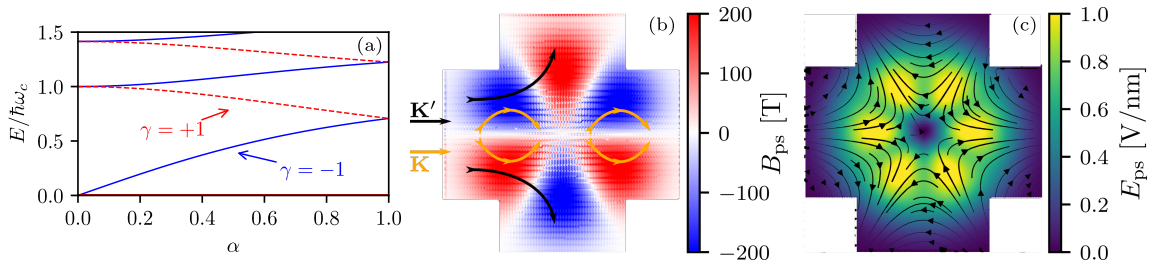

Fig. 8: (a) Pseudo-LL as a function of scaling parameter α for $n = 0, 1, 2$ and $\gamma = \pm 1$. (b) (Zoomed-in) Pseudomagnetic field induced by static Gaussian bump with $h_0 = 17.9$ nm and $\sigma = 20$ nm centered in a Hall bar of width $W = 50$ nm for electrons around the $\mathbf{K}$-valley. (Zoomed-in) Pseudoelectric field induced by an oscillating Gaussian bump centered in a Hall bar setup [see Fig. 7(a)] of width $W = 20$ nm with $h_0 = 8$ nm, $\sigma = 10$ nm, and $\Omega = 0.25\,J$ at $t = T/8$ for electrons in the $\mathbf{K}$-valley. The pseudoelectromagnetic fields for electrons residing in the $\mathbf{K}'$ valley are obtained by reversing the signs. Figure (b) and (c) are modified from article III

Setup Out-of-plane deformations like Gaussian bumps or folds are particularly interesting because valleytronic devices such as valley filters or beam splitters can be constructed by utilizing the valley-dependent pseudoelectromagnetic fields [56, 57, 61, 62, 79]. Here, we consider static ($\Omega t = 0$) or dynamic Gaussian bumps $\mathbf{u} = h(r,t)\mathbf{e}_z$ of height h_0 and width σ on the α-$\mathcal{T}_3$ lattice displayed in Fig. 7(a) with

$$h(r,t) = h_0\cos(\Omega t)\exp\left(-r^2/\sigma^2\right), \tag{17}$$

where T is the oscillation period, i.e. $h(r, t+T) = h(r,t)$, and $\Omega = 2\pi/T$ the corresponding frequency. This deformation induces a pseudoelectromagnetic vector potential $\mathbf{A}_{\mathrm{ps}} = (\mathrm{Re}A_{\mathrm{ps}}, \mathrm{Im}A_{\mathrm{ps}})$ given

by [81–83]

$$A_{\mathrm{ps}} = \frac{1}{ev_{\mathrm{F}}} \sum_{j=1}^{3} J_{ij}(t) e^{-i\mathbf{K}\cdot(\mathbf{r}'_i - \mathbf{r}'_j)}, \tag{18}$$

where **K** is a corner of the Brillouin zone. For the analytical PMF, see Eq. (17) in article II . Figure 8(a) and (b) display the local course of the PMF and PEF, which were obtained by Eq. (15) for electrons located in the **K**-valley. For **K′**, the PMF and PEF are obtained by reversing the signs. We briefly outline how this could potentially valley-filter incoming electrons [see Fig. 8(b)] in the four-terminal Hall-bar setup shown in Fig. 7(a). Injected valley-degenerate electrons from the left lead [cf. Fig. 7(a)] feel the opposite PMF, which pushes the **K** electrons to the center of the Gaussian bump while the **K′** electrons—feeling the reversed PMF—are scattered in the perpendicular direction and are collected by the leads at the top and bottom [59]. Hence, the outgoing stream of electrons at the right lead is effectively valley-filtered, as we will show below. To probe the valleytronic properties, we take the left (L) and right (R) lead in zigzag orientation since the **K** and **K′** valley can be identified with negative and positive momenta in this case, respectively.

Note that the valley selection does not depend on exciting valley-polarized states inside the Gaussian bump since the pseudo-LLs (16) are degenerate in the valley degree of freedom τ. Instead, the symmetry-breaking of the incoming electron stream from the left lead selects the **K**-valley. An incoming valley-degenerate current from the top or bottom lead will be split into three streams of valley-polarized electrons, which would require a different lead setup for detection [84, 85].

Valley-polarized current generation by static Gaussian bumps   We now turn to α-$\mathcal{T}_3$ quantum dots inscribed by static Gaussian bumps (17) [$\Omega t = 0$] and focus on the transport properties and the requirements for the valley-polarized current generation in a four-terminal Hall bar setup with $W = 50$ nm. We inspect the conductance G proportional to the transmission and valley polarization $\tau^{[\mathbf{K}]} = G^{[\mathbf{K}]}/G$ between the left (L) and right lead (R) [cf. Fig. 7(a)[(b)]] obtained using the KWANT library [70] based on the tight-binding model (1) for geometric parameters. The transfer amplitudes are given in Fig. 7(b) as a function of the squared nearest-neighbor distances, see Eq.(4) in article III. We define the valley polarization as the probability of an injected, valley-degenerate electron in the left lead to be transferred into any mode belonging to the **K** valley in the right lead weighted by the total conductance. Further insight into excited states inside the quantum dot is gained by the spatial distribution of the local density of states (LDOS). For further numerical details, refer to article II.

We assess the valley-polarization properties of the strain-induced quantum dots by studying three representative configurations of the Gaussian bump corresponding to low, high, or medium PMF inside the Hall bar region. We take $(h_0, \sigma) = (5, 20)$ nm, $(h_0, \sigma) = (17.9, 16)$ nm, and $(h_0, \sigma) = (17.9, 20)$ nm belonging, respectively, to the regime I, II, and III of Fig. 3(a) in article II. For regime I, we observe a finite conductance above a small gap of around $E_{\mathrm{F}} \simeq 0.04$ eV due to the barrier induced by the small PMF for combination $(h_0, \sigma) = (5, 20)$ nm. For larger energies, the conductance is (nearly) unperturbed and much higher compared to regimes II and III due to the weak field. Nevertheless, valley filtering is possible in a small window around $E_{\mathrm{F}} = 0.1$ eV. Beyond this point, the valley polarization decays to $\tau^{\mathbf{K}} \simeq 0.5$ because the weak PMF is unable to divert the **K′** electrons from the right lead [cf. Fig. 9(b)]. For the combination of $(h_0, \sigma) = (17.9, 16)$ nm, we observe that the conductance is significantly suppressed compared to the previous case [cf. Fig. 9(a)], because most electrons traversing by the Gaussian bump are blocked due to the exceedingly high PMF. However, a small amount of **K′** electrons is still able to circumvent the repulsive PMF barrier and pass to the right lead, thereby inducing a $\tau^{[\mathbf{K}']}$ polarization [cf. Fig. 9(b)].

We now turn to the valley-filtering regime III of the parameter space [see Fig. 3(a) of article II], where we take $h_0 = 17.9$ nm with $\sigma = 20$ nm. Here, the system shows only a finite conductance above $E_{\mathrm{F}} \simeq 0.15$ eV, i.e., when the (Fermi) energy exceeds the effective barrier from the high PMF inside the quantum dot region [cf. Fig. 9(a)]. Beyond this threshold $E_{\mathrm{F}} \simeq 0.15$ eV, we find a band of resonances between (1) and (2) [grey dots], and around (3), where each band displays nearly perfect valley polarization. Here, incoming electrons are excited to pseudo-LL subbands of different
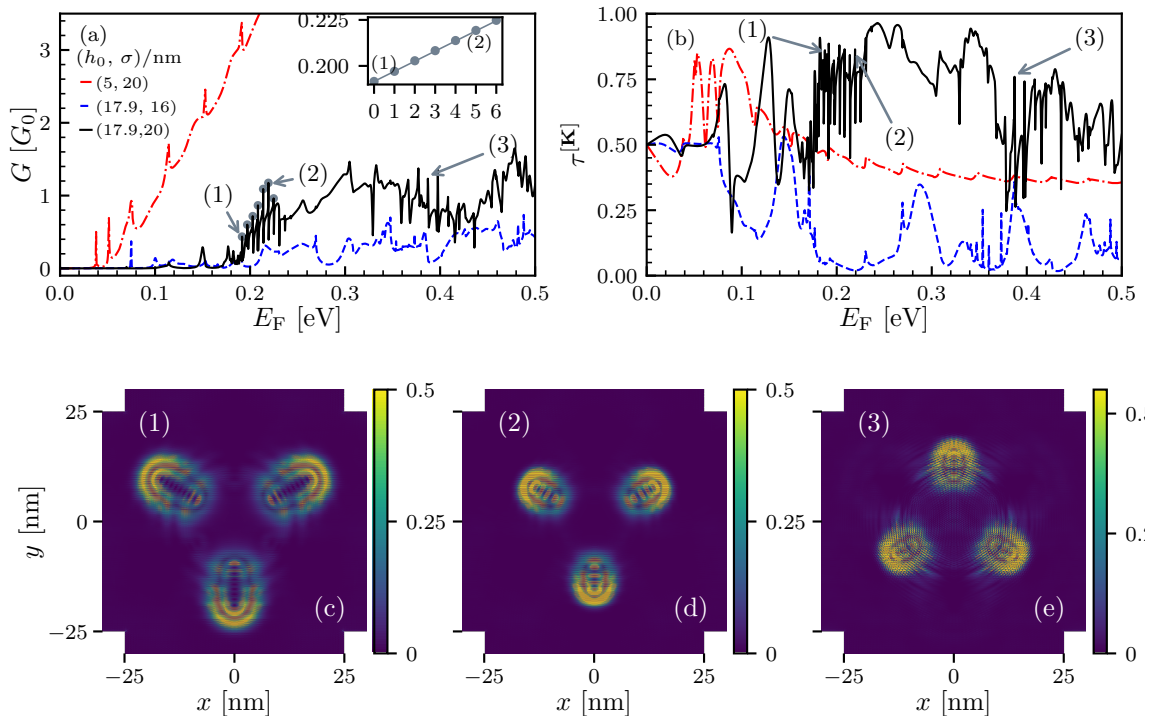
Fig. 9: (a)[(b)] Conductance [valley polarization] in dependence of the Fermi energy E_F for a strained $1/\sqrt{3}$-$\mathcal{T}_3$ lattice Hall bar with $W = 50$ nm and different (h_0, σ) combinations given in the legend. The gray circles denote peaks in the conductance at energies E_n for $h_0, \sigma = (17.9, 20)$ nm. The inset shows the peak energies E_n of (a) as a function of resonance index with a linear fit $E_n = E_0 + \Delta E_n n$ with $E_0 = 0.1911$ eV and $\Delta E_n = 0.0055$ eV. For the marked resonances (1) at $E_0 = 0.191$ eV , (2) at $E_5 = 0.219$ eV, and (3) at $E_F = 0.387$ eV, we find $\tau^{[\mathbf{K}]} = 0.88$, $\tau^{[\mathbf{K}]} = 0.86$, and $\tau^{[\mathbf{K}]} = 0.76$, respectively. (c)-(e) Zoomed-in LDOS at resonance (1),(2), and (3). Figure altered from article II.

B_{ps}-values with $\gamma = -1$ and $\gamma = +1$, respectively. By inspecting the inset in Fig. 9(a), we notice that the resonances energies [grey dots] E_n for $\gamma = -1$ between (1) and (2) [cf. Fig. 9(a)] are equidistant in the index n with spacing $\Delta E_n = 5.5$ meV, and we find $E_n \propto n \propto \sqrt{B_{\mathrm{ps},n}}$. This observation is consistent with the analysis conducted in Ref. [86], where the authors predicted an (approximately) linear relationship between the pseudo-LL subbands by the number n of iso-field orbits that surround an integer magnetic flux. For higher energies, the valley polarization tends to diminish because the cyclotron diameter $(d_c = 2|E_F|/v_F e B_{\mathrm{ps}})$ grows linearly, which shrinks the effective width of the bump [59]. To better characterize the various pseudo-LL subbands, we analyze the spatial distribution of LDOS in the quantum dot region. For the LDOS of resonances (1) [(2)] in Fig. 9(c)[(d)], we observe threefold-symmetric ∇-like patterns with a large [small] 'petal' radius, which corresponds to the iso-field orbits with small [large] B_{ps}. The petals of (1)/(2) [(3)] coincide with the $\gamma = -1$ [$\gamma = +1$] regions of the PMF [cf. Fig. 8(b)]. Note that the resonances (1),(2), and (3) are characteristic of the whole band of resonances. Furthermore, the ∇ and Δ shapes exhibit a sublattice polarization, i.e. only the *A-B* or *B-C* sublattices are, respectively, occupied. In fact, any $0 < \alpha < 1$ breaks the *A* and *C* sublattices in the α-$\mathcal{T}_3$ lattice, which splits the pseudo-LL bands of $\gamma = \mp 1$, thereby reducing the rotational symmetry of the LDOS pattern from sixfold to threefold and inducing an energy gap between $\gamma = -1$ and $\gamma = +1$ states. As can be seen for the dice-lattice case [$\alpha = 1$] in Fig. 4(b) from article II, the conductance reveals only a single band of resonances that are equidistantly spaced and nearly perfectly valley-polarized while the sixfold-symmetry of the LDOS is restored [cf. Fig. 4(e) and (f) in article II]. In the graphene-limit ($\alpha = 0$), a similar sixfold-symmetric 'flower' pattern has also been reported [56, 57]. As shown in detail in Fig. 4(g)

and Fig. 4(h) of article II, the local current densities of resonance (1) and (3), made of electrons belonging to the **K** valley, are trapped inside the bump in long-living resonant states orbiting the ∇ ($\gamma = -1$) and Δ ($\gamma = +1$) regions of the PMF before being transmitted into lead R along the zero-field lines of the PMF, while the unpolarized current is effectively collected by the perpendicular leads.
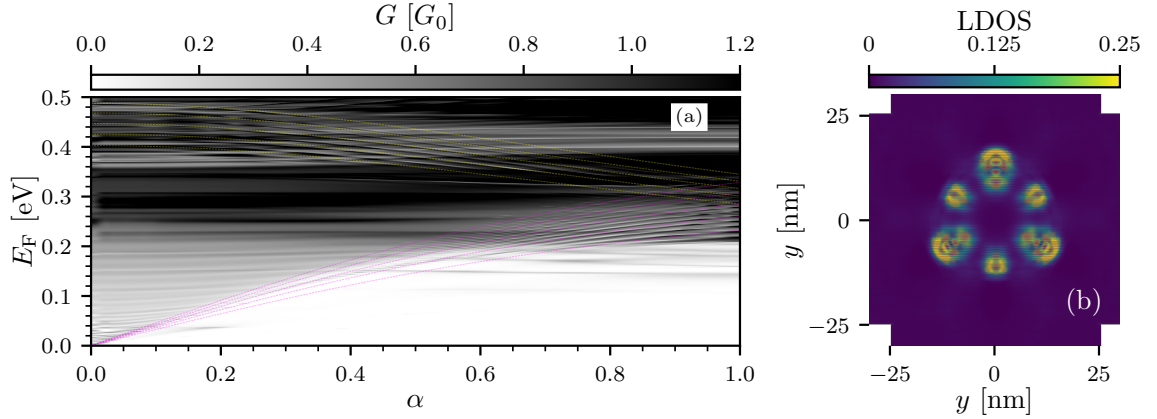

Fig. 10: (a) Contour plot of the conductance as function of α and E_F. The Pseudo-LLs from Eq. (16) are shown for $n = 0$ and $B_\mathrm{ps} \in [100, 200]$ T for $\gamma = -1$ (magenta) and $\gamma = +1$ (yellow). (b) (Zoomed-in) LDOS at E_F=0.335 eV and $\alpha = 0.95$. Figure adapted from article II

Figure 10(a) displays the full E_F-α-dependence of the conductance as a contour plot. We add the pseudo-LL of Eq. (16) for $n = 0$ and $\gamma = \pm 1$ with $B_\mathrm{ps} \in [100, 200]$ T as a guide to the eye. When $\alpha > 0.85$, we observe overlapping pseudo-LL subbands [see also Fig. 5.(b) of article II]. At these crossing points, the corresponding LDOS reveals a 'flower'-like pattern consisting of ∇- and Δ-shapes with different petal sizes [cf. Fig. 10(b)] because pseudo-LL subbands can only cross for unequal B_ps-values. Note that the observed LDOS pattern remains threefold-symmetric due to the different radii of the ∇ and Δ 'petals'.

Valley-polarized current generation by dynamic Gaussian bumps   Now, we time-periodically drive the height of the Gaussian bump, which induces an additional valley-dependent PEF [Fig. 8(d)]. This allows us to assess the valley-filter capabilities of crossed pseudoelectromagnetic fields and demonstrate the tunability of such setups by analyzing the steady-state transport properties in the four-terminal setup using Floquet theory. Below we will demonstrate, that the time-periodical drive gives us an additional 'knob' to tune the valley filtering.

Let us first give a brief overview of the non-equilibrium Floquet-Green's function formalism and transport quantities. The DC transmission between the left (L) and right lead (R) through our device is then obtained in the Keldysh non-equilibrium Green's function approach by

$$T(E) = \sum_{k \in \mathbb{Z}} \mathrm{Tr} \left[G_{k0}^r \Gamma_{00}^\mathrm{L} G_{0k}^a \Gamma_{kk}^\mathrm{R} \right], \tag{19}$$

where the retarded (advanced) Green's function in Floquet basis is denoted by $G_{k0}^{r(a)}$. The level-width function of the left (right) lead is simply the level-width function of the undriven lead shifted by $2k\Omega$. For the Floquet representation, we write $\Gamma_{kk}^{L(R)} = i[\Sigma_\mathrm{L(R)}^r - (\Sigma_\mathrm{L(R)}^r)^\dagger]_{kk}$, where $\Sigma_\mathrm{L(R)}^r$ is the respective self-energy in Floquet representation, i.e., $(\Sigma_\mathrm{L(R)}^r)_{km} = \delta_{km} \Sigma_\mathrm{L(R)}^r(E + 2k\Omega)$ and k is the sideband index. Here, the frequency $2k\Omega$ enters the Floquet equations, because the Hamiltonian $H^{(\alpha)}(t)$ has an oscillation period of $T/2$ (frequency of 2Ω) since Eq. (9) admits $h(r, t)^2$. The retarded

Floquet-Green's function G^r_{mn} is defined by [87]

$$\sum_{m\in\mathbb{Z}} \left[(E + 2k\Omega)\delta_{km} - H^{(k-m)}_\alpha - (\Sigma^r)_{km} \right] G^r_{mn}(E)$$
$$= \delta_{kn}, \tag{20}$$

where $(\Sigma^r)_{km}$ denotes the sum over the four lead self-energies in Floquet representation. The Hamiltonians $H^{(m)}_\alpha$ are the Fourier coefficients of the series $H_\alpha(t) = \sum_m e^{i2m\Omega t} H^{(m)}_\alpha$, which are given in Eq. (8) in article III. The Fourier-transformed transfer amplitudes given by Eq. (9) of article III are exemplarily shown in Fig. (7) for $m = 0,\ 1,\ 2$ as a function of the height differences between nearest neighbors up to the maximal sustainable elastic strain of graphene, $z_{ij} = 0.5625$, corresponding to 25% of the bond-length change [50]. In Floquet space, the transfer amplitudes of the on-diagonal Hamiltonian $H^{(m=0)}$ are decreased in comparison to the static transfer amplitudes due to time-averaging [cf. Fig. 7(b)]. Furthermore, the off-diagonal part $H^{(m\neq0)}$ depends crucially on $z_{ij} \propto h_0^2$ and decreases exponentially with m for constant z_{ij}. Due to the time-reversal symmetry, we have $H^{(m)} = H^{(-m)}$. Since the valleys are separated in momentum space for zigzag edges, we
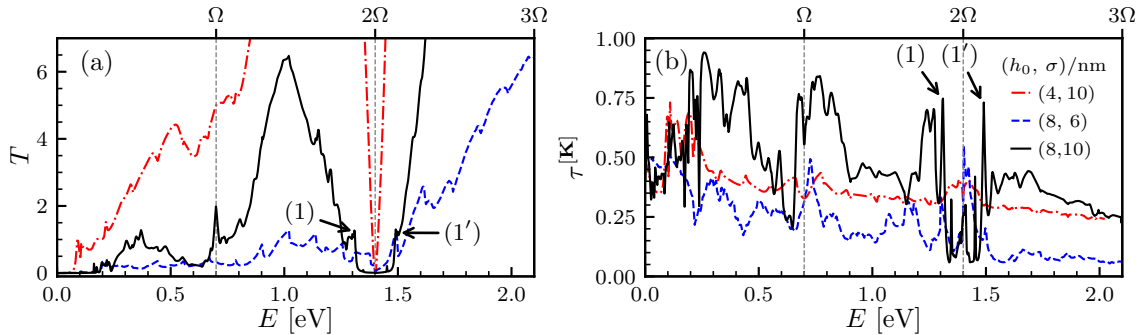

Fig. 11: (a)[(b)] Transmission [valley polarization] as a function of (quasi-) energy for an oscillating Gaussian bump with frequency $\Omega = 0.25J$ in a $1/\sqrt{3}$-$\mathcal{T}_3$ lattice Hall bar with $W = 20$ nm and different (h_0, σ) combinations given in the legend. For both the resonance (1) (1') at $E \simeq 1.31$ eV and $E \simeq 1.49$ eV, we find $\tau^{[\mathbf{K}]} = 0.75$. The figure is adapted from article III.

have $\Sigma^r_R = \Sigma^{r,[\mathbf{K}]}_R + \Sigma^{r,[\mathbf{K}']}_R$, which allows us to single-out a valley-index in the transmission,

$$T^{[\mathbf{K}]}(E) = \sum_{k\in\mathbb{Z}} \mathrm{Tr} \left[G^r_{k0} \Gamma^L_{00} G^a_{0k} \Gamma^{R,[\mathbf{K}]}_{kk} \right]. \tag{21}$$

Further information on excited states inside the setup is obtained by the spatial distribution of the time-averaged local density of states (LDOS), which is defined on site i in Floquet basis by

$$\text{T-LDOS}(E)_i = -\frac{1}{\pi} \mathrm{Im} \left(G^r_{00} \right)_{i,i} (E). \tag{22}$$

By the Floquet-Green's function algorithm, we also have access to the spatially resolved current density between site i and site j at a (quasi-) energy E [88],

$$I_{ij}(E) = \sum_{k\in\mathbb{Z}} J^{(k)}_{ij} \left[G^<_{0k} \right]_{ij} (E), \tag{23}$$

where the $\left[G^<_{0k} \right]_{ij} (E)$ is obtained by the Keldysh equation (16) in article III. In numerical practice, after truncating the infinite sum in Eq. (20) at $m \in [-M, M]$, we solved Eq. (20) with a recursive Floquet-Green's function algorithm [88, 89] by dividing the setup in circular slices[90]. The full numerical details and definitions are found in Sec. II in article III.

In the following, we only consider driving frequencies below the bandwidth since the effective Hamiltonian in the (high-frequency) off-resonant limit obtained by the Floquet-Magnus expansion
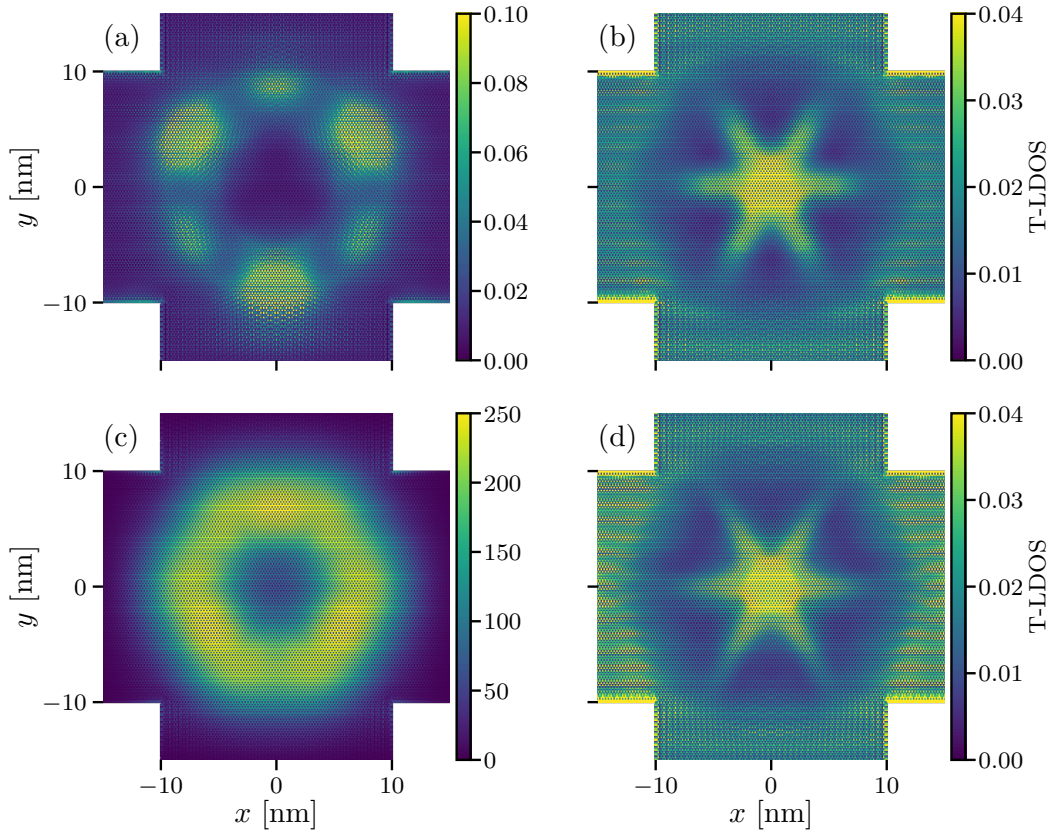
Fig. 12: (a)-(d) Time-averaged LDOS at $E = \Omega$, resonance (1), $E = 2\Omega$, and resonance (1'), respectively. The figure is adapted from article III.

is simply the time-averaged Hamiltonian (up to order Ω^{-2}) because elastic strain conserves time-reversal symmetry, see discussion in article III [91]. Therefore, we exemplarily take $\Omega = 0.25\,J$, then taking $M = 5$ and $J_{ij}^{(m)}$ up to $m = 3$ guarantee convergence in the truncation of the Floquet-Green's function.

We start the discussion on the Floquet-transport properties of dynamically strained quantum dots by examining the transmission [cf. Fig. 11(a)] and valley polarization [cf. Fig. 11(b)] for small, large, and medium pseudoelectromagnetic fields on the intermediate $1/\sqrt{3}\text{-}\mathcal{T}_3$ lattice. In view of the static results, we first examine $(h_0, \sigma) = (8, 10)$ nm [medium PMF and PEF] because the expected $\tau^{[\mathbf{K}]}$ is large. Indeed, we notice three characteristic transport regimes for valley-filtering that are emerging due to the time-dependent strain: (i) $E < \Omega$, (ii) $E \simeq \Omega$, and (iii) $E \simeq 2\Omega$. The regime (i) is reminiscent of the static case: We find a threshold energy of $E \simeq 0.2$ eV [cf. Fig. 11(a)] below which the oscillating Gaussian bump blocks any current. Above this energy, we observe transmission resonances with a (threefold-symmetric) 'flower'-like LDOS patterns due to the broken inversion symmetry and greatly increased valley polarization (see Fig. 9 and the discussion). Approaching regime (ii), the valley polarization deteriorates since higher bands are populated and the cyclotron diameter, $d_c \propto E$, grows, thereby effectively shrinking the width of the Gaussian bump [59]. Right below $E = \Omega$, the transmission actually decreases because the Floquet drive induces a gap at the zone boundary. In fact, we showed in article III that this α-dependent gap vanishes [is maximized] when $\alpha = 1$ [$\alpha = 0$]. At the $m = 0$ and $m = 1$ zone boundary where $E = \Omega$ however, we observe a sudden onset of a valley-polarization plateau [cf. Fig. 11(b)], which is in stark contrast to the static case [cf. Fig. 9(a)]. The regime (iii) about $E \simeq 2\Omega$ features a symmetric transmission gap of size $\delta = 0.19$ eV due to the hybridization of the flat band of the $m = 1$ particle-hole symmetric Floquet
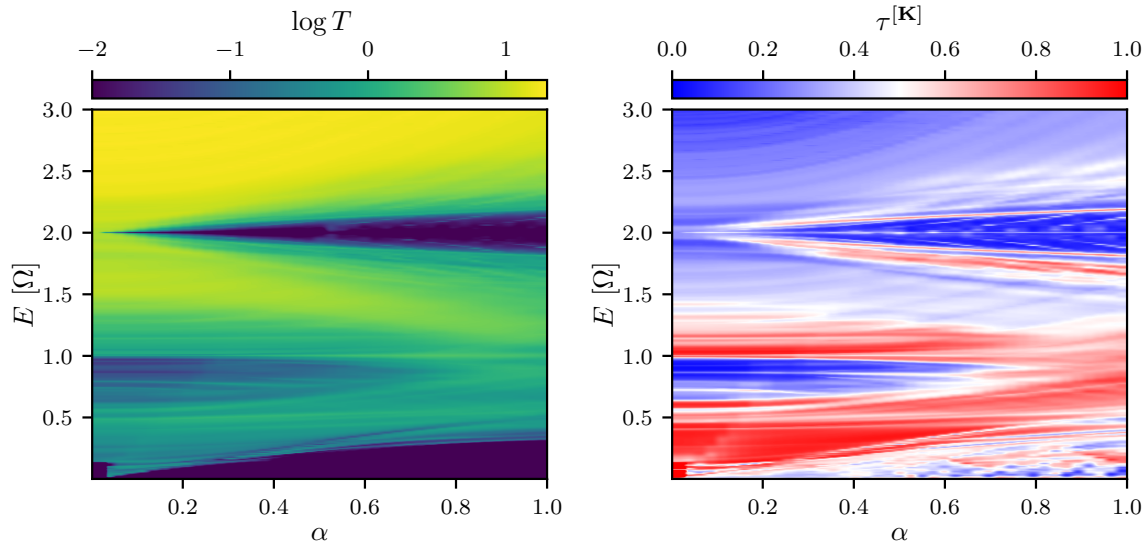
15

Fig. 13: Logarithmic transmission (a) and valley polarization (b) as a function of (quasi-) energy and scaling parameter α for $h_0 = 8$ nm, $\sigma = 10$ nm, and $\Omega=0.25J$.

sideband with the central $m = 0$ band via the off-diagonal $H^{(1)}$ term. Exactly at $E = 2\Omega$, the setup blocks any current between the left and right lead, i.e. $T(2\Omega) = 0$, due to the zero group velocity of flat-band states. Actually, we showed that the oscillating bump completely blocks any current in the setup by inspecting the transmission into the other leads [not shown]. At the edges of this gap, we find new valley-polarized transmission resonances at (1) and (1') which are related to the PEF (see below). By reducing the amplitude to $h_0 = 4$ nm, we decrease the pseudo-gauge field (18) by decreasing z_{ij} which is proportional to h_0^2 [see Eq. (4) of article III]. Thereby, the electrons flowing from the left lead to the right lead are transmitted with decreased scattering. At $E = 2\Omega$ however, the transmission vanishes again despite the reduced Floquet-sideband coupling $J_{ij}^{(m)}$. Furthermore, we showed in article III that the valley-polarized plateau in regime (ii) and the resonant states in (iii) persist for $6 \lesssim h_0/\text{nm} \lesssim 10$. However, the position of the resonant states in the regime (iii) scale approximately linearly with h_0 [see Fig. 5 in article III]. When $(h_0, \sigma) = (8, 6)$ nm, we notice that the transport between the lead L and R is almost completely blocked due to the large PMF and PEF field. Nevertheless, a small amount of $\mathbf{K'}$ electrons is able to pass by the Gaussian bump, similar to the static case.

Figure 13 demonstrates the α-dependency of the valley-filtering regimes (i-iii) of the oscillating Gaussian bump. The static-like regime (i) [$E < \omega$] has a finite transmission for small energies near $E = 0$ around $\alpha \gtrsim 0$ due to the zigzag edge states of graphene. Approaching $E \lesssim \Omega$, we notice a gap in the transmission related to the drive of the oscillating bump. The regime (ii) shows a (nearly) vanishing transmission up until $\alpha \simeq 1/\sqrt{2}(\simeq 0.707)$. In Fig. 13(b), this becomes especially apparent: Here, the valley-polarized plateau merges with the static-like regime (i). The transition near $\alpha \simeq 1/\sqrt{2}$ coincides with the value of the scaling parameter in the topological phase transition of the irradiated α-$\mathcal{T}_3$ lattice in the off-resonant limit, where the Chern number of the valence or conduction band takes $C = \pm 2$ instead of $C = \pm 1$. The critical scaling parameter $\alpha = 1/\sqrt{2}$ marks the (soft) boundary above which the dynamics of the charge carriers are dominated by pseudospin-1 characteristics instead of the pseudospin-1/2 one. When $\alpha > 0$, the transmission vanishes at $E = 2\Omega$ [regime (iii)], and the gap scales linearly with the scaling parameter.

To characterize the different transport channels for $E = \Omega$, resonances (1) and (1'), and $E = 2\Omega$, we examine the T-LDOS shown in Fig. 12(a)-(d), respectively. Beginning at $E = \Omega$, a threefold-symmetric T-LDOS pattern emerges, mimicking the static-like overlapping ∇ and Δ patterns of different petal sizes observed in article II Fig. 5(c). However, the situation is much different at $E \simeq 1.31$ eV [and $E \simeq 1.49$ eV] since the spatial distribution of the time-averaged LDOS has a large amplitude at the center of the bump. Here, the PEF [see Fig. 7(b) and (d)] pushes the incoming
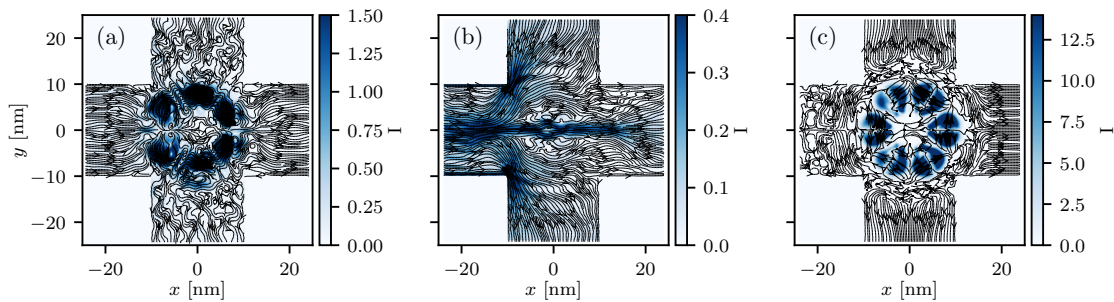
Fig. 14: Local current densities at $E = \Omega$ (a), resonance (1) in (b), and $E = 2\Omega$ (c) for $\alpha = 0$, $\alpha = 1/\sqrt{3}$, and $\alpha = 1$, respectively. The figure is adapted from article III.
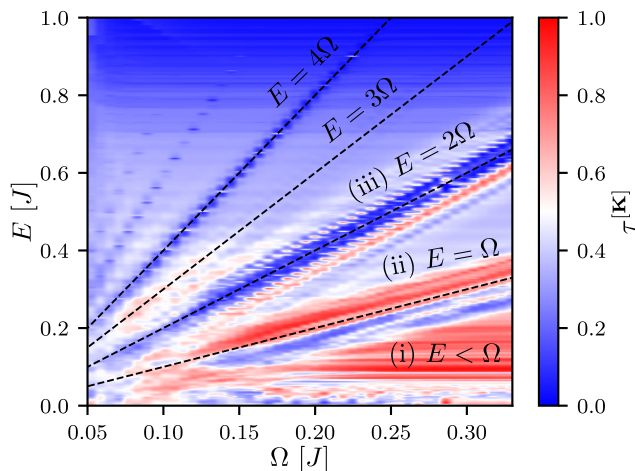

Fig. 15: Contour plot of the valley polarization as a function of (quasi-) energy and frequency for an oscillating Gaussian bump on the $1/\sqrt{3}$-$\mathcal{T}_3$ lattice. The Van Hove singularity at $E = J$ marks the upper limit for the definition of the valley polarization. Dashed lines denote $E = m\Omega$, where $m = 1, 2, 3$ and 4, respectively. Adapted from article III.

K-valley electrons towards the center, while the **K**$'$ electrons are blocked, creating an effective valley polarization. The time-averaged LDOS at $E = 2\Omega$ depicts a flat-band state with a large degeneracy confined to the Gaussian bump, which is unlike the flat band at $E = 0$ and is therefore induced by the dynamical drive of the strain. [cf. colorbar in Fig. 12(c)]. This flat-band state is repeated at $E = 2m\Omega$ with linearly decreasing spectral weight due to the weak off-diagonal $H^{(m)}$ Hamiltonian [see above].

To give further insight into the different regimes, we look upon the local course of the time-averaged current density in Fig. 14 for regimes (ii), resonance (1), and the flat band at $E = 2\Omega$ in regime (iii) for $\alpha = 0$, $\alpha = 1/\sqrt{3}$, and the dice lattice [$\alpha = 1$], respectively, where the direction of the electron flow is depicted by the arrows and its magnitude by the blue intensity plot. For regime (ii), we notice that the majority of the incoming electron flow is located near the lobes of PMF, resembling the static motion [cf. Fig. 4(i)(j) of article II] which is however distorted by the PEF. At the resonance (1), the PEF focuses **K** electrons through the quantum-dot region along the x-axis [cf. Fig. 8(c)] while the **K**$'$ electrons exit the setup by the perpendicular leads [cf. Fig. 14(b)]. The flat-band state shows a large trapped current inside the Gaussian bump [cf. Fig. 14(c)], emphasizing the localized nature of this state.

To avoid the rapidly increasing Floquet-space dimensions, we have only considered a rather large frequency of $\Omega = 0.25\,J$ so far, which coincides with an oscillating frequency of 170 THz. Therefore we show in Fig. 15 the valley polarization frequency dependence of the valley-filtering regimes up to $\Omega = 0.05\,J$ [34 THz]. Clearly, the regimes (ii) and (iii) endure frequencies down to at least $\Omega = 0.1\,J$ of the dynamical strain until the gap Δ is outside the first Floquet zone, i.e. $\delta = 2\Omega$. The valley-filtering capabilities of regime (i) depreciate through the overlap with regime (ii) below $\Omega = 0.2\,J$.

To sum up, we have demonstrated that out-of-plane deformations have several advantages for the

17

generation of valley-polarized currents in α-$\mathcal{T}_3$ lattices. By exciting different pseudo-LL subbands due to the inhomogeneous PMF, a sublattice filter to access pseudospin-1/2 subspace is feasible by breaking the inversion-symmetry for any $0 < \alpha < 1$. Furthermore, the regions of valley-polarized and unpolarized transport of the α-$\mathcal{T}_3$ lattice in the (h_0, σ) parameter space are notably sharpened compared to similar graphene configurations. However, the main disadvantage of this configuration is the small energy range in which valley-polarized currents can be generated. We have also shown that a time-periodic driving of the height of the Gaussian bump is able to induce novel valley-filtering regimes by the additional PEF. For certain parameters of bump and in dependence of the scaling parameter α, we found a plateau in the valley polarization at the first Floquet-zone boundary $E = \Omega$ and valley-polarized resonances near the center of the first Floquet zone $E = 2\Omega$. The filtering regimes can be tuned through the energy range by varying the driving frequency.

1.4 Conclusions

In this thesis, we have considered generalized Dirac-Weyl quasiparticles on α-$\mathcal{T}_3$ quantum dots in external magnetic fields and in valley-dependent pseudoelectromagnetic fields induced by applied out-of-plane strain.

Graphene and α-$\mathcal{T}_3$ nanostructures with various edge terminations and shapes have been studied to modify their properties and band structure [65–68, 71, 72]. However, the infinite-mass boundary condition [69] has not been previously considered in generalized α-$\mathcal{T}_3$ lattices. Given the resulting valley-contrasting Landau level and the flat band around the Dirac nodes, it is natural to ask about the effect of inhomogeneous strain-induced generate pseudomagnetic fields to manipulate the valley-degree of freedom in the α-$\mathcal{T}_3$ lattice. This was first studied in our article II. Subsequently, Ref. [80] derived the exact pseudo-LLs induced by non-uniform uniaxial and triaxial strains, where the sublattice polarization of our results was confirmed. Dynamically straining graphene gives rise to a pseudoelectric field, which has been widely explored for the valley-current generation [92, 93] or valleytronic devices [85] in the adiabatic limit justified by the slow graphene oscillation frequencies (10 to 100 MHz) and the high carrier mobility (1 THz). In our approach, we have considered larger, though somewhat unrealistic in solid-state systems, frequencies to enhance the pseudoelectric field, providing a proof-of-principle that time-dependent strain induces and enhances valley-filtering. Nevertheless, our setup should be engineerable in optical α-$\mathcal{T}_3$ lattices [33, 34] due to the high degree of manipulability of the transfer amplitudes [94–96].

In article I, we have generalized the infinite-mass boundary to α-$\mathcal{T}_3$ lattices to study Dirac-Weyl quasiparticles confined to quantum dots under external magnetic fields. Subsequently, we verified the analytically derived valley-anisotropic eigenstates of the quantum dot by numerically solving the tight-binding lattice-model in closed (isolated) and open (contacted) systems. We found good agreement with the valley-anisotropic states in the negative energy range close to the neutrality point. In the positive energy range, we found additional states located at the boundary connected to the shifted flat band. By locally disordering the gap size outside the dot, we found the bulk states to be less affected while the edge states were strongly perturbed. The flat band remains unaltered under the boundary condition and external magnetic fields. The precise conditions for the existence of boundary modes however remain an open problem for future works.

Motivated by the valley-contrasting properties of the Dirac-Weyl quasiparticles, we generalized strain fields to α-$\mathcal{T}_3$ lattices in article II to modify the electronic properties by generating effective pseudo-gauge fields with opposite signs in the **K** and **K′** valley. We showed that the inhomogeneous pseudomagnetic field generated by static Gaussian bumps placed at the center of a four-terminal Hall bar device acts as a valley filter by causing and controlling valley-polarized currents in the outgoing lead. We also classified and identified experimental realizable valley-filtering regimes based on the height and width of the Gaussian bump. In addition, the Fermi energy played a central role: the valley polarization is most dominant when incoming electrons are excited to pseudo-Landau level subbands that are linked to different iso-field orbits encircling the lobes of the pseudomagnetic field. These subbands are equidistantly spaced in the energy space. Furthermore, a finite α breaks the inversion symmetry of the α-$\mathcal{T}_3$ lattice which splits the pseudo-Landau levels into sublattice-polarized bands whose local density of states is localized at the negative or positive pseudomagnetic field

regions. Thereby, an *A-C* sublattice filter is realizable.

To extend the valley-filtering capabilities, we have equipped the Gaussian bump with a time-periodic drive in article III to induce a valley-dependent pseudoelectric field besides the pseudomagnetic field. We analyzed and assessed the steady-state transport properties of Gaussian bumps centered in a four-terminal Hall bar setup by the valley-filtering efficiency and the spatial charge and current densities obtained with a recursive Floquet-Green's function algorithm. In addition to the static regime for small energies, we identified two α-dependent dynamical valley-filtering regimes caused by the periodic drive. Firstly, we found an additional valley-polarization plateau at the Floquet-zone boundary between the central and first Floquet copy that also displayed a "flower"-like pattern in the local density of states. Secondly, we detected a series of transmission gaps at the center of every Floquet sideband $2m\Omega$ related to the Floquet coupling of the flat band with the central Floquet copy. Under certain strain parameters, a novel valley-filtering regime appears near the transmission gaps where the incoming **K** electrons are focused through the bump by the pseudoelectric field, instead of encircling the lobes of the pseudomagnetic field. A stability analysis demonstrated that the polarization regimes are tunable by the driving frequency.

So far, the flat band has played a rather minor role because it persists under external fields and does not directly affect the single-particle transport calculations due to the vanishing group velocity. The effect of lattice modulations by, e.g., strains on the composition of the flat band in dice models have not yet been studied, however. In principle, the flat band of the dice model is composed of compact localized states (CLS) that have nonzero weight only inside a finite real-space region due to the destructive interference responsible for localization [25, 97–99]. The set of all CLSs generated by the lattice translations typically produces the basis of the flat band. However, it has been shown that this set is linearly dependent in the dice model with periodic boundary conditions (real-space torus) due to the band-crossings at the **K** and **K**$'$ points. This was attributed to an immovable singularity in the Bloch wave function of the flat band in momentum space [99, 100]. Therefore, to span the basis of the flat band, the so-called non-contractible loop states, which wrap around the torus, have to be supplied [99, 101]. These states are extended along one spatial direction while localized along the other direction and cannot be constructed via the CLSs. Recently, the maximum Hilbert-Schmidt quantum distance near the band-crossing point has been proposed to evaluate its singular nature [102], which leads to anomalous Landau levels [103] and boundary modes through the bulk-interface correspondence [102] in systems with quadratic band-touching points. Besides the fundamental interest, these so-called singular flat bands have recently attracted attention because of potential applications in photonic lattices, such as distortion-free image transmission [104] and slow-light propagation [105]. In article IV, we address this issue by studying the dice model under a uniaxial strain along the zigzag orientation with a Haldane-type next-nearest neighbor (NNN) interaction that breaks the time-reversal symmetry. Such a Haldane term is often studied in the context of topological insulators as it realizes an anomalous quantum Hall effect on the dice [and honeycomb] lattice with Chern number $C = \pm 2$ $[C = \pm 1]$ [106, 107]. The uniaxial strain η breaks the threefold rotational symmetry and trimerizes the model along the y-axis. We computed the complete topological phase diagram (m, ϕ, η) where m is an on-site inversion-symmetry breaking term and identified all band gap closings at $m = m_c(\phi, \eta)$ similar to the graphene case [108]. We found the central band to be exactly flat for $\phi_c = (2n + 1)\pi/2$ and on this phase boundary $m_c(\phi_c, \eta)$, the system is a Dirac semimetal that hosts a single pseudospin-1 Dirac node whose position in the Brillouin zone $\mathbf{k}_c$ depends on η. In this case, we demonstrated that the flat band of the modified Haldane-dice model is singular by finding a maximum quantum distance $d_{\max} = 1$ of its Bloch wave function around the band-crossing point. To confirm this, we derived the general CLSs with Haldane-type NNN interaction and showed that the set of all CLS is linearly dependent in the vicinity of $\mathbf{k}_c$. We derived the two non-contractible loop states and an extended state whose components depend on the parameters of the system.

Throughout this thesis, we have neglected the electron-electron interaction to study the effect of external (strain) fields and boundary conditions on the flat band and Dirac-Weyl quasiparticle dynamics. As pointed out in the introduction, the electron-electron interaction in flat-band systems has striking consequences for correlation effects. In this regard, future works should focus on the interplay of strain and electron-electron interaction on the dice lattice regarding the valley population

dynamics and correlation effects.

After all, the α-$\mathcal{T}_3$ lattice is a promising platform to study one-particle physics with a relativistic-like Hamiltonian beyond the conventional Dirac equation due to the flat band and increased (pseudo-) spin. We have shown that the intrinsic inversion-symmetry breaking by the scaling parameter α allows for the precise manipulation of the valley and sublattice degree of freedom without any (gap-creating) on-site potential because of the variational Berry phase, which, in combination with externally applied strain fields to Dirac-Weyl quasiparticles, could be a building block of future valleytronic devices. In addition, the α-dependent interband coupling measured by the maximum quantum distance around the Dirac nodes makes the α-$\mathcal{T}_3$ lattice an ideal playground for studying geometric contributions to interband effects.

2 Thesis articles

Author Contribution

Article I:
Electronic properties of α-$\mathcal{T}_3$ quantum dots in magnetic fields, A. Filusch and H. Fehske, *Eur. Phys. J. B* (2020) **93**: 169. Copyright The Author(s) (2020).
A. Filusch and H. Fehske discussed the scope of the work and the strategy of the calculation. The calculations were performed by A. Filusch. H. Fehske wrote the manuscript, which was edited by A. Filusch.

Article II:
Valley filtering in strain-induced α-$\mathcal{T}_3$ quantum dots, A. Filusch, A. R. Bishop, A. Saxena, G. Wellein and H. Fehske, *Phys. Rev. B* **103**, 165114 (2021). Copyright (2021) by the American Physical Society.
All authors discussed the scope of the work and the strategy of the calculation. The calculations were performed by A. Filusch. A. Filusch and H. Fehske wrote the manuscript, which was edited by all authors.

Article III:
Tunable valley filtering in dynamically strained α-$\mathcal{T}_3$ lattices, A. Filusch and H. Fehske, *Phys. Rev. B* **106**, 245106 (2022). Copyright (2022) by the American Physical Society.
A. Filusch and H. Fehske discussed the scope of the work and the strategy of the calculation. The calculations were performed by A. Filusch. A. Filusch and H. Fehske wrote the manuscript.

Article IV:
Singular flat bands in the modified Haldane-Dice model, A. Filusch and H. Fehske, submitted to Physica B: Condensed Matter (March 2023).
A. Filusch and H. Fehske discussed the scope of the work and the strategy of the calculation. The calculations were performed by A. Filusch. A. Filusch and H. Fehske wrote the manuscript.

Confirmed:

_____
(Prof. Dr. Holger Fehske)   Greifswald, 6 March 2023

_____
(Alexander Filusch)   Greifswald, 6 March 2023

THE EUROPEAN
PHYSICAL JOURNAL B

Regular Article

Electronic properties of $\alpha - \mathcal{T}_3$ quantum dots in magnetic fields

Alexander Filusch and Holger Fehske[a]

Institute of Physics, University Greifswald, 17487 Greifswald, Germany

Abstract. We address the electronic properties of quantum dots in the two-dimensional $\alpha - \mathcal{T}_3$ lattice when subjected to a perpendicular magnetic field. Implementing an infinite mass boundary condition, we first solve the eigenvalue problem for an isolated quantum dot in the low-energy, long-wavelength approximation where the system is described by an effective Dirac-like Hamiltonian that interpolates between the graphene (pseudospin 1/2) and Dice (pseudospin 1) limits. Results are compared to a full numerical (finite-mass) tight-binding lattice calculation. In a second step we analyse charge transport through a contacted $\alpha - \mathcal{T}_3$ quantum dot in a magnetic field by calculating the local density of states and the conductance within the kernel polynomial and Landauer-Büttiker approaches. Thereby the influence of a disordered environment is discussed as well.

1 Introduction

Quantum matter with Dirac-cone functionality is expected to provide the building block of future electronics, plasmonics and photonics. Against this background, above all graphene-based nanostructures were intensively examined, both experimentally and theoretically, in the recent past. This is because their striking electronic properties can be modified by nanostructuring and patterning, e.g., manufacturing nanoribbons [1], nanorings [2], junctions [3], quantum dots [4], or even quantum dot arrays [5,6]. Thereby the transport behaviour heavily relies on the geometry of the sample (or device) and its edge shape [7,8].

The mutability of systems with Dirac nodal points, which is especially important from a technological point of view [9], can also be achieved by applying external electric (static or time-dependent) fields. One of the options is nanoscale top gates that modify the electronic structure in a restricted area [10]. This allows to imprint junctions and barriers relatively easy, and therefore opens new possibilities to study fascinating phenomena such as Klein tunnelling [11,12], Zitterbewegung [13,14], particle confinement [15,16], Veselago lensing [17], Mie scattering analogues [18–22] and resonant scattering [23,24]. Clearly the energy of the charge-carrier states can be manipulated by (perpendicular) magnetic fields as well. With this the quantum Hall effect, the Berry phase curvature, the Landau level splitting and Aharonov-Bohm oscillations have been investigated [2,25,26].

Shortly after the field of graphene was opened, Dirac-cone physics was combined with flat-band physics in a modified lattice, the $\alpha - \mathcal{T}_3$ lattice, which is obtained by coupling one of the inequivalent sites of the honeycomb lattice to an additional atom located at the centre of the hexagons with strength α [27–29]. Obviously, such a lattice interpolates between graphene ($\alpha = 0$) and the Dice lattice ($\alpha = 1$). Most notably, the flat band crosses the nodal Dirac points, which has peculiar consequences, such as an α-dependent Berry phase [30], super-Klein tunnelling [31,32], or Weiss oscillations [33]. Interestingly, the magneto-optical response will be also enhanced due to the flat bands [34]. Analysing the frequency-dependent magneto-optical and zero-field conductivity of $Hg_{1-x}Cd_xTe$ [35] at the critical cadmium concentration $x_c \simeq 0.17$ (marking the semimetal-semiconductor transition), it has been shown that this material can be linked to the $\alpha - \mathcal{T}_3$ model with $\alpha = 1/\sqrt{3}$ [36]. Other possibilities to realise the $\alpha - \mathcal{T}_3$ and Dice ($\alpha = 1$) models experimentally are cold bosonic or fermionic atoms loaded in optical lattices [30,37].

The massless Dirac equation [38] provides the basis for numerous theoretical investigations of the low-energy excitations in these novel, strictly two-dimensional systems [29,32,39–53], whereby the quasiparticles carry a pseudospin 1 in the Dice lattice rather than pseudospin 1/2 in the case of graphene. Accordingly one usually works with a three- (Dice) and two-component (graphene) realisation of the standard Dirac-Weyl Hamiltonian. Investigating the electronic properties of $\alpha - \mathcal{T}_3$ quantum dots in magnetic fields, we also start from such a description, and therefore must implement a boundary condition when the dot is cut out from the plane [39,54,55]. Of course, this approach has to be approved by comparison with lattice model results obtained numerically [55–57]. Addressing the transport behaviour of

---

contacted dots and the influence of disorder on that we have to work with the full lattice model in any case.

The outline of this paper is as follows. In Section 2 we introduce the $\alpha - \mathcal{T}_3$ model, discuss the continuum approach, derive the infinite-mass boundary condition, and solve the eigenvalue problem for an isolated quantum dot in a constant magnetic field in dependence on α. Section 3 contains our numerical results for the eigenvalue spectrum, the (local) density of states and the conductance. Thereby we critically examine how the continuum model results compare to the numerical exact tight-binding lattice-model data (Sect. 3.1). Afterwards we study transport through a quantum dot subject to a magnetic field in the end-contacted lead-sample geometry most relevant for experiments (Sect. 3.2), and analyse boundary disorder effects (Sect. 3.3). We conclude in Section. 4.

2 Theoretical approach

2.1 $\alpha - \mathcal{T}_3$ model

We start from the tight-binding Hamiltonian

$$
H^\alpha = -\sum_{\langle ij \rangle} t e^{i\Phi_{ij}} a_i^\dagger b_j - \sum_{\langle ij \rangle} \alpha t e^{i\Phi_{ij}} b_i^\dagger c_j
$$
$$
+ \Delta \sum_i \left(a_i^\dagger a_i - b_i^\dagger b_i + c_i^\dagger c_i \right) + \text{H.c.}, \quad (1)
$$

where $a^{(\dagger)}$, $b^{(\dagger)}$ and $c^{(\dagger)}$ annihilate (create) a particle in a Wannier state centred at site A, B and C of the $\alpha - \mathcal{T}_3$ lattice, respectively. The nearest-neighbour transfer amplitude between A and B sites is given by t, and will be rescaled by α if hopping takes place between nearest-neighbour B and C sites, see Figure 1a. In this way, the scaling parameter interpolates between the honeycomb lattice ($\alpha = 0$) and the Dice lattice ($\alpha = 1$). In the presence of a vector potential $\mathbf{A}(\mathbf{r})$, hopping is modified further by the Peierls phase $\Phi_{ij} = 2\pi/\phi_0 \int_i^j \mathbf{A}(\mathbf{r})d\mathbf{r}$ with $\phi_0 = h/e$.

In order to implement boundary conditions below, we have introduced a sublattice-dependent onsite potential Δ, which opens a gap in the band structure at the charge neutrality point. In what follows we assume that $\Delta > 0$; the case $\Delta < 0$ is obtained by changing the sign of the energy E. Note that a positive Δ will shift the flat band to the bottom of the upper dispersive one.

Next we write down the corresponding continuum Dirac-Weyl Hamiltonian in momentum space in the absence of a magnetic field, being valid for low energies near the Dirac-points K ($\tau = +1$) and K' ($\tau = -1$):

$$
H^\varphi_\tau = v_F \mathbf{S}^\varphi_\tau \cdot \mathbf{p} + U\Delta, \quad (2)
$$

where $\varphi = \arctan \alpha$ and τ is the valley index. In equation (2), $v_F = 3at/2\hbar$ is the Fermi velocity, where a refers to the lattice constant, and $\mathbf{p} = -i\hbar\boldsymbol{\nabla}$ denotes the momentum operator in two spatial dimensions. The components of the pseudospin vector $\mathbf{S}^\varphi_\tau = (\tau S^\varphi_x, S^\varphi_y)$ in
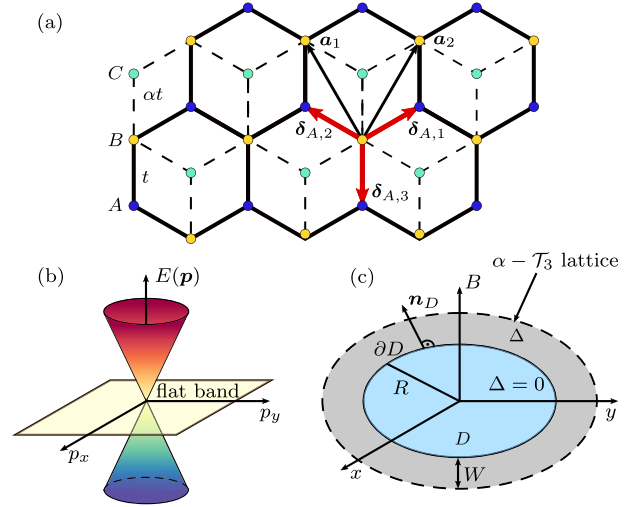

Fig. 1. (a) $\alpha - \mathcal{T}_3$ lattice with basis $\{A, B, C\}$ and Bravais-lattice vectors $\mathbf{a}_1$ and $\mathbf{a}_2$. Next-nearest neighbours are connected by $\boldsymbol{\delta}_{A,i}$ ($i = 1, 2, 3$) where α gives the ratio of the transfer amplitudes A-B and B-C. In the numerical work we use graphene-like parameters, i.e., a lattice constant $a = 0.142$ nm and a transfer integral $t = 3.033$ eV which sets the energy scale. (b) Continuum model energy dispersion near K or K' when $\Delta = 0$ with two linear dispersive bands and a flat band at $E = 0$. (c) $\alpha - \mathcal{T}_3$ dot setup with a constant magnetic field, perpendicular to the (x, y) plane. The quantum dot D (blue region) with radius R and zero gap ($\Delta = 0$) is surrounded by a ring of width W (grey, dashed border) having a gapful band structure ($\Delta > 0$). The vector $\mathbf{n}_D$ is perpendicular to the boundary.

(three-dimensional) spin space,

$$
S^\varphi_x = \begin{pmatrix} 0 & \cos\varphi & 0 \\ \cos\varphi & 0 & \sin\varphi \\ 0 & \sin\varphi & 0 \end{pmatrix},
$$
$$
S^\varphi_y = \begin{pmatrix} 0 & -i\cos\varphi & 0 \\ i\cos\varphi & 0 & -i\sin\varphi \\ 0 & i\sin\varphi & 0 \end{pmatrix}, \quad (3)
$$

represent the sublattice degrees of freedom. In equation (2), the matrix

$$
U = \begin{pmatrix} 1 & 0 & 0 \\ 0 & -1 & 0 \\ 0 & 0 & 1 \end{pmatrix} \quad (4)
$$

introduces a mass term, similar to σ_z in the standard (spin-1/2) massive Dirac-Weyl equation. Therefore H^φ_τ comprises the limiting cases of massive pseudospin 1/2 ($\alpha = 0$) and pseudospin 1 ($\alpha = 1$) Dirac-Weyl quasiparticles. Rescaling the energy by $\cos\varphi$, the eigenvalues $E_{\tau,s} | \psi_\tau \rangle$ of $H^\varphi_\tau | \psi_\tau \rangle = E_{\tau,s} | \psi_\tau \rangle$ become

$$
E_{\tau,0} = \Delta, \quad (5)
$$
$$
E_{\tau,s} = s\sqrt{(v_F \mathbf{p})^2 + \Delta^2}, \quad (6)
$$

where $s = \pm 1$ marks the band index. Note that the energy eigenvalues are valley degenerate.

2.2 Infinite mass boundary condition

Implementing the so-called infinite mass boundary condition (IMBC) we take up a proposal by Berry and Mondragon [58]. For this, we consider the Hamiltonian

$$H_\tau^\varphi = \mathbf{S}_\tau^\varphi \cdot \mathbf{p} + \Delta(\mathbf{r})U \tag{7}$$

(setting $v_F = \hbar = 1$ in this section), with a position-dependent mass term, $\Delta(\mathbf{r})U$, which is zero (finite) inside (outside) a circular region D, cf. Figure 1. Note that Hermiticity of the Hamiltonian in D implies $\langle \mathbf{n}_D \cdot \mathbf{j}^\tau \rangle(\mathbf{r}) = 0$ at every point $\mathbf{r}$ of the boundary ∂D. Here, $\mathbf{j}^\tau = \mathbf{S}_\tau^\varphi$ is the current density operator and $\mathbf{n}_D = (\cos \vartheta(\mathbf{r}), \sin \vartheta(\mathbf{r}))$ is the normal vector of D. Then the local boundary condition for a general wave function $\psi_\tau = (\psi_{\tau,A}, \psi_{\tau,B}, \psi_{\tau,C})$ is

$$\psi_{\tau,B}\Big|_{\mathbf{r} \in \partial D} = i\Gamma_\tau(\mathbf{r}) \Big(\cos \varphi \, e^{i\tau\vartheta(\mathbf{r})} \psi_{\tau,A}$$
$$+ \sin \varphi \, e^{-i\tau\vartheta(\mathbf{r})} \psi_{\tau,C} \Big) \Big|_{\mathbf{r} \in \partial D}. \tag{8}$$

The variable $\Gamma_\tau(\mathbf{r})$ can be obtained from the solution of the scattering problem at a planar mass step, $H_\tau^\varphi = \mathbf{S}_\tau^\varphi \cdot \mathbf{p} + \Delta\Theta(x)$, where the height of the barrier is assumed to be larger than the energy $(\Delta > |E|)$ and the Heaviside step function divides the (x, y)-plane in regions I for $x < 0$ and II for $x > 0$. In doing so, we will consider only the dispersive states, since $\langle \mathbf{j}^\tau \rangle = 0$ for the flat band states.

In region I, the wave function with wave vector $\mathbf{k} = (k_x, k_y)$ and propagation direction $\theta_\mathbf{k} = \arctan k_y/k_x$ is

$$\psi_{\tau,s}^{\mathrm{I}} = \frac{1}{\sqrt{2}} \begin{pmatrix} \tau \cos \varphi \, e^{-i\tau\theta_\mathbf{k}} \\ s \\ \tau \sin \varphi \, e^{i\tau\theta_\mathbf{k}} \end{pmatrix} e^{i\mathbf{kr}}$$
$$+ \frac{r_\tau}{\sqrt{2}} \begin{pmatrix} \tau \cos \varphi \, e^{i\tau\theta_\mathbf{k}} \\ -s \\ \tau \sin \varphi \, e^{-i\tau\theta_\mathbf{k}} \end{pmatrix} e^{i\mathbf{k'r}}. \tag{9}$$

Here, $\mathbf{k'} = (-k_y, k_x)$ denotes the wave vector of the reflected wave having a valley-dependent reflection coefficient r_τ.

In region II, the wave function takes the form

$$\psi_{\tau,s}^{\mathrm{II}} = \frac{t_\tau}{\sqrt{2}} \begin{pmatrix} \tau a_{\tau,s} \\ b_{\tau,s} \\ \tau b_{\tau,s} \end{pmatrix} \frac{e^{-qx+ik_yy}}{d_{\tau,s}}, \tag{10}$$

where t_τ denotes the valley-dependent transmission coefficient, $(k_x, k_y) = (iq, k_y)$, and

$$a_{\tau,s} = -i \cos \varphi \sqrt{(q - \tau k_y)^2 (\Delta + E)}, \tag{11}$$

$$b_{\tau,s} = \sqrt{(q^2 - k_y^2)(\Delta - E)}, \tag{12}$$

$$c_{\tau,s} = -i \sin \varphi \sqrt{(q + \tau k_y)^2 (\Delta + E)}, \tag{13}$$

$$d_{\tau,s} = \sqrt{\Delta q^2 + E k_y^2 - \tau k_y q \cos 2\varphi (\Delta + E)}. \tag{14}$$

Obviously, $\psi_{\tau,s}^{\mathrm{II}}$ is an evanescent wave perpendicular to the boundary but oscillatory along ∂D.

Enforcing the continuity of the wave function at $x = 0$,

$$\psi_{\tau,s,B}^{\mathrm{I}} = \psi_{\tau,s,B}^{\mathrm{II}}, \tag{15}$$

$$\cos \varphi \, \psi_{\tau,s,A}^{\mathrm{I}} + \sin \varphi \, \psi_{\tau,s,C}^{\mathrm{I}} = \cos \varphi \, \psi_{\tau,s,A}^{\mathrm{II}}$$
$$+ \sin \varphi \, \psi_{\tau,s,C}^{\mathrm{II}}, \tag{16}$$

and performing the limit $\Delta \to \infty$ ($q \to \infty$), we obtain

$$r_{\tau,s} = \frac{is + \cos^2 \varphi \, e^{-i\tau\theta_\mathbf{k}} + \sin^2 \varphi \, e^{+i\tau\theta_\mathbf{k}}}{is - \cos^2 \varphi \, e^{i\tau\theta_\mathbf{k}} + \sin^2 \varphi \, e^{-i\tau\theta_\mathbf{k}}}. \tag{17}$$

Since $|r_{\tau,s}|^2 = 1 \; \forall E$, the incoming wave is perfectly reflected at the boundary, regardless of τ and s. Inserting the full wave function (9) with (17) and $\mathbf{n}_D(x = 0) \equiv \mathbf{e}_x$ into equation (8), we find $\Gamma_\tau = \tau$.

Clearly the whole scattering problem can be rotated by any angle ϑ, i.e., for the $\alpha - \mathcal{T}_3$ lattice the IMBC at ∂D becomes:

$$\psi_{\tau,B} = i\tau \left(\cos \varphi \psi_{\tau,A} \, e^{i\tau\vartheta} + \sin \varphi \psi_{\tau,C} \, e^{-i\tau\vartheta} \right). \tag{18}$$

At $\alpha = 0$ we reproduce the IMBC of graphene [58].

2.3 Eigenvalue problem of the $\alpha - \mathcal{T}_3$ quantum dot in a perpendicular magnetic field

We now consider a circular quantum dot of radius R in a constant magnetic field, $\mathbf{B} = B\mathbf{e}_z$, related to the vector potential $\mathbf{A} = B/2(-y, x, 0)$. Then, using polar coordinates $(x, y) \to (r, \phi)$, the (minimal-coupling) Hamiltonian is

$$H_\tau^\varphi = v_F \mathbf{S}_\tau^\varphi \cdot (\mathbf{p} + e\mathbf{A}) + \Delta U \Theta(r - R). \tag{19}$$

In the quantum dot region D ($r < R$) we have $\Delta = 0$ and

$$H_\tau^\varphi = \tau \hbar \omega_c \begin{pmatrix} 0 & \cos \varphi L_{\tau,-} & 0 \\ \cos \varphi L_{\tau,+} & 0 & \sin \varphi L_{\tau,-} \\ 0 & \sin \varphi L_{\tau,+} & 0 \end{pmatrix}. \tag{20}$$

Here, $L_{\tau,\mp} = -ie^{\mp i\tau\phi} \left\{ \partial_\rho \pm \frac{\tau L_z}{\hbar \rho} \pm \tau \rho \right\}$, $L_z = -i\hbar \partial_\phi$, $\hbar \omega_c = \sqrt{2} \hbar v_F / l_B$, $l_B = \sqrt{\frac{\hbar}{eB}}$, and $\rho = r/\sqrt{2} l_B$. Rotational symmetry ($[H_0^\varphi, J_z] = 0$) suggests the ansatz:

$$\psi_\tau^D = \begin{pmatrix} \chi_{\tau,A} \, e^{i(m-\tau)\phi} \\ \chi_{\tau,B} \, e^{im\phi} \\ \chi_{\tau,C} \, e^{i(m+\tau)\phi} \end{pmatrix}. \tag{21}$$

With this, for the *dispersive band states*, we obtain the following differential equation for the $\chi_{\tau,B}$ component:

$$0 = \left\{ \partial_\rho^2 + \frac{1}{\rho}\partial_\rho - 2m + 4\varepsilon_\tau^2 \right.$$
$$\left. + 2\tau\cos 2\varphi - \left(\frac{m^2}{\rho^2} + \rho^2\right) \right\} \chi_{\tau,B}, \qquad (22)$$

yielding

$$\psi_{\tau,s}^D = N \begin{pmatrix} \tau\cos\varphi\rho^{-m+\tau} f_{\tau,A} e^{i(m-\tau)\phi} \\ i\varepsilon_\tau \rho^{-m} L_{n_\tau}^{-m}(\rho^2) e^{im\phi} \\ \tau\sin\varphi\rho^{-m-\tau} f_{\tau,C} e^{i(m+\tau)\phi} \end{pmatrix} e^{-\frac{\rho^2}{2}}. \qquad (23)$$

The $L_a^b(x)$ are the generalized Laguerre polynomials,

$$f_{\tau,A} = \begin{cases} -L_{n_+ -1}^{-m+1}(\rho^2), & \text{if } \tau = +1 \\ (n_- + 1)L_{n_- +1}^{-m-1}(\rho^2), & \text{if } \tau = -1 \end{cases} \qquad (24)$$

$$f_{\tau,C} = f_{-\tau,A}, \qquad (25)$$

$n_\tau = \varepsilon_\tau^2 + (\tau\cos 2\varphi - 1)/2$ is the principal quantum number, $\varepsilon_\tau^2 = (E_{\tau,s}/\hbar\omega_c)^2$, m is the total angular quantum number, and N is a normalization constant. Note that $\chi_{\tau,C} \neq \chi_{-\tau,A} \; \forall\varphi$, implying a valley asymmetry for $\alpha < 1$.

Employing now the IMBC (18) for $r = R$, where $\mathbf{n}_D = \mathbf{n}_r = (\cos\phi, \sin\phi)$, we obtain

$$0 = \cos^2\varphi\rho^{2\tau} f_{\tau,A}(\rho)$$
$$+ \sin^2\varphi f_{\tau,C}(\rho) - \varepsilon_\tau \rho^\tau L_{n_\tau}^{-m}(\rho)\Big|_{\rho=R/\sqrt{2}l_B}. \qquad (26)$$

As a result, the energy eigenvalues $E_{\tau,sn_\rho,m}$, are determined by the (positive and negative) zeros of this equation, where $n_\rho = 1, 2, 3\ldots$ is the radial quantum number. At $\alpha = 0$, these eigenvalues are related to those derived previously for graphene [39,47,55] by replacing $m \to (m-1)$.

In the large-R (or large-B) limit, we can exploit the relation between Laguerre polynomials $L_a^b(x)$ and confluent hypergeometric functions of the first kind $M(a,b,x)$:

$$L_a^b(x) = \binom{a+b}{b} M(-a, b+1, x). \qquad (27)$$

In leading order, $M(-a, b+1, x \to \infty)$ takes the form [59]:

$$M(-a, b+1, x) = \frac{\Gamma(b+1)}{\Gamma(-a)} e^x x^{-a-b-1} \left[1 + O(|x|^{-1})\right]. \qquad (28)$$

Substituting this into equation (26), we obtain $\sin(\pi n_\tau) = 0$. Consequently $n_\tau = 0, 1, 2, \ldots$ and the energy eigenvalues (Landau levels) become [30]

$$E_{\tau,n_\tau,s} = s\hbar\omega_c\sqrt{n_\tau + \frac{1}{2}(1 - \tau\cos 2\varphi)}. \qquad (29)$$

For the *flat band states*, a similar calculation gives

$$\psi_{\tau,0}^D = \begin{pmatrix} \sin\varphi\rho^{-m+\tau} f_{\tau,A} e^{i(m-\tau)\phi} \\ 0 \\ \cos\varphi\rho^{-m-\tau} f_{\tau,C} e^{i(m+\tau)\phi} \end{pmatrix} e^{-\frac{\rho^2}{2}}. \qquad (30)$$

Since $\psi_{\tau,B}^D \equiv 0$, this is always compatible with the IMBC. Clearly, $E_{\tau,0} = 0$ [cf. Eq. (5)].

3 Results and discussion

3.1 Isolated quantum dot

3.1.1 Continuum model

Figure 2 presents the analytical results for the magnetic field dependence of the energy spectra of (isolated) $\alpha - \mathcal{T}_3$ quantum dots with IMBC. For all α, we observe flat bands at $E = 0$ (red lines) and a merging of the quantum dot states to the Landau levels characterised by quantum number n_τ (dotted curves) when the magnetic field increases. Note that $n_\tau = n_\tau(n_\rho, m)$ (the data show the results for $n_\rho \leq 3$ and $|m| \leq 10$). Different from normal semiconductors, the Landau levels exhibit a square-root dependence on B [cf. Eq. (29)], i.e., they are not equidistant.

In the *graphene-lattice* model ($\alpha = 0$, top panels), we arrive at the same conclusions as previous work [47,55], also for larger total angular and radial quantum numbers. According to the IMBC, the spectra show a broken particle-hole symmetry and $E_m \neq E_{-m}$, even for $B = 0$ [where the eigenvalues are twofold degenerate ($E_\tau = E_{-\tau}$)]. For $B > 0$ time-reversal symmetry is broken and we have $E_\tau = -E_{-\tau}$. Combining the spectra of both valleys K and K', the symmetry is restored.

In the $\alpha - \mathcal{T}_3$-lattice model with $0 < \alpha < 1$ (see middle panels), the situation is the same for $B = 0$, i.e., we find $E_m \neq E_{-m}$ and valley degeneracy $E_\tau = E_{-\tau}$. Clearly time-reversal symmetry is broken at $B > 0$, but now $E_\tau \neq -E_{-\tau}$. As a consequence, the eigenvalues vary differently when B is increased. Such valley-anisotropy has been found in the magneto-optical properties of (zigzag) $\alpha - \mathcal{T}_3$ nanoribbons [34].

For the *Dice-lattice* model ($\alpha = 1$, bottom panels), we have a specific situation. Here, $E_m = E_{-m}$ at $B = 0$, i.e., the state is now fourfold degenerate. When $B > 0$ the states in each valley are still two-fold degenerate (Kramers degeneracy), and the magnetic-field dependence of the energy spectrum is the same at the K and K' points.

Let us now discuss the convergence of the eigenvalues against the Landau levels in some more detail. The first Landau level comprises all eigenvalues with $m < 0$; the higher Landau levels have contributions with $m < n_\tau$. This holds for K and K', independent of α. Obviously, the eigenvalues with positive (negative) energies cross the Landau levels first, before they converge towards these values from below (above) at the K (K') point when the magnetic field increases. The greater α, the more pronounced this kind of "overshooting" appears to be. This effect (being largest at $\alpha = 1$) is not observed for negative

Article I

Eur. Phys. J. B (2020) 93: 169   Page 5 of 11
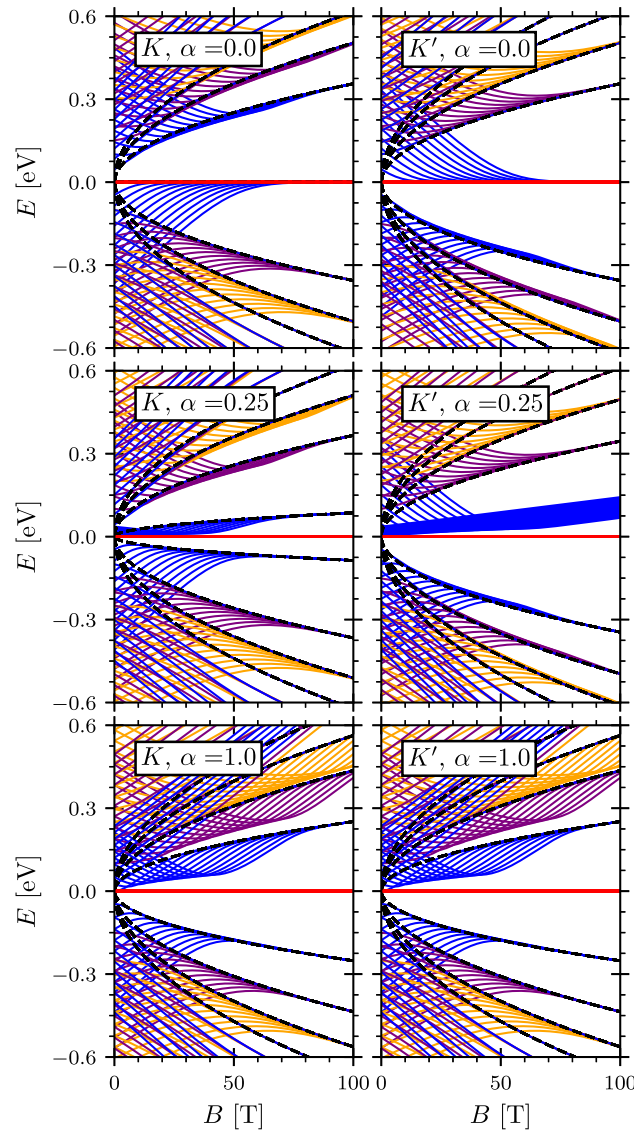
Fig. 2. Eigenvalue spectra of an $\alpha - \mathcal{T}_3$ dot with radius $R = 20$ nm. Solid lines give the solutions of (26) as a function of the perpendicular magnetic field B in valleys K (left) and K' (right) when $\alpha = 0$, 0.25, and 1 (top to bottom). Only results with $n_\rho = 1$ (blue), 2 (violet) and 3 (orange) with $-10 \leq m \leq 10$ are shown. Flat bands are marked in red. Dashed black lines give the Landau levels (29).

Fig. 3. Eigenvalue spectra of a quantum dot with $\alpha = 1/\sqrt{3}$ up to $B = 200$ T (other model parameters and notation as in Fig. 2). Inset: Magnification of solutions with $m = -3$, and $n_\rho = 1$ (blue) respectively $n_\rho = 2$ (violet), at an avoiding crossing.

(positive) energies at K (K'). We note that in certain cases the eigenvalue levels form a wide band of states and can be hardly resolved after bending up. In addition, looking for instance at the blue curves for $\alpha = 0.25$ (K' point, $E > 0$), it seems that there is no convergence of this array of curves to a Landau level. Figure 3 (right panel) shows, however, that convergence of the K'-eigenvalue sets is reached for larger values of the magnetic field. The inset demonstrates an avoided crossing for $m = -3$: While the eigenvalue belonging to $n_\rho = 1$ (blue curve) converges to the first Landau level, the eigenvalue with $n_\rho = 2$ (violet
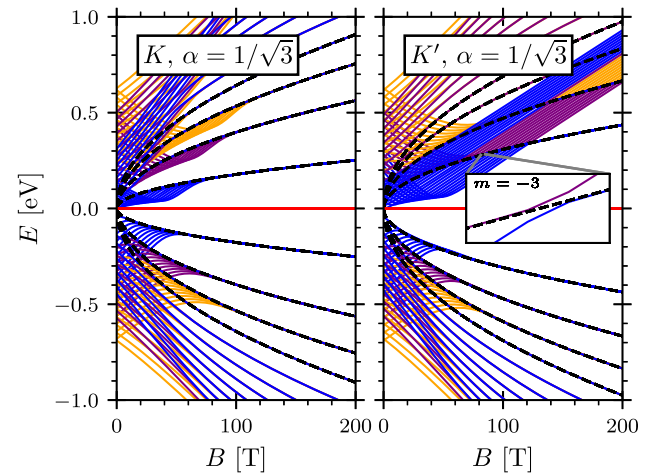
curve) tends to the second one. The same happens for the curves with other values of m.

3.1.2 Tight-binding model

We now analyse the validity range of the continuum model derived in the low-energy charge carrier regime close to the Dirac points K and K'. For this we consider the case of a circular dot imprinted on the $\alpha - \mathcal{T}_3$ lattice, whereby the dot region is not surrounded by an infinite mass medium but by a ring (of width W with finite mass potential Δ, cf. Fig. 1), which has the same lattice structure as D. In this way particularly good results can be achieved if $\Delta/t > a/W$. The eigenvalue problem of such a finite (non-interacting) system can be solved numerically, e.g., in a very efficient way by using the kernel polynomial method [60]. By the kernel polynomial method we have also direct access to the local (L) density of states (DOS),

$$\text{LDOS}(E)_i = \sum_l |\langle i|l \rangle|^2 \delta(E - E_l) \qquad (31)$$

(i is a singled out lattice site and n numbers the single-particle eigenvalues), the DOS

$$\text{DOS}(E) = \sum_n \delta(E - E_n) \,, \qquad (32)$$

and the integrated (I) DOS

$$\text{IDOS}(E) = \int_{-\infty}^{E} \text{DOS}(E') \mathrm{d}E' \,. \qquad (33)$$

Figure 4 contrasts the DOS of our quantum dot lattice model with the eigenvalues of the continuum model, in dependence on the strength of the applied magnetic
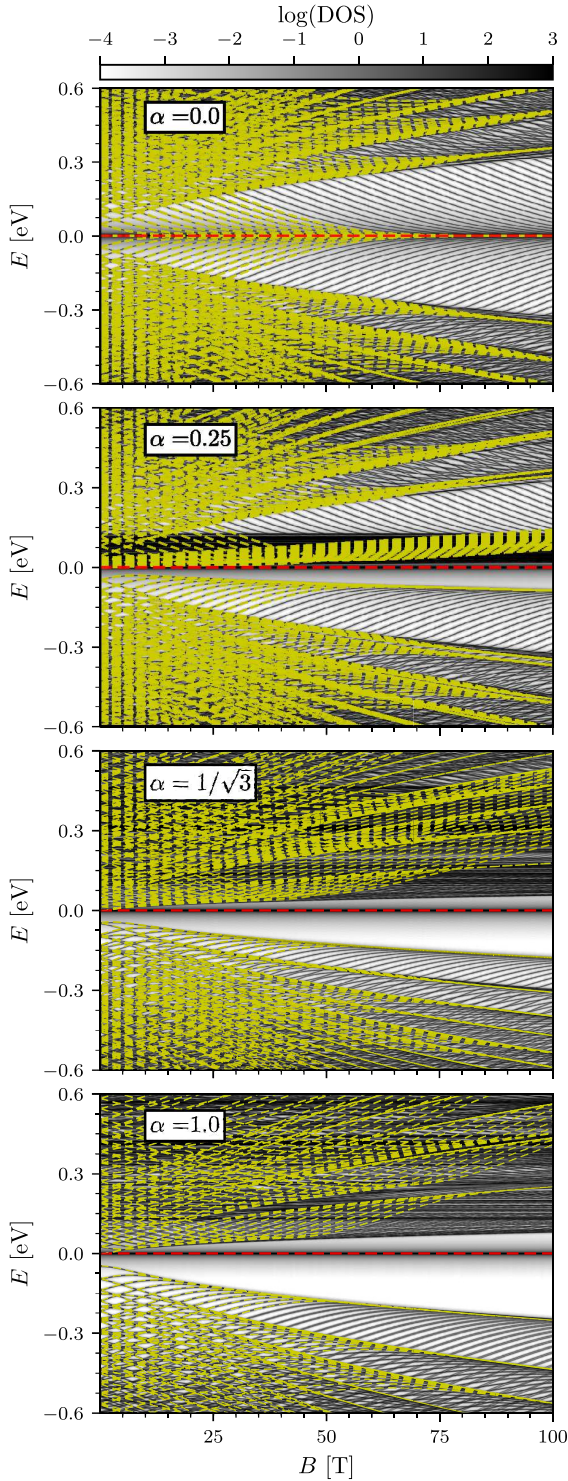
Fig. 4. Logarithmic density of states, log(DOS) (grey curves), of an $\alpha - \mathcal{T}_3$ quantum dot ($R = 20$ nm) embedded in a circular ring-barrier potential $\Delta/t = 0.8$ (width $W = 5$ nm). For comparison, the continuum model eigenvalues of Figures 2 and 3 are incorporated (yellow curves). Again the flat band is marked in red.

field B, for different values of α. In general we can say that the continuum model provides an excellent approximation to the exact data for negative energies, regardless of B and α. At this point let us emphasise once again that if we had used a negative Δ, positive and negative energy results would change roles. Comparing the data, one has to remember that the numerical exact tight-binding approach takes into account larger angular momenta (m) than our continuum model calculation; therefore additional eigenvalues will appear also for $E < 0$. In the case of graphene ($\alpha = 0$), we obtain a very good agreement also for positive energies, even though some features, such as the anti-crossing of energy levels, are not reproduced in the continuum model [55]. At finite α (and $E > 0$), the greatest difference between the continuum and tight-binding model results is the "horizontal band" of states at low energies, where the width of the band increases when α is growing. These states are mainly localised at the quantum dot's boundary (see below), and can be related to the sublattice-dependent potential Δ along ∂D. Similar "anomalous" in-gap states were also found in two-dimensional pseudospin-1 Dirac insulators and have been attributed to the boundary between two regions with different flat-band positions in a gapped Dice-lattice system [61]. The edge states in our system have the same origin: The position of the flat band is shifted by Δ when changing from region I to II.

Figure 5 compares the DOS of the tight-binding quantum-dot model and the distribution of the eigenvalues in the continuum IMBC model (with $n_\rho \leq 3$, $|m| \leq 20$) for weak and strong magnetic fields. The heights of the steps in the integrated DOS can be taken as measure of the spectral weight of the corresponding eigenstates, particularly with regard to the degeneracy of the levels (note that the IDOS is not drawn for $E > 0$ for display reasons). The figure shows once again that the main energy levels are extremely well approximated by the continuum IMBC model for $E < 0$. The sector $E > 0$ is reproduced less accurately, obviously there are many states which are not taken into account within the continuum approach. For weak magnetic fields ($B = 2$ T, upper panel), the Landau levels are more difficult to identify. For high magnetic fields ($B = 140$ T, lower panel), states with large angular quantum numbers m contribute to each Landau level. Note that we have included in the figure series of states which are not yet converged for the n_ρ- and m-values used (vertical dashed yellow lines).

3.2 Contacted quantum dot

We now consider a more realistic situation, where the $\alpha - \mathcal{T}_3$ quantum dot is contacted by leads. The boundary of this "device" is realised covering the whole setup by a sheath of width W with a gapful band structure due to a (finite) mass term Δ, see Figure 6. To determine the conductance between the left (L) and right (R) leads in the limit of vanishing bias voltage, we employ the Landauer-Büttiker approach [62]:

$$G = G_0 \sum_{m \in \mathrm{L}, n \in \mathrm{R}} |S_{n,m}|^2 \qquad (34)$$
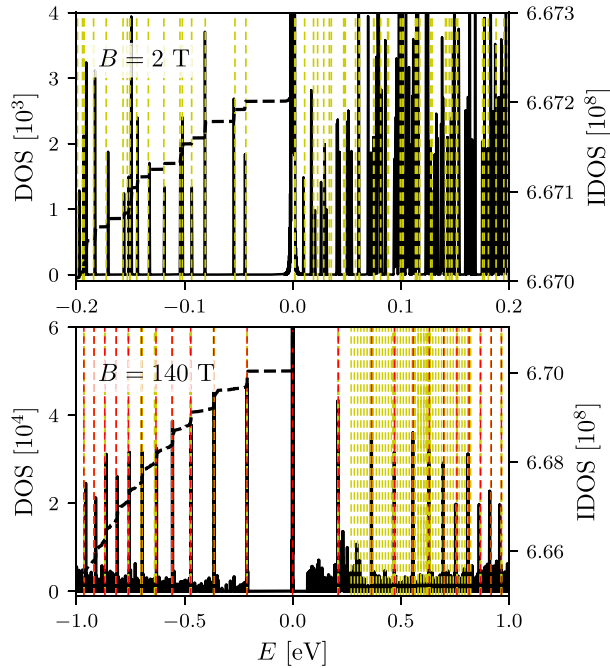
Fig. 5. DOS (black lines, left axis) and integrated DOS (dashed lines, right axis; included for $E \leq 0$ only) of an $\alpha - \mathcal{T}_3$ quantum dot (where $\alpha = 1/\sqrt{3}$) in a perpendicular magnetic fields: $B = 2$ T (upper panel) and $B = 140$ T (lower panel). Yellow vertical lines mark the energy eigenvalues of the continuum model with IMBC. For $B = 140$ T, the Landau levels are included (red lines). Other model parameters are as in Figure 4.
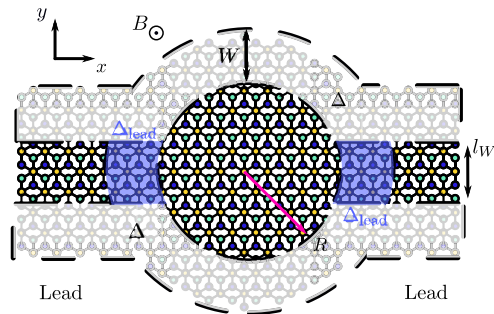

Fig. 6. Drawing of the $\alpha - \mathcal{T}_3$ lattice quantum dot (radius R) contacted by leads (width l_W). The boundary condition is realised by a W-wide stripe with mass term Δ that covers the whole element. The leads are docked by an additional mass term Δ_{lead} (blue region); the homogenous magnetic field B points out of the plane. In the calculations we use $R = 20$ nm, $\Delta/t = 0.5$, $W = 5$ nm, and $l_W = 80\sqrt{3}a - 2W$.

with $G_0 = 2e^2/h$. G_0 is the maximum conductance per channel. The scattering matrix between all open (i.e., active) lead channels, $S_{n,m}$, can be easily calculated with the help of the `Phyton`-based toolbox `Kwant` [63].

Figure 7 shows the conductance of the contacted $\alpha - \mathcal{T}_3$ quantum dot as a function of energy at weak (upper panel) and strong (lower panel) magnetic fields. The conductance essentially probes the extended (current-carrying) states
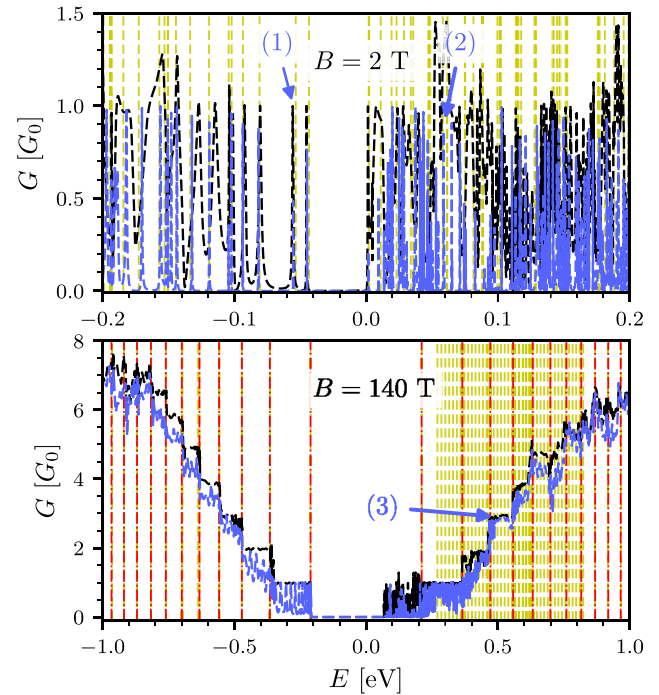
Fig. 7. Conductance of the contacted $\alpha - \mathcal{T}_3$ quantum dot with $\alpha = 1/\sqrt{3}$ as a function of energy for $B = 2$ T (top) and $B = 140$ T (bottom). The other dot parameters are as indicated in Figure 6. Results for $\Delta_{\text{lead}} = 0$ ($\Delta_{\text{lead}} = 0.2$ eV) are shown in black (blue). Yellow vertical lines are those included in Figure 5 as well. Landau levels are marked by red lines. The LDOS for the selected signatures (1), (2) and (3) is given in Figure 8 below.

of the dot. Again, we choose $\alpha = 1/\sqrt{3}$, in order to allow for a direct comparison with the DOS data of the isolated dot depicted in Figure 5. Let us first consider the case $\Delta_{\text{lead}} = 0$ (black dashed lines). For $B = 2$ T, we see that the first five peaks at $E < 0$ can be assigned to the eigenvalues of the continuum model for the isolated dot. For larger negative energies the conductance resonances will start to overlap, resulting in broader peaks, more specifically bands. In this range the rotation symmetry is completely destroyed by the contacts, and m is not a good quantum number anymore. For positive energies we recognise larger deviations from the continuum eigenvalues as is the case for the DOS (cf. Fig. 5); overall much more conductive channels appear. At $B = 140$ T, we observe the expected Landau level quantisation of the conductance. Obviously, the steps respectively plateaus are less pronounced at positive and larger absolute values of the energy once again. The conductance quantisation basically breaks down if the cyclotron diameter $d_c = 2|E|/v_F eB$ exceeds the lead width l_W; in this case the charge carriers, moving on a cyclotron trajectory along the quantum dot circumference, will miss the way out at the right lead.

Working with additional barriers at the lead contacts ($\Delta_{\text{lead}} = 0.2$ eV, blue dashed lines), the conductance resonances are sharpened to some extent. This is because the
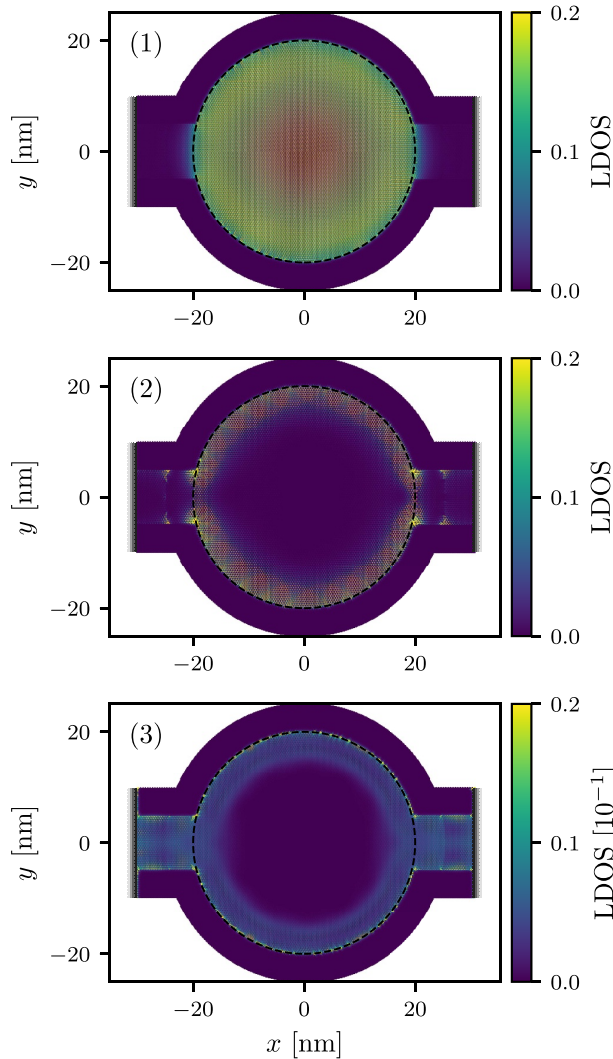
Fig. 8. LDOS for the contacted $\alpha - \mathcal{T}_3$ quantum dot at the resonances indicated in Figure 7 by (1), (2) [$B = 2$ T; two upper panels] and (3) [$B = 140$ T; lowest panel] for $\Delta_{\text{lead}} = 0.2$ eV. Remaining parameters given in Figure 6. The dashed line marks the dot boundary.

Fig. 9. LDOS of the contacted $\alpha - \mathcal{T}_3$ quantum dot surrounded by a disordered circular ring. The LDOS is shown for a single (but typical) realisation of the random mass term, where the Δ_i are drawn out of the interval [0,1.6], i.e., $\hat{\Delta} = 0.8$. Again we consider the resonances (1), (2) [$B = 2$ T; two upper panels] and (3) [$B = 140$ T; lowest panel] with system parameters as in Figures 6, 7 and 8.

dot region now is more self-contained. Of course, the transmission of the device is reduced in total when the barrier becomes too high (we have backscattering effects and, disregarding Klein tunnelling, only evanescent particle waves will enter the dot region).

Further information about the nature of the states belonging to specific resonances can be obtained from the LDOS. Figure 8 records and visualises the spatial variation of the LDOS at the (resonance) energies $E = -0.055$ eV (1), $E = 0.059$ eV (2) and $E = 0.5$ (3) for $B = 2$ T and $B = 140$ T, respectively. For (1), the LDOS is almost rotationally symmetric (owing to the leads there is some weak asymmetry) and has a maximum at the centre of the quantum dot. This is in accord with the corresponding continuum solution ($m = 0$, $sn_\rho = -1$ and $\tau = -1$), which according to equation (23) has no angle dependence.
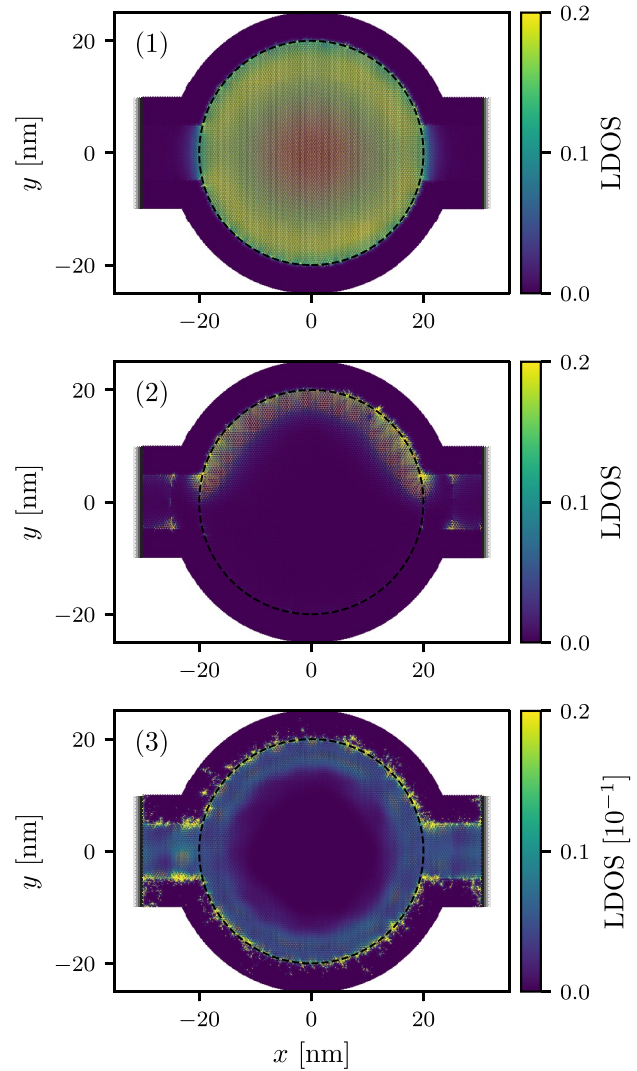
Resonances at higher energy, belonging to larger values of m, will lead to more complicated LDOS pattern (not shown). For (2), the LDOS is more or less localised at the boundary of the quantum dot, i.e., this resonance will not correspond to a bulk state as (1). Note that we find almost the same conductances, $G/G_0 \simeq 0.98$ (1) and $G/G_0 \simeq 1$ (2), which indicates that we have one perfect current carrying (bulk or edge) state. In both cases, we observe some scattering and "localisation" effects at the edges of the (lead) mass barrier. At resonance (3), the LDOS at the quantum dot boundary is also much larger than those in the bulk (although by a factor of ten smaller compared to cases (1) and (2); note the different scale of the color bar).
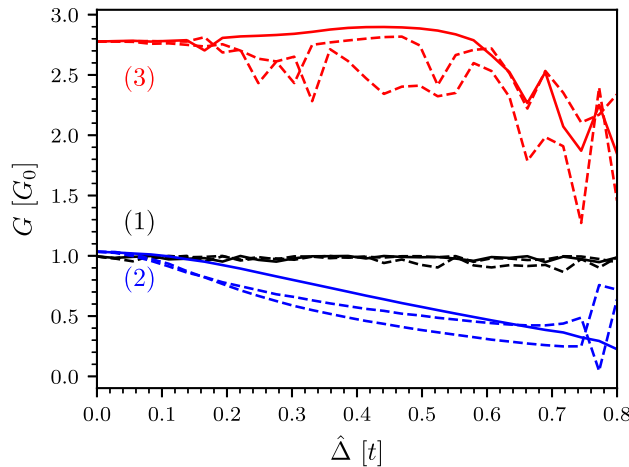
Fig. 10. Conductance G/G_0 for the resonances (1) [black curves], (2) [blue curves] and (3) [red curves] (cf., Fig. 7) calculated at different (discrete) disorder strengths $\hat{\Delta}$. Results obtained for the disorder realisation used in Figure 9 (two other disorder realisations) are marked by solid (dashed) lines, which should guide the viewer's eye only. All other parameters are as in the previous figures.

Regardless of this, $G/G_0 \simeq 2.9$, i.e., we have almost three perfect transport channels. In this case we already entered the quantum Hall regime, where quantum Hall edge states evolve which differ in nature from the edge state (2).

3.3 Disorder effects

As a matter of course, imperfections will strongly influence the transport through contacted Dirac-cone systems [57,64,65]. This holds true even up to the point of complete suppression, e.g., by Anderson localisation [66]. Nevertheless most of these nanostructures appear to be conducting [67,68], simply because the (Anderson) localisation length exceeds the device dimensions for weak disorder in one or two dimensions [67,68]. In our case, the disorder caused by the boundary of the quantum dot is of particular importance. To model these disorder effects, we let the mass term fluctuate in the circular ring of width W. More precisely, we assume $\Delta \rightarrow \Delta_i$ in equation (1), where Δ_i is evenly distributed in the interval $[\Delta - \hat{\Delta}, \Delta + \hat{\Delta}]$ with $\hat{\Delta} < \Delta$, i.e., $\hat{\Delta} > 0$ measures the disorder strength. We note that only suchlike short-range disorder causes intervalley scattering, and thus may lead to Anderson localisation [69]. This holds at least in the case $\alpha = 0$ (graphene) and within the Dirac approximation. Long-range disorder, on the other hand, gives rise to intravalley scattering which is not sufficient to localise the charge carriers [70].

Figure 9 illustrates how the LDOS shown in Figure 8 for three characteristic resonances will change if we randomise the mass potential Δ_i with strength $\hat{\Delta} = 0.8$ in the ring covering the quantum dot. For this we have chosen a randomly selected but from a physical perspective typical realisation (sample) and followed the resonances (1), (2) and (3) by increasing $\hat{\Delta}$ from zero to its final

value 0.8. Thereby the positions of the resonances (1) and (2) are slightly shifted compared to the ordered case: We find $E = -0.057$ eV (1) and $E = 0.058$ eV (2) for the sample used in Figure 9. Since the plateau structure is completely destroyed for the (disordered) high-field case $B = 140$ T, we will leave $E = 0.5$ eV (3). It is obvious that the LDOS of the "bulk-state" resonance (1) is not changed much by the edge disorder (upper panel). This is also reflected in the conductance $G/G_0(\hat{\Delta} = 0.8) = 0.93 \simeq G/G_0(0)$. A completely different behaviour is observed for the "edge-state" resonance (2). Here the LDOS is not homogeneously distributed along the periphery region anymore. Instead we find an imbalance between energy states (and associated transport channels) in the upper and lower half of the quantum dot, which depends on the specific sample of course. For other realisations the LDOS will be larger in the lower half of the quantum dot. In any case the conductance is substantially reduced, however, for example, we have $G/G_0(\hat{\Delta} = 0.8) = 0.54$ for the depicted realisation. The effect of the disorder is similarly strong for the quantum Hall edge-state resonance (3), $G/G_0(\hat{\Delta} = 0.8) = 1.85$, but here the LDOS is uniformly spread about the upper and lower halves of the quantum dot. Interestingly, it appears that now states can penetrate more deeply into the barrier region.

Finally, we show in Figure 10 how the conductance depends on the disorder strength $\hat{\Delta}$, for resonances (1), (2) and (3) and three different disorder realisations each. Despite the strong fluctuations at larger values of $\hat{\Delta}$, which clearly result from large local differences of the onsite energies and a varying overlap of energetically adjacent states, one observes a noticeable reduction of the conductance for the states (2) and (3) located primarily near the quantum dot boundary whereas the conductance of the bulk state (1) is only little affected. Since the spatial dimensions of the device are in the nanoscale regime, the conductance of our setup is not self-averaging. Determining the probability distribution for the LDOS and conductances from a large assembly of disorder realisations [71] could be a promising approach to deal with this problem, but this is beyond the scope of the present work.

4 Conclusions

To summarise, we considered a generalisation of both graphene and Dice lattices, the so-called $\alpha - \mathcal{T}_3$ lattice, and studied the electronic properties of a quantum dot, imprinted on this material, in a perpendicular static magnetic field. The quantum dot boundary condition was implemented in a consistent manner by an infinite mass term (circular ring having a finite band gap) in the continuum (tight-binding model) description. For an isolated quantum dot we analysed the magnetic-field dependence of the eigenvalue spectra at the K and K' Dirac nodal points and demonstrated significant differences between the graphene, Dice and $\alpha - \mathcal{T}_3$ continuum model results, particularly with respect to the degeneracy and the convergence towards the Landau levels at high fields. The comparison of our analytical results with exact numerical data for the $\alpha - \mathcal{T}_3$ tight-binding lattice shows that the

states with negative band energies were generally satisfactory reproduced (if not too far away from the neutral point), whereas the lattice effects play a more prominent role at positive energies. For a contacted quantum dot, our transport calculations confirm the existence of transport channels, i.e., current carrying states, at weak magnetic fields, and Landau level quantisation of the conductance (related to quantum Hall edge states) at larger fields. The local density of states reveals the different physical nature of these states. The LDOS not only indicates how the boundary and the contacts affect the electronic structure, but also how disorder in the quantum dot's surrounding will influence its transport behaviour. While transport channels related to bulk resonances were less impacted, edge channel resonance and quantum hall edge states are strongly affected, giving rise to a significant reduction of the conductance.

All in all, we are optimistic that the (strong) magneto-response of valley-contrasting quasiparticles in $\alpha - \mathcal{T}_3$ model materials provides a good basis for promising valleytronics applications in near future.

Author contribution statement

Both authors contributed equally to this work.

Publisher's Note The EPJ Publishers remain neutral with regard to jurisdictional claims in published maps and institutional affiliations.

References

1. L. Yang, C.-H. Park, Y.W. Son, M.L. Cohen, S.G. Louie, Phys. Rev. Lett. **99**, 186801 (2007)
2. S. Russo, J.B. Oostinga, D. Wehenkel, H.B. Heersche, S.S. Sobhani, L.M.K. Vandersypen, A.F. Morpurgo, Phys. Rev. B **77**, 085413 (2008)
3. J.R. Williams, L. DiCarlo, C.M. Marcus, Science **317**, 638 (2016)
4. L.A. Ponomarenko, F. Schedin, E.W.H.M.I. Katsnelson, R. Yang, K.S. Novoselov, A.K. Geim, Science **320**, 356 (2008)
5. J.Y. Vaishnav, J.Q. Anderson, J.D. Walls, Phys. Rev. B **83**, 165437 (2011)
6. J.M. Caridad, S. Connaughton, C. Ott, H.B. Weber, V. Krstìc, Nat. Commun. **7**, 12894 (2016)
7. D. Gunlycke, D.A. Areshkin, J. Li, J.W. Mintmire, C.T. White, Nano Lett. **7**, 3608 (2007)
8. P. Zhao, J. Guo, J. Appl. Phys. **105**, 034503 (2009)
9. J. Güttinger, F. Molitor, C. Stampfer, S. Schnez, A. Jacobsen, S. Dröscher, T. Ihn, K. Ensslin, Rep. Prog. Phys. **75**, 126502 (2012)
10. R.V. Gorbachev, A.S. Mayorov, A.K. Savchenko, D.W. Horsell, F. Guinea, Nano Lett. **8**, 1995 (2008)
11. O. Klein, Z. Phys. **53**, 157 (1928)
12. M.I. Katsnelson, K.S. Novoselov, A.K. Geim, Nat. Phys. **2**, 620 (2006)
13. B. Trauzettel, Y.M. Blanter, A.F. Morpurgo, Phys. Rev. B **75**, 035305 (2007)
14. C. Wurl, H. Fehske, Phys. Rev. A **98**, 063812 (2018)
15. J.H. Bardarson, M. Titov, P.W. Brouwer, Phys. Rev. Lett. **102**, 226803 (2009)
16. H. Fehske, G. Hager, A. Pieper, Phys. Status Solidi B **252**, 1868 (2015)
17. B. Brun, N. Moreau, S. Somanchi, V.H. Nguyen, K. Watanabe, T. Taniguchi, J.C. Charlier, C. Stampfer, B. Hackens, Phys. Rev. B **100**, 041401 (2019)
18. R. Heinisch, F.X. Bronold, H. Fehske, Phys. Rev. Lett. **109**, 243903 (2012)
19. J. Cserti, A. Pályi, C. Péterfalvi, Phys. Rev. Lett. **99**, 246801 (2007)
20. R.L. Heinisch, F.X. Bronold, H. Fehske, Phys. Rev. B **87**, 155409 (2013)
21. A. Pieper, R. Heinisch, H. Fehske, Europhys. Lett. **104**, 47010 (2013)
22. M.M. Asmar, S.E. Ulloa, Phys. Rev. Lett. **112**, 136602 (2014)
23. J.S. Wu, M.M. Fogler, Phys. Rev. B **90**, 235402 (2014)
24. A. Filusch, C. Wurl, H. Fehske, Eur. Phys. J. B. **93**, 59 (2020)
25. Y. Zhang, Y.W. Tan, H.L. Stormer, P. Kim, Nature **438**, 201 (2005)
26. D. Smirnov, H. Schmidt, R.J. Haug, Appl. Phys. Lett. **100**, 203114 (2008)
27. B. Sutherland, Phys. Rev. B **34**, 5208 (1986)
28. J. Vidal, R. Mosseri, B. Douçot, Phys. Rev. Lett. **81**, 5888 (1998)
29. B. Dóra, J. Kailasvuori, R. Moessner, Phys. Rev. B **84**, 195422 (2011)
30. A. Raoux, M. Morigi, J.N. Fuchs, F. Piéchon, G. Montambaux, Phys. Rev. Lett. **112**, 026402 (2014)
31. R. Shen, L.B. Shao, B. Wang, D.Y. Xing, Phys. Rev. B **81**, 041410 (2010)
32. D.F. Urban, D. Bercioux, M. Wimmer, W. Häusler, Phys. Rev. B **84**, 115136 (2011)
33. S.K. Firoz Islam, P. Dutta, Phys. Rev. B **96**, 045418 (2017)
34. Y.R. Chen, Y. Xu, J. Wang, J.F. Liu, Z. Ma, Phys. Rev. B **99**, 045420 (2019)
35. M. Orlita, D.M. Basko, M.S. Zholudev, F. Teppe, W. Knap, V.I. Gavrilenko, N.N. Mikhailov, S.A. Dvoretskii, P. Neugebauer, C. Faugeras et al., Nat. Phys. **10**, 233 (2015)
36. J.D. Malcolm, E.J. Nicol, Phys. Rev. B **92**, 035118 (2015)
37. M. Rizzi, V. Cataudella, R. Fazio, Phys. Rev. B **73**, 144511 (2006)
38. P.A.M. Dirac, Proc. R. Soc. Lond. A **117**, 610 (1928)
39. S. Schnez, K. Ensslin, M. Sigrist, T. Ihn, Phys. Rev. B **78**, 195427 (2008)
40. R. Jackiw, A.I. Milstein, S.Y. Pi, I.S. Terekhov, Phys. Rev. B **80**, 033413 (2009)

41. D. Bercioux, D.F. Urban, H. Grabert, W. Häusler, Phys. Rev. A **80**, 063603 (2009)
42. M. Vigh, L. Oroszlány, S. Vajna, P. San-Jose, G. Dávid, J. Cserti, B. Dóra, Phys. Rev. B **88**, 161413 (2013)
43. Y. Betancur-Ocampo, G. Cordourier-Maruri, V. Gupta, R. de Coss, Phys. Rev. B **96**, 024304 (2017)
44. H.Y. Xu, Y.C. Lai, Phys. Rev. B **94**, 165405 (2016)
45. E.A. Stepanov, V.C. Zhukovsky, Phys. Rev. B **94**, 094101 (2016)
46. E. Illes, E.J. Nicol, Phys. Rev. B **95**, 235432 (2017)
47. M.R. Thomsen, T.G. Pedersen, Phys. Rev. B **95**, 235427 (2017)
48. R. Zhu, C. Cai, J. Appl. Phys. **122**, 124302 (2017)
49. C.Z. Wang, H.Y. Xu, L. Huang, Y.C. Lai, Phys. Rev. B **96**, 115440 (2017)
50. O.V. Bugaiko, D.O. Oriekhov, J. Phys.: Condens. Matter **31**, 325501 (2019)
51. D. Huang, A. Iurov, H.Y. Xu, Y.C. Lai, G. Gumbs, Phys. Rev. B **99**, 245412 (2019)
52. H.Y. Xu, Y.C. Lai, Phys. Rev. Res. **2**, 013062 (2020)
53. C.D. Han, H.Y. Xu, Y.C. Lai, Phys. Rev. Res. **2**, 013116 (2020)
54. A.R. Akhmerov, C.W.J. Beenakker, Phys. Rev. B **77**, 085423 (2008)
55. M. Grujić, M. Zarenia, A. Chaves, M. Tadić, G.A. Farias, F.M. Peeters, Phys. Rev. B **84**, 205441 (2011)
56. J. Wurm, M. Wimmer, H.U. Baranger, K. Richter, Semicond. Sci. Technol. **25**, 034003 (2010)
57. A. Filusch, C. Wurl, A. Pieper, H. Fehske, J. Low Temp. Phys. **191**, 259 (2018)
58. M.V. Berry, R. Mondragon, Proc. R. Soc. Lond. A **412**, 53 (1987)
59. M. Abramowitz, I.A. Stegun, *Handbook of Mathematical Functions with formulas, graphs, and mathematical tables* (Dover, New York, 1970)
60. A. Weiße, G. Wellein, A. Alvermann, H. Fehske, Rev. Mod. Phys. **78**, 275 (2006)
61. H.Y. Xu, Y.C. Lai, Phys. Rev. Res. **2**, 023368 (2020)
62. P.S. Davids, Phys. Rev. B **52**, 4146 (1995)
63. C.W. Groth, M. Wimmer, A.R. Akhmerov, X. Waintal, New J. Phys. **16**, 063065 (2014)
64. G. Schubert, H. Fehske, Phys. Rev. Lett. **108**, 066402 (2012)
65. A. Pieper, G. Schubert, G. Wellein, H. Fehske, Phys. Rev. B **88**, 195409 (2013)
66. P.W. Anderson, Phys. Rev. **109**, 1492 (1958)
67. G. Schubert, J. Schleede, H. Fehske, Phys. Rev. B **79**, 235116 (2009)
68. J. Schleede, G. Schubert, H. Fehske, Europhys. Lett. **90**, 17002 (2010)
69. H. Suzuura, T. Ando, Phys. Rev. Lett. **89**, 266603 (2002)
70. J.H. Bardarson, J. Tworzydło, P.W. Brouwer, C.W.J. Beenakker, Phys. Rev. Lett. **99**, 106801 (2007)
71. G. Schubert, J. Schleede, K. Byczuk, H. Fehske, D. Vollhardt, Phys. Rev. B **81**, 155106 (2010)

Valley filtering in strain-induced α-$\mathcal{T}_3$ quantum dots

Alexander Filusch [1], Alan R. Bishop,[2] Avadh Saxena [3], Gerhard Wellein,[4] and Holger Fehske [1,*]

[1]*Institut für Physik, Universität Greifswald, 17487 Greifswald, Germany*
[2]*Science, Technology and Engineering Directorate, Los Alamos National Laboratory, Los Alamos, New Mexico 87545, USA*
[3]*Theoretical Divison, Los Alamos National Laboratory, Los Alamos, New Mexico 87545, USA*
[4]*Department of Computer Science, Friedrich-Alexander-Universität Erlangen-Nürnberg, 91058 Erlangen, Germany*

We test the valley-filtering capabilities of a quantum dot inscribed by locally straining an α-$\mathcal{T}_3$ lattice. Specifically, we consider an out-of-plane Gaussian bump in the center of a four-terminal configuration and calculate the generated pseudomagnetic field having an opposite direction for electrons originating from different valleys, the resulting valley-polarized currents, and the conductance between the injector and collector situated opposite one another. Depending on the quantum dot's width and width-to-height ratio, we detect different transport regimes with and without valley filtering for both the α-$\mathcal{T}_3$ and dice lattice structures. In addition, we analyze the essence of the conductance resonances with a high valley polarization in terms of related (pseudo-) Landau levels, the spatial distribution of the local density of states, and the local current densities. The observed local charge and current density patterns reflect the local inversion symmetry breaking by the strain, besides the global inversion symmetry breaking due to the scaling parameter α. By this way we can also filter out different sublattices.

I. INTRODUCTION

In the emerging field of "valleytronics," the valley degree of freedom is used to distinguish and designate quantum states of matter. For this, the band structure of the system must have at least two inequivalent valleys that take over the role of charge or spin in more traditional electronics and spintronics. Two-dimensional condensed-matter materials, such as graphene or semiconducting transition metal dichalcogenides, host an easily accessible electronic valley degree of freedom to encode information [1–3]. In this respect graphene-based valleytronics seems to be particularly promising. This is mostly because of graphene's striking electronic properties [4], including Dirac-cone functionality which can be tuned by applying external electric fields, even in restricted areas, e.g., by top gates [5]. Another advantage is that diverse graphene nanostructures such as ribbons, rings, quantum dots, or junctions can be manufactured without major problems, whereby transport through these "devices" strongly depends on the geometry of the sample and its edge shape [6].

Graphene-based structures also sustain a large amount of strain without breaking because of their strong (planar) covalent sp^2 bonds [7]. In graphene, the coupling between the mechanical deformation and electronic structure has remarkable consequences: It introduces an effective gauge field in the low-energy Dirac spectrum. The associated pseudomagnetic field (PMF) has been demonstrated in scanning tunneling microscopy (STM) experiments [8], which reveal Landau level (LL) quantization. Most notably, strain-induced PMFs con-

serve time-reversal symmetry, unlike real magnetic fields, and therefore point in opposite directions in graphene's inequivalent valleys **K** and **K**′ related by time-reversal symmetry [9]. This sign difference together with a spatially varying PMF forms the basis for theoretical proposals to manipulate the valley degree of freedom in graphene-based structures by nanoscale strain engineering [10–14]. In experiments, such local deformation fields can be produced and controlled by STM tips [15]. Breaking the valley degeneracy and spatially separating the electrons from different valleys is clearly a prerequisite for every form of valleytronics. In this context, it has been shown that Gaussian bumps lead to different real-space trajectories for **K** and **K**′ electrons, and therefore can act as valley filters and beam splitters [10,13,16,17].

The combination of strain, Dirac-cone physics, and flat-band physics in a modified α-$\mathcal{T}_3$ lattice structure is an interesting case to study, not only because the flat band then crosses the nodal Dirac points with peculiar consequences for the Berry phase [18], Klein tunneling [19], Weiss oscillations [20], or LL quantization [21], but also regarding the interplay between the local inversion symmetry breaking by strain and the global one by α. In the α-$\mathcal{T}_3$ structure one of the inequivalent sites of the honeycomb lattice is connected to a site located in the center of the hexagons with strength α, i.e., in a certain sense this system interpolates between graphene ($\alpha = 0$) and dice ($\alpha = 1$) lattices [22]. The dice lattice can be fabricated by growing trilayers of cubic lattices, e.g., $SrTiO_3/SrIrO_3/SrTiO_3$, in the (111) direction [23]. An α-$\mathcal{T}_3$ lattice with an intermediate scaling parameter $\alpha = 1/\sqrt{3}$ has been reported for $Hg_{1-x}Cd_xTe$ at a critical doping [18,24]. Optical lattice realizations of the α-$\mathcal{T}_3$ structure that would allow tuning of α have been also suggested [18,24]. Based on

---

*fehske@physik.uni-greifswald.de

this background, it is not surprising that there have been recent activities to exploit valley filtering in the α-$\mathcal{T}_3$ and dice models to realize, for example, a geometric valley-Hall effect [25] or magnetic Fabry-Pérot interferometry [26]. Nevertheless, the role of nonuniform strain in confined (open) α-$\mathcal{T}_3$ nanostructures is still widely unexplored, especially with regard to the above-mentioned combination of local and global inversion symmetry breaking.

In this paper, we address this issue by investigating the transmission of particles through a quantum dot created by an out-of-plane centrosymmetric deformation of an α-$\mathcal{T}_3$ lattice in the center of a four-terminal configuration with zigzag terminations. In Sec. II we introduce our model and discuss the basic impact of the strain-induced PMF with trigonal symmetry in a continuum approach, allowing for an analytical treatment. In particular, taking into account the first-order corrections to the transfer integrals only, we can determine the (pseudo-) Landau levels (LLs) and specify their valley dependence with regard to filtering effects. To also investigate highly strained samples of any geometry and with specific boundaries, we numerically solve the full (tight-binding) lattice-model problem in Sec. III. For this, we employ the Landauer-Büttiker scattering matrix [27] and kernel polynomial [28] approaches. Using the KWANT toolbox [29], we analyze the conductance, the valley polarization, and the local charge and current densities. The results will be discussed with a perspective of potential device applications. Our conclusions are found in Sec. IV.

II. THEORETICAL APPROACH

We start from a tight-binding description of the α-$\mathcal{T}_3$ lattice by the Hamiltonian

$$H^\alpha = -\sum_{\langle ij \rangle} t_{ij} a_i^\dagger b_j - \alpha \sum_{\langle ij \rangle} t_{ij} b_i^\dagger c_j, \quad (1)$$

where $a^{(\dagger)}$, $b^{(\dagger)}$, and $c^{(\dagger)}$ annihilate (create) an electron in a Wannier state centered at site A, B, and C, respectively. The hopping scaling parameter α interpolates between the honeycomb graphene lattice ($\alpha = 0$) and the dice lattice ($\alpha = 1$) [see Fig. 1(a)]. In the pristine case, the transfer amplitude of particles between nearest-neighbor sites becomes $t_{ij} = t$. Rescaling the energy by $\cos\varphi$, where $\tan\varphi = \alpha$, the Fourier transformed Hamiltonian (1) takes the form

$$H^\alpha = \sum_{\mathbf{k}} \psi_{\mathbf{k}}^\dagger \begin{pmatrix} 0 & \cos\varphi f_{\mathbf{k}} & 0 \\ \cos\varphi f_{\mathbf{k}}^* & 0 & \sin\varphi f_{\mathbf{k}} \\ 0 & \sin\varphi f_{\mathbf{k}}^* & 0 \end{pmatrix} \psi_{\mathbf{k}} \quad (2)$$

in $\mathbf{k}$ space with $\psi_{\mathbf{k}} = (a_{\mathbf{k}}, b_{\mathbf{k}}, c_{\mathbf{k}})$ and

$$f_{\mathbf{k}} = -\sum_{j=1}^{3} t_j e^{-i\mathbf{k}\cdot\boldsymbol{\delta}_{A,j}'}. \quad (3)$$

We now consider a lattice distortion by a strain field $\mathbf{u}(x, y) = [u_x, u_y, u_z \equiv h(x, y)]$. Then the displaced lattice coordinates $\mathbf{r}' = \mathbf{r} + \mathbf{u}$ and the bond lengths vary according to $d_{ij} = |\mathbf{r}_i' - \mathbf{r}_j'|$, yielding bond-dependent transfer integrals:

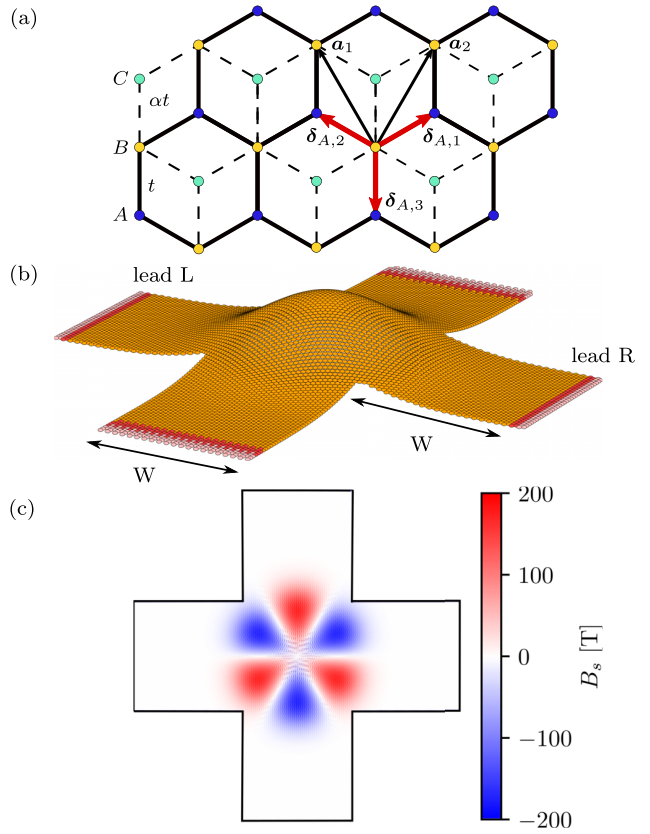$$t_{ij} = t \exp\{-\beta(d_{ij}/a - 1)\}. \quad (4)$$

FIG. 1. (a) Pristine α-$\mathcal{T}_3$ lattice with basis $\{A, B, C\}$ and Bravais lattice vectors $\mathbf{a}_1$ and $\mathbf{a}_2$. Neighboring sites are connected by vectors $\boldsymbol{\delta}_{A,j}$ ($j = 1, 2, 3$); the transfer amplitudes on A-B and B-C bonds are t and αt, respectively. (b) Four-terminal configuration with a quantum dot generated by the Gaussian deformation (16), where $H = 17.9$ nm, $\sigma = 20$ nm, and $W = 50$ nm. (c) Strain-induced pseudo-magnetic field calculated for electrons residing in the **K** valley. These electrons can pass the quantum dot from L to R whereas electrons stemming from the **K**$'$ valley will be reflected.

In Eq. (4), $\beta = -\partial \log t / \partial \log a$ is the Grüneisen parameter with a being the lattice constant of the unstrained lattice. These equations will be the basis for the exact numerical study carried out in Sec. III.

At first, however, let us perform some theoretical considerations for an easier interpretation of the results below. If the strain is weak, we only need to take into account first-order corrections to the hopping parameter:

$$t_j \simeq t\left(1 - \frac{\beta}{a^2}\Delta_j\right). \quad (5)$$

Here, $\Delta_j = \boldsymbol{\delta}_{A,j} \underline{\epsilon} \boldsymbol{\delta}_{A,j}$, where the strain tensor $\underline{\epsilon}$ is given as

$$(\underline{\epsilon})_{ij} = \partial_i u_j + \partial_j u_i + (\partial_i h)(\partial_j h), \quad i, j = x, y, \quad (6)$$

in the framework of continuum theory. Neglecting other influences of the strain, in the vicinity of the Dirac points $\mathbf{K}^{(\prime)} = (\tau \frac{4\pi}{3\sqrt{3}a}, 0)$ with $\tau = 1$ ($\tau = -1$), we have

$$f_{\mathbf{K}^{(\prime)}+\mathbf{q}} \simeq \frac{3at}{2}(\tau q_x - iq_y) + \sum_{j=1}^{3} \frac{\beta t}{a^2}\Delta_j(1 + i\mathbf{q}\cdot\boldsymbol{\delta}_{A,j})e^{i\mathbf{K}^{(\prime)}\cdot\boldsymbol{\delta}_{A,j}}. \quad (7)$$

Inserting this expansion into Eq. (2), we find

$$H_\tau^\varphi = \hbar v_{\rm F} \mathbf{S}_\tau^\varphi \cdot \left(\mathbf{q} + \frac{e}{\hbar}\mathbf{A}_{\rm s}\right), \tag{8}$$

with $v_{\rm F} = 3at/2\hbar$ (Fermi velocity) and $\mathbf{q} = -i\nabla$ (momentum operator in two spatial dimensions). The components of the pseudospin vector $\mathbf{S}_\tau^\varphi = (\tau S_x^\varphi, S_y^\varphi)$ in the three-dimensional spin space,

$$S_x^\varphi = \begin{pmatrix} 0 & \cos\varphi & 0 \\ \cos\varphi & 0 & \sin\varphi \\ 0 & \sin\varphi & 0 \end{pmatrix}, \tag{9}$$

$$S_y^\varphi = \begin{pmatrix} 0 & -i\cos\varphi & 0 \\ i\cos\varphi & 0 & -i\sin\varphi \\ 0 & i\sin\varphi & 0 \end{pmatrix}, \tag{10}$$

represent the sublattice degrees of freedom. Note that the strain-induced vector potential

$$\mathbf{A}_{\rm s} = -\tau\frac{\hbar\beta}{2a}\begin{pmatrix} \epsilon_{xx} - \epsilon_{yy} \\ -2\epsilon_{xy} \end{pmatrix} \tag{11}$$

depends not only on the two-dimensional strain tensor, but also on the valley index τ in an explicit way. Effectively, it acts as an artificial gauge field that gives rise to a PMF,

$$B_{\rm s} = (\nabla \times \mathbf{A}_{\rm s})_z = \partial_x A_y - \partial_y A_x, \tag{12}$$

perpendicular to the α-$\mathcal{T}_3$ lattice plane.

In the presence of a magnetic field, the valley dependence of the (pseudo-) Landau levels (LLs) is of special interest, particularly with regard to valley-filtering effects when changing the α-$\mathcal{T}_3$ lattice scaling parameter α or the direction of the PMF $\gamma = \pm 1$. For this purpose we analyze initially the influence of a constant perpendicular PMF obtained from $\mathbf{A}_{\rm s} = -\tau\gamma B_{\rm s}y\mathbf{e}_x$ ($B_{\rm s} > 0$). Such a PMF can be created by triaxial strain of the lattice [30]. Introducing ladder operators $\hat{l}_\gamma^{(\dagger)}$ with $[\hat{l}_\gamma, \hat{l}_\gamma^\dagger] = 1$, we find for $\gamma = +1$,

$$\hat{l}_+^{(\dagger)} = \sqrt{\frac{\hbar}{2eB_{\rm s}}}(q_x \pm i\tau q_y + \tau eB_{\rm s}y/\hbar). \tag{13}$$

For $\gamma = -1$, $\hat{l}_+$ corresponds to $\hat{l}_-^\dagger$. Accordingly, Eq. (8) becomes

$$H_{\tau,+}^\varphi = \tau\hbar\omega_c\begin{pmatrix} 0 & \cos\varphi\,\hat{l}_+ & 0 \\ \cos\varphi\,\hat{l}_+^\dagger & 0 & \sin\varphi\,\hat{l}_+ \\ 0 & \sin\varphi\,\hat{l}_+^\dagger & 0 \end{pmatrix} \tag{14}$$

with $\omega_c = \hbar v_{\rm F}\sqrt{2eB_{\rm s}/\hbar}$, which, together with the corresponding expression for $\gamma = -1$, yields the LL spectrum

$$E_{\tau,\gamma} = \pm\hbar\omega_c\sqrt{n + \tfrac{1}{2}[1 + \gamma\cos(2\varphi)]}. \tag{15}$$

If we compare this result with the LL spectrum induced by a real magnetic field in the α-$\mathcal{T}_3$ lattice [see, e.g., Eq. (4) in Ref. [18]], we find that $-\tau$ corresponds to γ in Eq. (15). This means that the pseudo-LLs are degenerate in valley space. Of course, there exists an additional zero-energy flat band for $0 < \alpha \leqslant 1$.

Finally, we note that the higher-order contributions (due to larger strain) should give similar corrections as in the case of graphene because $f_{\mathbf{k}}$ is the same; for a recent review on strain in graphene, see Ref. [31].

III. NUMERICAL MODEL AND RESULTS

In the following calculations we will use "graphene-like" model parameters $a = 0.142$ nm, $t = 2.8$ eV, and $\beta = 3$ [10], where t sets the energy scale. Furthermore, we consider the four-terminal configuration depicted in Fig. 1(b) to study the transport properties of an α-$\mathcal{T}_3$ quantum dot imprinted by straining the lattice with an out-of-plane Gaussian bump:

$$h(\rho) = H\exp\left(-\rho^2/\sigma^2\right). \tag{16}$$

Here, ρ gives the in-plane radial distance from the quantum dot's center. H and σ denote the magnitude and the characteristic width of the deformation, respectively.

The resulting PMF follows from Eq. (12) together with Eqs. (11) and (6):

$$B_{\rm s} = \tau\frac{4\hbar\beta}{ae}\frac{H^2}{\sigma^3}\left(\frac{\rho}{\sigma}\right)^3 e^{-2(\rho/\sigma)^2}\sin 3\phi \tag{17}$$

(ϕ denotes the polar angle). $B_{\rm s}$ is visualized in Fig. 1(c) in the vicinity of the Dirac point $\mathbf{K}$. The PMF near $\mathbf{K}'$ is simply obtained by reversing the signs. As a result, electrons injected from $\mathbf{K}$ and $\mathbf{K}'$ valleys feel PMFs of opposite sign and thus will move in opposite directions. This observation gave rise to the proposal of strain-based valley filtering in graphene [13,17].

To determine the conductance G between the left (L) and right (R) leads in the limit of vanishing bias voltage, we use the Landauer-Büttiker formula [27],

$$G = G_0\sum_{m\in {\rm L}, n\in {\rm R}}|S_{n,m}|^2, \tag{18}$$

where the scattering matrix between all open (i.e., active) lead channels $S_{n,m}$ can be easily calculated with the help of the PYTHON-based toolbox KWANT [29]. In Eq. (18), G_0 is the maximum conductance per channel. We should also mention the use of zigzag boundaries for the injector (L) and collector (R) leads. In this case the valleys are well separated in momentum space [1]. The perpendicular leads, which had been added to reduce the leakage of non-valley-polarized currents into the collector [17], will have armchair boundaries. This allows us to single out a valley conductance, $G^{[\mathbf{K}^{(\prime)}]} = G_0\sum_{m\in {\rm L}, n\in {\rm R}}|S_{n,m}^{[\mathbf{K}^{(\prime)}]}|^2$, which is related to the probability that an injected electron will be transferred in any mode belonging to the $\mathbf{K}$ ($\mathbf{K}'$) valley of the collector. Then, with $G = G^{[\mathbf{K}]} + G^{[\mathbf{K}']}$, the $\mathbf{K}^{(\prime)}$ valley polarization of the output current can be defined as

$$\tau^{[\mathbf{K}^{(\prime)}]} = G^{[\mathbf{K}^{(\prime)}]}G^{-1}. \tag{19}$$

For validation of our numerical scheme we first reexamined the graphene lattice case ($\alpha = 0$) in Fig. 2, and confirmed the previously found qualitative behavior [17] also for larger values of the Fermi energy. The Fermi energy $E_{\rm F} = 0.219$ eV has been chosen such that it exceeds the barrier produced by the Gaussian bump for a wide range of strain parameters H and σ. Raising $E_{\rm F}$ will increase the cyclotron radius and thereby reduce the valley polarization by effectively shrinking the width of the bump. A maximum valley filtering $\tau^{[\mathbf{K}]}$ is observed in regime III for $\sigma > 15$ nm and $1.1 \lesssim \sigma/H \lesssim 3.9$ at $W = 50$ nm. In regime II we have quantum dots with large
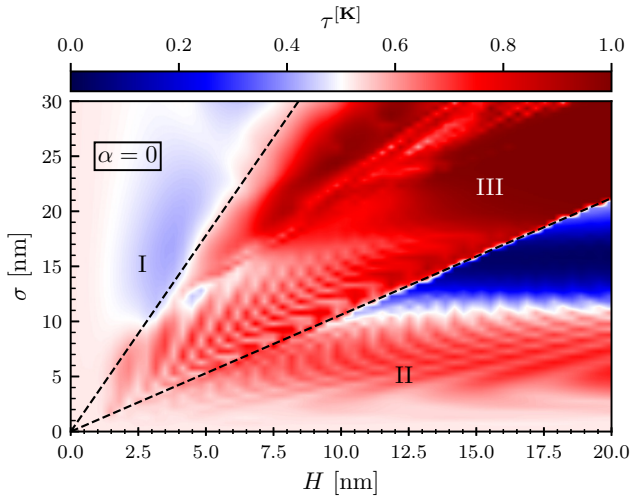
FIG. 2. Valley polarization by a strain-induced graphene-based quantum dot. The contour plot shows $\tau^{[\mathbf{K}]}$, depending on H and σ, for the four-terminal configuration in Fig. 1(b). The Fermi energy of the injected particles is $E_\mathrm{F} \simeq 0.22$ eV.

H and rather small σ which generate very high PMFs and therefore tend to repel the electron. This notably weakens the filtering effect. In the blue "subregime" for $\sigma > 10$ nm, the collector appears to be completely blocked for electrons from the **K** valley [17]. The boundary between regimes II and III is almost perfectly linear. The boundary between regimes III and I is more diffuse. The low PMFs in regime I (due to the small H and large σ) are clearly inefficient with regard to valley filtering.

Figure 3 demonstrates that the valley-polarization effect is also observed for α-$\mathcal{T}_3$-lattice-based configurations. In the top panel, we have chosen $\alpha = 1/\sqrt{3}$ in view of Refs. [18,24], whereas $\alpha = 1$ in the bottom panel refers to the dice lattice. Differences compared to the graphene-based system appear, primarily, for small H and σ. In particular, we find no weak valley-filtering effects in regimes I and II, which in the case of zigzag graphene nanoribbons result from the zero-energy edge state at the **K** point, whereas for α-$\mathcal{T}_3$ and dice zigzag nanoribbons the number of zero-energy states at **K** is even due to the additional flat-band state.

Comparing the valley polarization in the $\alpha = 1/\sqrt{3}$ and $\alpha = 1$ lattices, the boundary between regime II and III is smeared out in the former case for small to medium H. In the dice lattice the most interesting region III now is more clearly separated from the others, which might be advantageous in terms of possible applications. Note that the ripple structures found in the valley polarization will weaken with increasing size of our configuration (cf. Ref. [17]).

Figures 4(a) and 4(b) give the conductance G and valley polarization $\tau^{[\mathbf{K}]}$, respectively, as functions of the Fermi energy E_F for a strain-induced α-$\mathcal{T}_3$ quantum dot. Additional information is provided by the spatial distribution of the local density of states (LDOS),

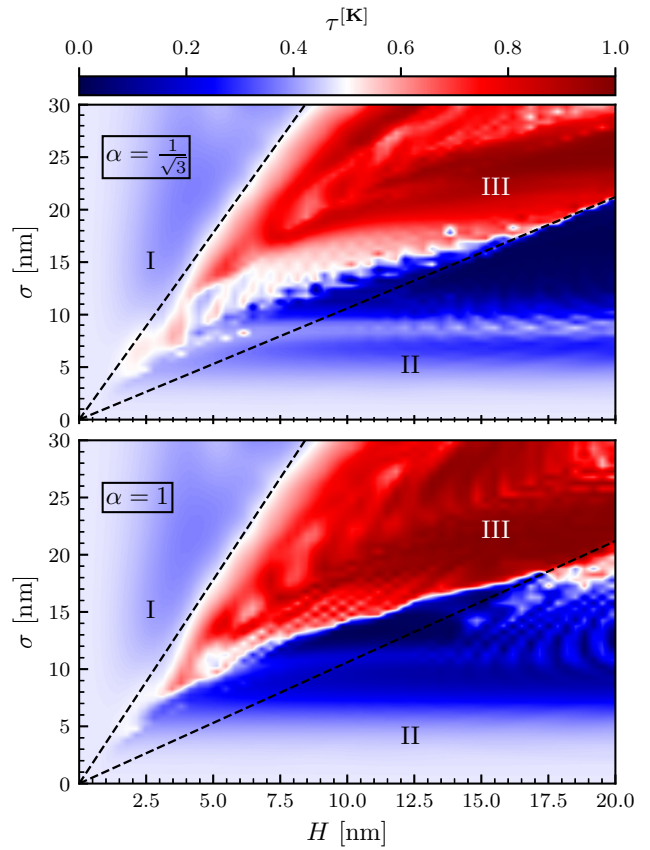$$\mathrm{LDOS}(E)_i = \sum_l |\langle i|l \rangle|^2 \delta(E - E_l), \qquad (20)$$

FIG. 3. Valley polarization by a strain-induced α-$\mathcal{T}_3$ quantum dot. The contour plots give $\tau^{[\mathbf{K}]}$ as a function of H and σ for the four-terminal configurations with $\alpha = 1/\sqrt{3}$ (top) and $\alpha = 1$ (bottom), where $E_\mathrm{F} \simeq 0.22$ eV. We included the linear regime boundaries of Fig. 2 for comparison.

and the local current density,

$$J_{ij}^{(m)} = \frac{i}{\hbar} \left[\langle j | \left(H_{ij}^\alpha \right)^\dagger | i \rangle^{(m)} - \langle i | H_{ij}^\alpha | j \rangle^{(m)} \right], \qquad (21)$$

where $|i\rangle$ and $|j\rangle$ are the single-particle wave functions projected on the respective sites. Equation (21) holds for the mth mode injected by the lead at energy E_F; the total (incident) current density is $J_{ij} = \sum_m J_{ij}^{(m)}$. Utilizing again KWANT [29] and the kernel polynomial method [28], these quantities can be computed very efficiently. The LDOS and J are shown in Figs. 4(c)–4(f) and 4(g)–4(j), respectively, for the resonances (1), (2), (1′), and (2′) marked in Figs. 4(a) and 4(b).

We begin the discussion of how the strained α-$\mathcal{T}_3$ quantum dot affects the transport properties of the configuration by examining the conductance (upper panels of Fig. 4, left ordinate) and the valley polarization (right ordinate). Of course, a notable current will only flow through the device if the Fermi energy E_F exceeds the barrier produced by the strained quantum dot. Otherwise the bump, having a high PMF inside, will basically block the flow of electrons towards the collector. We note that our finite quantum system can have a finite, albeit extremely low, transmission probability for (**K**- or **K**′-valley-polarized) electrons with smaller E_F. That notwithstanding, a high valley polarization may occur in this
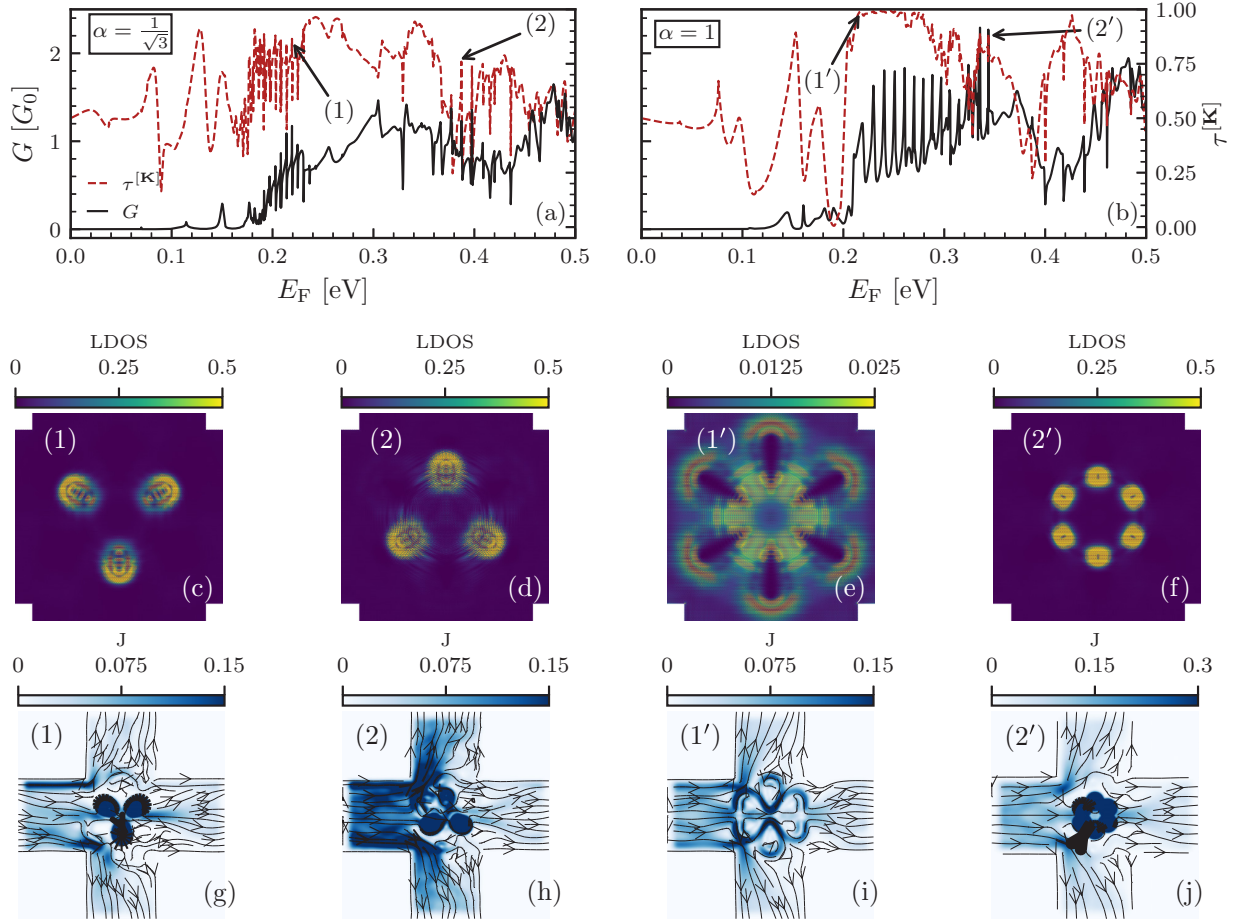
FIG. 4. (a), (b) Conductance G/G_0 and valley polarization $\tau^{[\mathbf{K}]}$ as a function of E_F for a strain-induced α-$\mathcal{T}_3$ quantum dot with $H = 17.9$ nm and $\sigma = 20$ nm. For the marked resonances (1) at $E_F = 0.219$ eV and (2) at $E_F = 0.387$ eV (lattice with $\alpha = 1/\sqrt{3}$) we have $\tau^{[\mathbf{K}]} = 0.86$ and $\tau^{[\mathbf{K}]} = 0.76$, respectively. For resonances (1′) at $E_F = 0.219$ eV and (2′) at $E_F = 0.344$ eV (dice lattice, $\alpha = 1$) we find $\tau^{[\mathbf{K}]} = 0.98$ and $\tau^{[\mathbf{K}]} = 0.86$, respectively. (c)–(f) Zoomed-in LDOS at resonances $(1^{(\prime)})$ and $(2^{(\prime)})$. (g)–(j) Corresponding intensity-coded current densities $|J_{ij}|$ (here, the lines and arrows are a guide to the eye.)

regime just as in the graphene case, where $\tau^{[\mathbf{K}]}$ reaches unity for small energies because of valley-polarized zigzag edge states.

For $\alpha = 1/\sqrt{3}$ above the threshold ($\simeq 0.2$ eV), two regions (bands) in the vicinity of resonance (1) and (2) with a high transmission probability are observed (in the displayed energy interval 0.2–0.5 eV). Here, the conductance shows an oscillating behavior that can be attributed to LL quantization (cf. the discussion of Fig. 5 below). In the dice-lattice case, the conductance features only a single band of resonances between (1′) and (2′) with particularly high valley polarization and can be similarly attributed to LL quantization. Increasing (decreasing) the PMF by varying H or σ will shift this region to higher (lower) Fermi energies as the LL are proportional to $\sqrt{B_s}$ [see Eq. (15)].

To further characterize the different transport channels we now examine the spatial variation of the LDOS in the quantum dot region. For a graphene-based ($\alpha = 0$) quantum dot configuration, the LDOS will show a "flower"-like pattern with sixfold symmetry, where consecutive "petals" belong to the A or B sublattice [10,16].

In the α-$\mathcal{T}_3$ lattice with $\alpha = 1/\sqrt{3}$ the inversion symmetry is broken in two ways: Besides the local inversion symmetry breaking by the strain, α itself breaks the inversion symmetry between sublattices A and C on a global scale. As a result, the "petals" of graphene's "flower"-like LDOS pattern will have alternating large and small amplitudes [see Figs. 4(c) and 4(d)]. The resulting ∇- and $\triangle$-shaped LDOS patterns with highly occupied sites belong to A-B and B-C sublattices and correspond to the typical resonances (1) and (2) in regions with high conductance, respectively. Moreover, the ∇ ($\triangle$) LDOS pattern is related to a negative (positive) sign of the PMF. It is worth noting, however, that both configurations, albeit separated by a large energy gap, possess an almost equally high valley polarization.

In the $\alpha = 1$ dice lattice, we rediscover the sixfold symmetry of the LDOS pattern in view of the threefold symmetries of the positive, respectively negative, strain-induced PMFs [cf. Fig. 1(c)]. This is illustrated by Figs. 4(e) and 4(f) for the resonances (1′) and (2′), respectively, but holds for the whole series of conductance peaks of Fig. 4(b). Clearly the spatial size and magnitude of the LDOS "petals" depend on the value
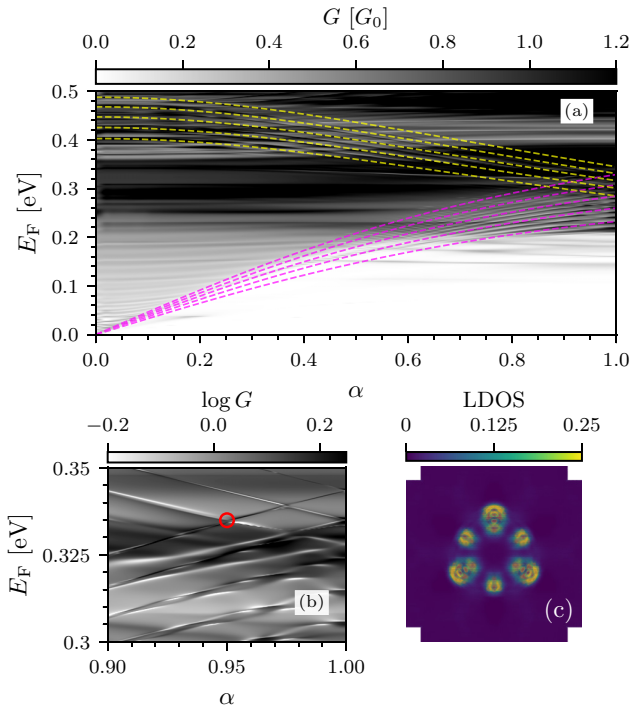
FIG. 5. Transport properties of a strained α-$\mathcal{T}_3$ quantum dot with $A = 17.9$ nm, $\sigma = 20$ nm. (a) Contour plot of the conductance G in the α-E_F plane. Dashed lines mark the lowest pseudo-LLs, according to Eq. (15) with $n = 0$, for five equidistant B_s fields ranging from 100 to 200 T and $\gamma = 1$ (yellow), -1 (magenta). (b) Zoom-in of the contour plot. (c) LDOS at $E = 0.335$ eV and $\alpha = 0.95$ [marked in (b) by the red circle].

of Fermi energy. In this regard, Figs. 4(e) and 4(f) represent rather extreme situations.

Figures 4(g)–4(j) display the course of the local current density, where its magnitude is coded by the blue-intensity map and the arrows visualize the direction of the electron flow. First, it becomes apparent that the electron flow from L to R is significantly blocked by the bump and the additional (perpendicular) contacts collect the nonpolarized current very effectively. Moreover, parts of the electrons are "confined" in the quantum dot region in long-living resonant states, just as observed for circular graphene quantum dots [32–36]. This becomes particularly obvious if one looks at Fig. 4(i), where the current is encircling the PMF. Nevertheless, in all cases, substantial amounts of electrons are able to penetrate through the quantum dot (preferably along the zero-PMF lines) and finally reach the collector R. Recalling the valley polarization according to Figs. 4(a) and 4(b), we can conclude that this particle stream is made up of electrons belonging to the **K** valley. Apparently the current intensities in Figs. 4(g) and 4(h) nicely feature the ∇ and Δ α-$\mathcal{T}_3$-lattice LDOS patterns in Figs. 4(c) and 4(d), respectively, and what is more, the current is valley polarized although it seems that the electrons do not feel the full PMF of Fig. 1(c).

Figure 5(a) provides a contour plot of the conductance dependence on the scaling parameter α and the Fermi energy E_F. In order to assign the onset of the conductance and some of resonances we included the pseudo-LLs (15) for $n = 0$ and

$\gamma = \pm 1$ at different PMFs B_s in the range 100–200 T, where the magenta (yellow) curves belong to $\gamma = -1$ ($+1$). Then, at $\alpha = 1/\sqrt{3} \simeq 0.577$, the resonances (1) and (2) from Fig. 4(a) fall within the range of the LLs with $n = 0$, $\gamma = -1$ and $n = 0$, $\gamma = 1$, respectively, exhibiting the ∇ and Δ pattern. Bearing in mind that γ in the PMF takes the role of $-\tau$ for a real magnetic field, the change in the sublattice polarization of the LDOS is understandable. This means that exchanging the valleys accounts for the change in the sublattices $A \to C$.

In Fig. 5(b) the region close to the dice-lattice case is enlarged, where the crossing of the $\gamma = \pm 1$ resonances takes place in Fig. 5(a). Here, the LDOS exhibits overlapping ∇ and Δ patterns. This is exemplarily demonstrated in Fig. 5(c). Note that the LDOS shows a similar behavior at the other (pseudo-LL) "crossing points" in Figs. 5(a) and 5(b).

IV. SUMMARY

To conclude, we have demonstrated how nanoscale strain engineering of pseudomagnetic fields can be used to cause and control valley-polarized transport through an α-$\mathcal{T}_3$ quantum dot embedded in a four-terminal configuration with zigzag edges. The strain (pseudomagnetic field) locally breaks the inversion symmetry of the system. By utilizing the KWANT software package, we presented numerically exact results for quantities that characterize the electronic properties and functionality of the considered device. Specifically, we discussed the conductance, the valley-filter efficiency, and the spatial charge and current density distributions. We noticed that the conductance resonances with high valley polarization could be related to the (pseudo-) Landau levels of the continuum quantum dot model. Thereby the local current densities reveal that transmission of electrons with given, let us say, **K**-valley polarization is possible and takes place predominantly along the lines of vanishing pseudomagnetic field; at the same time, electrons coming from the **K**' valley will be blocked by the quantum dot, and vice versa. For the dice model, at the set of resonances appearing in the first "conductance band," the maxima in the local density of states show a sixfold symmetry in real space, just as for the graphene case. Any finite $\alpha < 1$, however, gives rise to a (global) sublattice asymmetry and therefore creates an energy gap between states belonging to a local density pattern with threefold ∇ respectively Δ symmetry. Compared to a graphene-based configuration, for the dice and α-$\mathcal{T}_3$ lattices, the specific (limited) region in the quantum dot's width-and-height parameter space where the maximum valley-filtering effect appears, is much more clearly separated from that with valley-unpolarized transport. This might be advantageous for potential applications. Furthermore, since $\alpha \neq 0, 1$ globally breaks the inversion symmetry of the lattice, the use of the proposed configuration as an A-C-sublattice filter is feasible. Finally, we note that our results are generic to a class of lattices, which means they are applicable to graphene-like materials but also transition metal dichalcogenides and related materials. This also applies to kagome crystals where elastic strain induces the same pseudomagnetic field near the Dirac points as in the α-$\mathcal{T}_3$ lattice [37]. Equally important, the discussed valley filter effects should stay intact even for weak interactions or spin-orbit coupling as they primarily induce an energy gap.

[1] A. Rycerz, J. Tworzydło, and C. W. J. Beenakker, Europhys. Lett. **79**, 57003 (2007).

[2] D. Xiao, W. Yao, and Q. Niu, Phys. Rev. Lett. **99**, 236809 (2007).

[3] J. R. Schaibley, H. Yu, G. Clark, P. Rivera, J. S. Ross, K. L. Seyler, W. Yao, and X. Xu, Nat. Rev. Mater. **1**, 16055 (2016).

[4] A. H. Castro Neto, F. Guinea, N. M. R. Peres, K. S. Novoselov, and A. K. Geim, Rev. Mod. Phys. **81**, 109 (2009).

[5] R. V. Gorbachev, A. S. Mayorov, A. K. Savchenko, D. W. Horsell, and F. Guinea, Nano Lett. **8**, 1995 (2008).

[6] P. Zhao and J. Guo, J. Appl. Phys **105**, 034503 (2009).

[7] C. Lee, X. Wei, W. Kysar, and J. Hone, Science **321**, 385 (2008).

[8] N. Levy, S. Burke, K. L. Meaker, N. Panlasigui, A. Zettl, F. Guinea, A. Neto, and M. Crommie, Science **329**, 544 (2010).

[9] M. R. Masir, D. Moldovan, and F. M. Peeters, Solid State Commun. **175-176**, 76 (2013).

[10] M. Schneider, D. Faria, S. Viola Kusminskiy, and N. Sandler, Phys. Rev. B **91**, 161407(R) (2015).

[11] L. S. Cavalcante, A. Chaves, D. R. da Costa, G. A. Farias, and F. M. Peeters, Phys. Rev. B **94**, 075432 (2016).

[12] R. Carrillo-Bastos, C. León, D. Faria, A. Latgé, E. Y. Andrei, and N. Sandler, Phys. Rev. B **94**, 125422 (2016).

[13] M. Settnes, S. R. Power, M. Brandbyge, and A.-P. Jauho, Phys. Rev. Lett. **117**, 276801 (2016).

[14] C.-C. Hsu, M. L. Teague, J.-Q. Wang, and N.-C. Yeh, Sci. Adv. **6**, eaat9488 (2020).

[15] N. N. Klimov, S. Jung, S. Zhu, T. Li, C. A. Wright, S. D. Solares, D. B. Newell, N. B. Zhitenev, and J. A. Stroscio, Science **336**, 1557 (2012).

[16] R. Carrillo-Bastos, D. Faria, A. Latgé, F. Mireles, and N. Sandler, Phys. Rev. B **90**, 041411(R) (2014).

[17] S. P. Milovanović and F. M. Peeters, Appl. Phys. Lett. **109**, 203108 (2016).

[18] A. Raoux, M. Morigi, J.-N. Fuchs, F. Piéchon, and G. Montambaux, Phys. Rev. Lett. **112**, 026402 (2014).

[19] R. Shen, L. B. Shao, B. Wang, and D. Y. Xing, Phys. Rev. B **81**, 041410 (2010).

[20] S. K. Firoz Islam and P. Dutta, Phys. Rev. B **96**, 045418 (2017).

[21] A. Filusch and H. Fehske, Eur. Phys. J. B **93**, 169 (2020).

[22] B. Sutherland, Phys. Rev. B **34**, 5208 (1986).

[23] F. Wang and Y. Ran, Phys. Rev. B **84**, 241103 (2011).

[24] D. Bercioux, D. F. Urban, H. Grabert, and W. Häusler, Phys. Rev. A **80**, 063603 (2009).

[25] H.-Y. Xu, L. Huang, D. Huang, and Y.-C. Lai, Phys. Rev. B **96**, 045412 (2017).

[26] F. Bouhadida, L. Mandhour, and S. Charfi-Kaddour, Phys. Rev. B **102**, 075443 (2020).

[27] P. S. Davids, Phys. Rev. B **52**, 4146 (1995).

[28] A. Weiße, G. Wellein, A. Alvermann, and H. Fehske, Rev. Mod. Phys. **78**, 275 (2006).

[29] C. W. Groth, M. Wimmer, A. R. Akhmerov, and X. Waintal, New J. Phys. **16**, 063065 (2014).

[30] M. Settnes, S. R. Power, and A.-P. Jauho, Phys. Rev. B **93**, 035456 (2016).

[31] G. G. Naumis, S. Barraza-Lopez, M. Oliva-Leyva, and H. Terrones, Rep. Prog. Phys. **80**, 096501 (2017).

[32] J. Cserti, A. Pályi, and C. Péterfalvi, Phys. Rev. Lett. **99**, 246801 (2007).

[33] R. L. Heinisch, F. X. Bronold, and H. Fehske, Phys. Rev. B **87**, 155409 (2013).

[34] A. Pieper, R. Heinisch, and H. Fehske, Europhys. Lett. **104**, 47010 (2013).

[35] M. M. Asmar and S. E. Ulloa, Phys. Rev. Lett. **112**, 136602 (2014).

[36] H. Fehske, G. Hager, and A. Pieper, Phys. Status Solidi B **252**, 1868 (2015).

[37] T. Liu, Phys. Rev. B **102**, 045151 (2020).

Tunable valley filtering in dynamically strained α-$\mathcal{T}_3$ lattices

Alexander Filusch[1] and Holger Fehske [1,2,*]

[1]*Institute of Physics, University Greifswald, 17487 Greifswald, Germany*
[2]*Erlangen National High Performance Computing Center, 91058 Erlangen, Germany*

Mechanical deformations in α-$\mathcal{T}_3$ lattices induce local pseudomagnetic fields of opposite directionality for different valleys. When this strain is equipped with a dynamical drive, it generates a complementary valley-asymmetric pseudoelectric field, which is expected to accelerate electrons. We propose that by combining these effects by a time-dependent nonuniform strain, tunable valley filtering devices can be engineered that extend beyond the static capabilities. We demonstrate this by implementing an oscillating Gaussian bump centered in a four-terminal Hall bar α-$\mathcal{T}_3$ setup and calculating the induced pseudoelectromagnetic fields analytically. Within a recursive Floquet Green-function scheme, we determine the time-averaged transmission and valley polarization, as well as the spatial distributions of the local density of states and current density. As a result of the periodic drive, we detect novel energy regimes with a highly valley-polarized transmission, depending on α. Analyzing the spatial profiles of the time-averaged local density of states and current density we can relate these regimes to the pseudoelectromagnetic fields in the setup. By means of the driving frequency, we can manipulate the valley-polarized states, which might be advantageous for future device applications.

I. INTRODUCTION

In addition to charge and spin, electrons possess a valley degree of freedom in exciting two-dimensional condensed matter materials such as graphene or transition metal dichalcogenides. For example, graphene has two inequivalent Dirac cones at the **K** and **K**′ valleys of the Brillouin zone [1]. These valleys can be used to carry and encode information for logical operations, opening the field of "valleytronics" [2–4]. The main challenge for valleytronic devices is the precise control of valley polarization. Several proposals for valley filters and spatially separated valley-resolved currents by, e.g., nanoconstrictions [2], inversion-symmetry breaking [5], or line defects [6,7] have been made.

Graphene's outstanding ability to withstand mechanical deformations of up to 25% due to the strong sp^2 bonds [8] and, most importantly, its extraordinary electromechanical coupling is particularly promising in this regard. Because geometrical deformations modify the electronic hopping amplitude between the atoms, effective gauge fields with corresponding pseudomagnetic fields (PMFs) of more than 300 T can be generated [9]. Remarkably, electrons residing in the **K** or **K**′ valley feel opposing strain-induced PMFs since time-reversal symmetry is conserved. In connection, inhomogeneous PMFs due to out-of-plane deformations have attracted much attention because valley filters and beam splitters can be engineered [10–15], for an overview see Ref. [16]. Experimentally, such deformations can be created and controlled by STM tips [17]. Since the observed effects depend heavily on the energy and the degree of the deformation, there have been

efforts to improve the valley-filtering efficiency by arranging multiple Gaussian bumps in superlattices [18,19]. Interestingly, time-dependent strains introduce additional pseudoelectric fields (PEFs) proportional to the effective gauge field. The PEFs give rise to valley-current generation and phonon damping [20,21] and charge pumping in mechanical resonators [22]. Recently, it has been demonstrated that graphene nanodrums are viable means for valleytronic devices [23]. Also, crossed pseudoelectromagnetic fields have been shown to produce a charge current via a pseudo-Hall effect [24,25]. Oscillating out-of-plane strains have already been realized in nanoelectromechanical systems, where a suspended graphene membrane or ribbon is driven by an ac gate voltage with typical resonance frequencies in the MHz to GHz range [26,27].

The somewhat more complicated α-$\mathcal{T}_3$ lattice is obtained by placing an additional atom at the center of each hexagon in the honeycomb lattice with strength α, thereby interpolating between graphene ($\alpha = 0$) and the dice lattice ($\alpha = 1$) [28–30]. Most notably, an additional, strictly flat band appears at zero energy going through the **K** and **K**′ points, while the conduction and valence bands remain unaltered. There are several proposals for experimental realizations. The dice lattice can be manufactured by growing trilayers of cubic lattices, e.g., $SrTiO_3/SrIrO_3/SrTiO_3$, in the (111) direction [31]. In two dimensions, $Hg_{1-x}Cd_xTe$ at a critical doping has been reported to map onto the α-$\mathcal{T}_3$ lattice with an intermediate $\alpha = 1/\sqrt{3}$ parameter [28,32]. There are also several suggestions for an optical α-$\mathcal{T}_3$ lattice that would allow a tuning of α by dephasing one pair of the three counter-propagating laser beams [28,32]. Under external electromagnetic fields, the flat band and α-dependent Berry phase have striking consequences on the Landau level quantization [28,33], the quantum Hall effect [34,35], Klein tunneling [36–39], and Weiss oscillations [40].

---
*fehske@physik.uni-greifswald.de

While the flat band has zero group velocity and therefore zero conductivity, it is predicted to play an important role for the transport by its nontrivial topology [31,46], the coupling to propagating bands [41–43], or interaction effects [44–47]. Furthermore, electrons dressed by external laser fields or shaking in the α-$\mathcal{T}_3$ model have attracted interest particularly in view of tuning the electronic properties [48–51] up to the point of inducing Floquet topological phase transitions [52]. Accordingly, several works have exploited the valley degree of freedom, e.g., via the geometric (valley) Hall effect [53], magnetic Fabry-Pérot interferometry [54], or crossed Andreev reflections [55].

Recently, elastic deformations in α-$\mathcal{T}_3$ structures have been shown to induce PMFs that efficiently valley filter incoming electrons by excitation to α-dependent (pseudo) Landau levels [56,57]. When the out-of-plane deformations also oscillate in time, complementary PEFs are induced that drive electrons of opposite valleys in different directions. So far, however, the electronic transport properties of graphene ($\alpha = 0$) nano-electromechanical systems have mostly been discussed in the adiabatic limit, i.e., the ultrafast electrons simply perceive a static deformation profile due to the slowly oscillating nanodrum [23].

In this paper, we therefore consider a time-periodically oscillating Gaussian bump on an α-$\mathcal{T}_3$ lattice within the Floquet theory and show how the PEF improves the valley-filter capabilities and affects the flat band. For this, we study the transmission of electrons in a four-terminal Hall bar setup with zigzag terminations. The advantage of such driving is the possible tuning of α-dependent valley-polarized states by the driving frequency and the creation of (locally) flat bands for $\alpha > 0$. The paper is structured as follows. In Sec. II, we introduce the tight-binding model with time-periodic Gaussian deformations and derive the Fourier decomposition of the time-dependent transfer amplitudes analytically. We also provide results for the DC transmission, the time-averaged local density of states and the current density in four-terminal devices under a periodic drive in the nonequilibrium Green-function formalism. In Sec. III, we analyze a typical four-terminal transport setup and calculate all relevant quantities through a recursive Floquet Green-function algorithm built on top of the KWANT toolbox [58]. We conclude in Sec. IV.

II. MODEL AND METHODS

To describe the electronic properties of the time-periodically strained α-$\mathcal{T}_3$ lattice, we consider the following tight-binding Hamiltonian ($\hbar = 1$)

$$H_\alpha(t) = -\sum_{\langle ij \rangle} J_{ij}(t) a_i^\dagger b_j - \alpha \sum_{\langle ij \rangle} J_{ij}(t) c_i^\dagger b_j + \text{H.c.,} \quad (1)$$

where $a^{(\dagger)}$, $b^{(\dagger)}$ and $c^{(\dagger)}$ create (annihilate) an electron on Wannier sites A, B, and C, respectively. In the α-$\mathcal{T}_3$ lattice, an additional site C is placed at the center of each hexagon formed by the A and B sites. This site couples to the B sites via $\alpha J_{ij}(t)$, which allows for an interpolation between graphene ($\alpha = 0$) and the dice lattice ($\alpha = 1$). In the unstrained lattice, the nearest-neighbor hopping is $J_{ij} = J$ and the α-$\mathcal{T}_3$ lattice
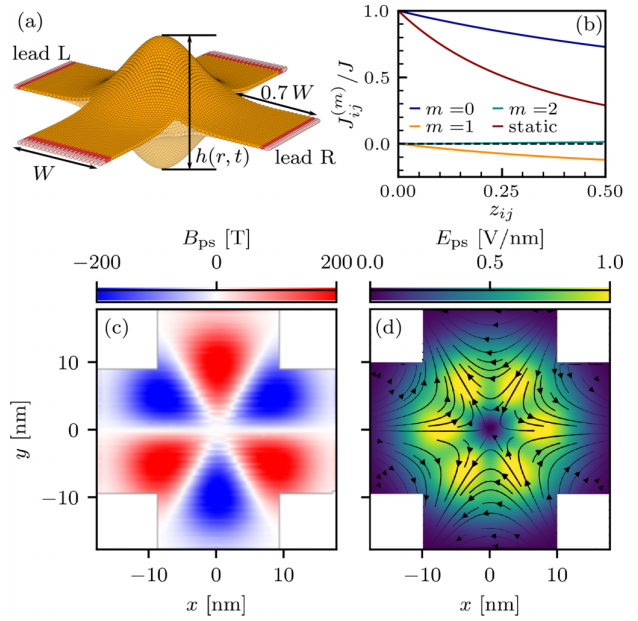

FIG. 1. (a) Four-terminal setup with a dynamic Gaussian deformation (3) in the center oscillating with frequency Ω. The parameters are $h_0 = 8$ nm, $\sigma = 10$ nm, and $W = 20$ nm. Semi-infinite leads (red) attached to the Hall bar region are modeled by the pristine tight-binding Hamiltonian, i.e., $J_{ij} = J$. For the coupling between the Hall bar and the leads, we take $J_{ij} = J$ also. To create the system numerically, we use the KWANT library [58]. (b) Comparison of the Fourier components of the time-dependent transfer amplitudes for representative values of z_{ij}, and $m = 0$, 1, 2. The static $J_{ij}(t = 0)/J$ case is also showcased. The horizontal line denotes $J = 0$. [(c) and (d)] (Zoomed-in) Pseudomagnetic and pseudoelectric field at, respectively, $t = 0$ and $t = T/8$ due to the time-periodic oscillating Gaussian bump from (a) with $\Omega = 0.25J$ for electrons in the **K** valley.

features a graphene-like band structure with an additional dispersionless band at zero energy [28].

The out-of-plane lattice distortion $h(\mathbf{r}, t)$ alters the site positions $\mathbf{r}_i'(t) = \mathbf{r}_i + h(\mathbf{r}_i, t)\mathbf{e}_z$ [cf. Fig. 1(a)], thereby varying the bond length $d_{ij}(t) = |\mathbf{r}_i'(t) - \mathbf{r}_j'(t)|$ between nearest neighbors. The modified transfer amplitude is given by

$$J_{ij}(t) = J \exp\{-\beta(d_{ij}(t)/a - 1)\}, \quad (2)$$

where $\beta = -\partial \ln J / \partial \ln a$ is the Grüneisen parameter with a denoting the (unstrained) nearest-neighbor distance.

In this work, we look upon a temporal oscillating Gaussian bump

$$h(r, t) = h_0 \cos(\Omega t) \exp(-r^2/\sigma^2), \quad (3)$$

where r is the radial distance from the center, and h_0 and σ denote the bump's height and width, respectively. The Gaussian deformation is assumed to be periodic in time, $h(r, t + T) = h(r, t)$, where T is the oscillation period and $\Omega = 2\pi/T$ the corresponding frequency. Note that since $h(r, t)^2$ enters Eq. (2), $J_{ij}(t)$ [and thereby $H^{(\alpha)}(t)$] has a periodicity of $T/2$ (frequency of 2Ω) instead.

We expand Eq. (1) in a Fourier series, $H_\alpha(t) = \sum_m e^{i2m\Omega t} H_\alpha^{(m)}$, with the Fourier coefficients given by

$H_\alpha^{(m)} = \frac{2}{T} \int_0^{T/2} e^{i2m\Omega t} H_\alpha(t) \, dt$. Rewriting Eq. (2) as $J_{ij}(t)/J = \exp g(z_{ij}, t)$, where $g(z_{ij}, t) = -\beta(\sqrt{1 + z_{ij} \cos^2 \Omega t} - 1)$, we can expand Eq. (2) with respect to the (squared) height differences between nearest neighbors,

$$z_{ij} = \frac{h_0^2}{a^2} \left(e^{-r_i^2/\sigma^2} - e^{-r_j^2/\sigma^2}\right)^2, \qquad (4)$$

in a Taylor series around the pristine case $z_{ij} = 0$. Then, using Faà di Bruno's formula, we obtain

$$J_{ij}(t)/J = \sum_{n=0}^{\infty} \sum_{k=0}^{n} B_{n,k}(t) \frac{z_{ij}^n}{n!}, \qquad (5)$$

where

$$B_{n,k}(t) = \beta^k \frac{(-1)^n}{2^n} \cos^{2n}(\Omega t)[2(n-k)-1]!! \binom{2n-k-1}{2(n-k)} \qquad (6)$$

denotes the partial Bell polynomials of the second kind for the nth derivative of $\exp g(z_{ij}, t)$ at $z_{ij} = 0$ [59]. Due to

$$\cos^{2n}(\Omega t) = \frac{1}{2^{2n}} \left\{ \sum_{l=0}^{n-1} 2 \binom{2n}{l} \cos[2(n-l)\Omega t] + \binom{2n}{n} \right\}, \qquad (7)$$

[60], the Fourier coefficients of the time-dependent Hamiltonian

$$H_\alpha^{(m)} = -\sum_{\langle ij \rangle} J_{ij}^{(m)} a_i^\dagger b_j - \alpha \sum_{\langle ij \rangle} J_{ij}^{(m)} c_i^\dagger b_j + \text{H.c.} \qquad (8)$$

become

$$J_{ij}^{(m)}/J = \sum_{n=|m|}^{\infty} \sum_{k=0}^{n} B_{n,k}(0) \binom{2n}{n-|m|} \frac{1}{2^{2n}} \frac{z_{ij}^n}{n!}. \qquad (9)$$

Note that the series in Eq. (5) has a convergence radius of 1, which corresponds to a strained bond length $d_{ij} = \sqrt{2}a$. Since graphene is known to sustain up to 25% [8] of elastic strain ($z_{ij} = 0.5625$), any physical deformation can be correctly described. The dependence of the different Fourier components on the driving amplitude h_0 is depicted in Fig. 1(b), where we show Eq. (9) for $m = 0$, 1 and 2 as a function of the expansion parameter $z_{ij} \propto h_0^2$. We also plot the static hopping parameter ($t = 0$) from Eq. (2). Due to time-averaging, $J_{ij}^{(0)}/J$ is increased compared to the static Gaussian bump. Clearly, z_{ij} (h_0) directly controls the magnitude of $J_{ij}^{(m)}$. If z_{ij} is constant, $J_{ij}^{(m)}$ decreases exponentially with m.

Dynamic elastic strain results in a time-dependent pseudoelectromagnetic vector potential $\mathbf{A}_{\text{ps}} = (\text{Re}A_{\text{ps}}, \text{Im}A_{\text{ps}})$ [1,61,62], where

$$A_{\text{ps}}(\mathbf{r_i}, t) = \frac{1}{ev_F} \sum_{j=1}^{3} J_{ij}(t) e^{-i\mathbf{K} \cdot \delta_{ij}'} \qquad (10)$$

and the sum is taken over the nearest neighbors. $\mathbf{K}$ denotes the corner of the Brillouin zone and $\delta_{ij}' = \mathbf{r_i'} - \mathbf{r_j'}$ is the strained nearest-neighbor vector. The PMF is then $\mathbf{B}_{\text{ps}} = \nabla \times \mathbf{A}_{\text{ps}}$ and the PEF is $\mathbf{E}_{\text{ps}} = -\partial \mathbf{A}_{\text{ps}}/\partial t$. The PMF and PEF induced by oscillating Gaussian strain for electrons in the $\mathbf{K}$ valley is

depicted in Figs. 1(c) and 1(d). For electrons in the $\mathbf{K}'$ valley, the signs of the PMF and PEF are reversed. To study the transport properties of the temporal oscillating Gaussian bump with regard to its valley-filter capabilities, we use the four-terminal setup shown in Fig. 1(a). The DC transmission of electrons originating from the left lead (L) to the right lead (R) is given by [63,64]

$$T(E) = \sum_{k \in \mathbb{Z}} \text{Tr}\left[G_{k0}^r \Gamma_{00}^L G_{0k}^a \Gamma_{kk}^R\right], \qquad (11)$$

where $G_{k0}^{r(a)}$ denotes the retarded (advanced) Green function in Floquet basis. $\Gamma_{kk}^{L(R)} = i[\Sigma_{L(R)}^r - (\Sigma_{L(R)}^r)^\dagger]_{kk}$ is the level-width function of the left (right) lead in Floquet representation and $\Sigma_{L(R)}^r$ denotes the respective self-energy in Floquet representation, i.e., $(\Sigma_{L(R)}^r)_{km} = \delta_{km} \Sigma_{L(R)}^r(E + 2k\Omega)$. The trace (Tr) is taken over all sites in the Hall bar region.

The retarded Floquet Green function G_{mn}^r is defined by [65]

$$\sum_{m \in \mathbb{Z}} \left[(E + i\eta + 2k\Omega)\delta_{km} - H_\alpha^{(k-m)} - (\Sigma^r)_{km}\right] G_{mn}^r(E) = \delta_{kn}, \qquad (12)$$

where $(\Sigma^r)_{km}$ denotes the sum over the four lead self-energies in Floquet representation, and $i\eta$ is a small complex number guaranteeing convergence in the numerical matrix inversion. After truncating Eq. (12) at finite $m \in [-M, M]$, we apply the recursive Green-function algorithm for Floquet systems [66,67] and split the four-terminal setup by a circular slicing scheme [68]. Thereby, systems with up to 150 000 lattice sites with $M = 6$ are accessible, which is not feasible by direct matrix inversion.

In order to study the valley-filtering, we choose zigzag boundaries for the left and right lead of the Hall bar to have well-separated valleys in momentum space and the self-energy can be projected, respectively, onto the $\mathbf{K}$ or $\mathbf{K}'$ points, i.e., $\Sigma_R^r = \Sigma_R^{r,[\mathbf{K}]} + \Sigma_R^{r,[\mathbf{K}']}$. Then,

$$T^{[\mathbf{K}]}(E) = \sum_{k \in \mathbb{Z}} \text{Tr}\left[G_{k0}^r \Gamma_{00}^L G_{0k}^a \Gamma_{kk}^{R,[\mathbf{K}]}\right] \qquad (13)$$

gives the transmission of electrons originating from the left lead into the $\mathbf{K}$ states of the right lead and we can define the valley polarization

$$\tau^{[\mathbf{K}]} = T^{[\mathbf{K}]}/T. \qquad (14)$$

For incidents along the armchair direction, i.e., from the top or bottom lead [cf. Fig. 1(a)], the Gaussian bump acts as a valley-beam splitter instead [12], which would necessitate a different lead configuration [23,69]. In addition, the spatial distribution of the time-averaged local density of states (LDOS) on site i in Floquet basis,

$$\text{T-LDOS}(E)_i = -\frac{1}{\pi} \text{Im}\left(G_{00}^r\right)_{i,i}(E), \qquad (15)$$

gives valuable insight into excited states inside the Gaussian bump, quite similar to the static case, where one has $\text{LDOS}_i(E) = -\frac{1}{\pi} \text{Im} \, G_{i,i}^r(E)$. The T-LDOS can be efficiently calculated by the kernel polynomial method [70,71]. Furthermore, the Keldysh equation connects the retarded

Floquet-Green function with the lesser Floquet-Green function in Floquet representation [72,73],

$$G_{mn}^<(E) = \sum_{kl} G_{mk}^r(E) \Sigma_{kl}^<(E) G_{ln}^a(E), \qquad (16)$$

where $\Sigma_{kl}^< = i \sum_p \Gamma_{kl}^p(E) f^p$ and $f^p = 1/1 + \exp\{(E - \mu_p)/k_b T\}$ denotes the Fermi-Dirac distribution of an individual lead p with chemical potential $\mu_p = E + eV_p/2$, and V_p is the applied bias voltage. Then, the time-averaged and energy-resolved current density between site i and site j is given by [66]

$$I_{ij}(E) = \sum_{k \in \mathbb{Z}} J_{ij}^{(k)} [G_{0k}^<]_{ij}(E). \qquad (17)$$

III. RESULTS

In our numerical calculations, we take the system parameters given in Fig. 1, as well as the (graphene-like) values $a = 0.142$ nm, $\beta = 3$, and $J = 2.8$ eV for the tight-binding model [11], unless otherwise specified. Let us first comment on the frequency dependency in the off-resonant case. Here, the time-reversal symmetry is intact and the time-averaged Hamiltonian $H_\alpha^{(0)}$ dominates the dynamics because the first-order corrections, $[H_\alpha^{(m)}, H_\alpha^{(-m)}]$, vanish in the Floquet-Magnus expansion [74]. Concomitantly, the coupling between the Floquet sidebands is weak [cf. Fig. 1(b)], necessitating frequencies smaller than the bandwidth to ensure a large overlap between neighboring sidebands. For the parameters used, we take $J_{ij}^{(m)}$ up to $m = 3$ since $z_{ij} \lesssim 0.5$ [cf. Fig. 1(b)] and $M = 5$ in the Floquet space to assure convergence of the truncation scheme.

Figures 2(a), 2(b), and 2(c) show the transmission T of electrons originating from the left lead moving to the right lead and their valley polarization $\tau^{[\mathbf{K}]}$ for graphene ($\alpha = 0$), the intermediate $1/\sqrt{3}$-$\mathcal{T}_3$ lattice, and the dice lattice ($\alpha = 1$), respectively. The main feature of the static bump is an almost complete valley polarization of the transmitted electrons stemming from the excitation to α-dependent strain-induced Landau levels leading to "flowerlike" LDOS patterns inside the deformed region [10,11,13,56]. One of the main caveats is the reduction in valley polarization of the output current with increasing energy since the main contribution comes from the lowest energy band [13].

For the graphene case [cf. Fig. 2(a)], we notice two characteristic transport regimes, for $E < \Omega$ and $E \simeq \Omega$. Starting with $E < \Omega$, we observe a plateau in the valley polarization up to $E \simeq 0.3$ eV with finite transmission because, in this energy range, only the valley-polarized zigzag edge band is occupied [18]. At higher energies up to $E = \Omega$, the valley polarization decreases since higher bands are populated [13]. Moreover the transmission is suppressed near $E \lesssim \Omega$, indicating a gap at edge of the first Floquet zone. We found this Floquet gap irrespective of the applied frequency (below the bandwidth). Exactly at $E = \Omega$, we see an abrupt onset in the transmission with almost perfect valley polarization [$\tau^{[\mathbf{K}]} \simeq 0.9$] at the $m = 0$ and $m = 1$ zone boundary. This is quite contrary to the static case, where an increase in the energy will lower the valley polarization.
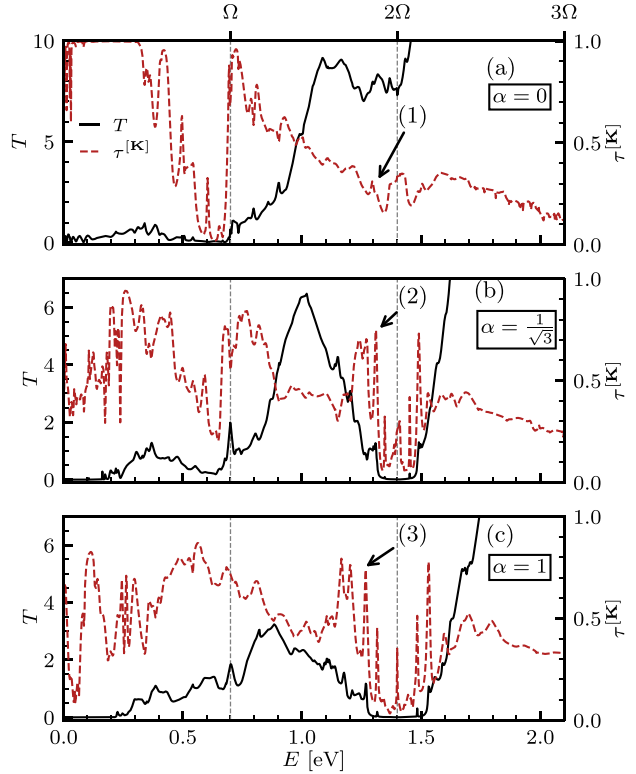

FIG. 2. [(a)–(c)] Transmission and valley polarization in dependence of (quasi) energy for an oscillating Gaussian bump in a α-$\mathcal{T}_3$ lattice for $\alpha = 0$, $1/\sqrt{3}$ and 1, respectively. Vertical dashed lines denote $E = \Omega$ and $E = 2\Omega$. The resonances at energies $E \simeq 1.31$, $\simeq 1.31$, and $\simeq 1.27$ eV are marked by (1), (2), and (3), respectively, where we find $\tau^{[\mathbf{K}]} = 0.4$, 0.75, and 0.75.

In the intermediate case $\alpha = 1/\sqrt{3}$, an additional transport channel emerges around $E \simeq 2\Omega$ [cf Fig. 2(b)] related to the flat band, besides the valley plateau at $E = \Omega$ and the static-like regime $E < \Omega$. For energies below a threshold of 0.2 eV, the bump will block any current due to the large PMF inside. Above this threshold, the transmission features valley-polarized resonances with the characteristic six-fold symmetric (T-)LDOS pattern indicative of the static case. Near $E = \Omega$, we notice a similar Floquet gap with a valley-polarization plateau, albeit slightly reduced. Around $E \simeq 2\Omega$, we notice that the transmission vanishes (is greatly suppressed) exactly at (near) the $m = 1$ zone center at $E = 2\Omega$ ($E = 2\Omega \pm 0.1$ eV). Here, the flat band of the $m = 1$ Floquet sideband hybridizes with the central $m = 0$ band, and all states at this energy become localized [cf. discussion of Figs. 3(h) and 3(i) below]. Since flat bands—due to their zero group velocity—do not carry any current, the transport is completely blocked. Regrettably, the numerical accuracy at the flat band heavily influences the value of the calculated polarization. We also verified that no current is transmitted into top/bottom leads, confirming the complete blocking of any transport. The transmission gap of width $\Delta \simeq 0.18$ eV around $E = 2\Omega$ is symmetric in the energy, which is a result of the particle-hole symmetric sidebands. Away from this gap we observe
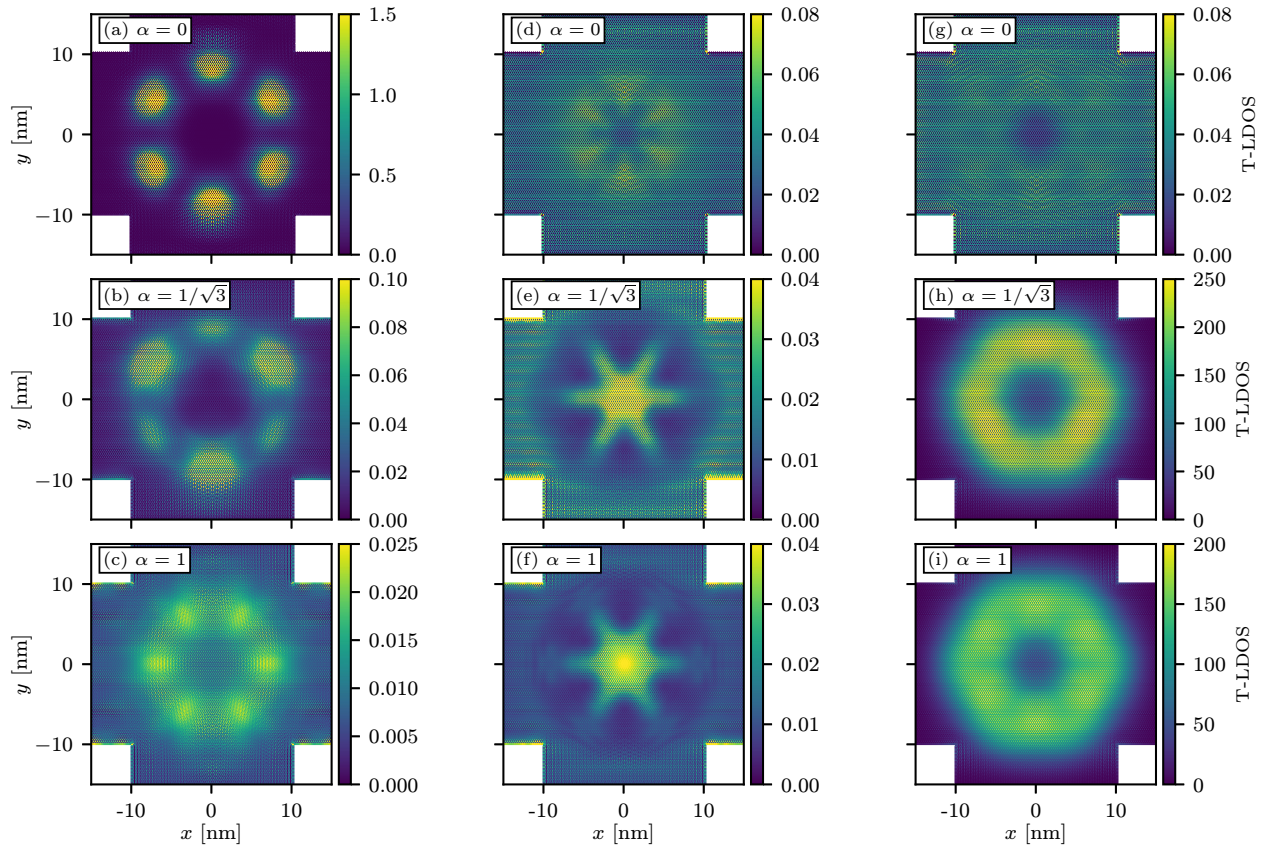
FIG. 3. (Zoomed-in) Time-averaged local density of states (T-LDOS) at energies $E = \Omega$ [(a)–(c)], resonances (1–3) in [(d)–(f)] and $E = 2\Omega$ [(g)–(i)] for graphene ($\alpha = 0$), the $1/\sqrt{3}$-$\mathcal{T}_3$ lattice and the dice lattice ($\alpha = 1$), respectively.

a small band of transmission resonances around $E \simeq 1.31$ eV [cf. (2) in Fig. 2(b)] with a particular high degree of valley polarization $\tau^{[\mathbf{K}]} \simeq 0.75$. We will see that this is due to the PEF, see discussion of Figs. 3(e), 3(f), and 4(b) below.

For the dice lattice [cf. Fig. 2(c)], we can again identify the two characteristic transport regimes, $E < \Omega$ and $E \simeq 2\Omega$, of the $\alpha = 1/\sqrt{3}$ model, which obviously interpolates between graphene and the dice-lattice physics. Accordingly, as necessary conditions for the different regimes, we find: When $\alpha < 1$, a valley-polarization plateau is induced around $E \simeq \Omega$,

while in the case of $\alpha > 0$, the model features flat-band states at $E = 2\Omega$ with highly valley-polarized states at the edges of the transmission gap.

To fix the signatures of these effects and contrast them with those of the static transport channels, in Fig. 3 we plot the time-averaged LDOS for $E = \Omega$, resonances (1)-(3) and $E = 2\Omega$ for $\alpha = 0$, $1/\sqrt{3}$ and 1, respectively.

At $E = \Omega$, the T-LDOS for $\alpha = 0$ ($\alpha = 1/\sqrt{3}$) features the sixfold (threefold) symmetric T-LDOS pattern confined to the lobes of the PMF displayed in Fig. 1(c),
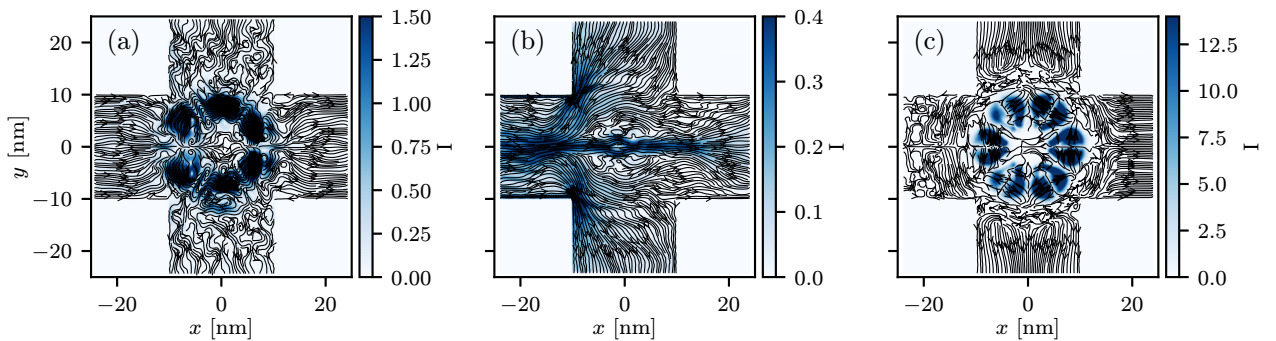

FIG. 4. (Zoomed-in) Time-averaged current density profile I at energies $E = \Omega$ (a), resonances (2) in (b) and $E = 2\Omega$ (c) for graphene ($\alpha = 0$), the $1/\sqrt{3}$-$\mathcal{T}_3$ lattice and the dice lattice ($\alpha = 1$), respectively.

while the T-LDOS almost vanishes in the dice lattice case [cf. Figs. 3(a)–3(c)].

For resonances (1)–(3) [cf. Figs. 3(d)–3(f)], we notice for $\alpha > 0$ that the incoming electrons are confined to the center instead of mirroring the profile of the PMF. We attribute this to the PEF displayed in Fig. 1(d), which drives the incoming electrons residing in the **K** valley to the low field region inside the bump, while electrons in **K**′ valley—feeling the opposite field—are pushed away, thereby effectively polarizing the transmitted electrons [see discussion on Fig. 4(b)]. This feature is characteristic for the series of resonances around (2) and (3) [and also Fig. 7 around (1)]. The time-averaged LDOS at $E = 2\Omega$ in Fig. 3(h), 3(i) shows a highly degenerate state restricted to the Gaussian bump [cf. the color-map scale], which is in contrast to the flat band state at $E = 0$, where the LDOS is spread over the whole lattice instead. In fact, the LDOS diverges at $E = 2\Omega$, which indicates a flat-band like state. In the numerics, we have added a small imaginary part to the energy ($\eta = 10^{-5}$) to guarantee convergence of the matrix inversion. This effect occurs at $E = 2m\Omega$, where $m = 0, \pm1, \pm2, \ldots$ The spectral weight increases with increasing h_0 and $1/m$. In the graphene case shown Fig. 3(g), the flat band is decoupled and the T-LDOS vanishes in accordance with the transmission calculations [cf. Fig. 2(a)].

Figures 4(a), 4(b), and 4(c) provide the local (time-averaged) current densities, indicating the dynamical effects, at $E = \Omega$, resonance (2) and $E = 2\Omega$, for $\alpha = 0$, $1/\sqrt{3}$, and 1, respectively, where a small bias is applied between the left and right lead. The magnitude is decoded by the blue intensity, and the arrows denote the direction of the electron flow. The static-like nature of the system at $E = \Omega$ becomes particularly apparent in Fig. 4(a), where the incoming stream of electrons is encircling the (distorted) lobes of the PMF, nicely representing the behavior of the T-LDOS [cf. Fig. 3(a)]. The situation for resonance (2) [cf. Fig. 4(b)] is much different, because, here, the PEF focuses a small part of the electron flow through the bump along the x axis before exiting the scattering region through lead R. The majority of the electron flow is blocked and leaves the scattering region via the top and bottom lead, see Fig. 4(b). Recalling the corresponding valley polarization in Fig. 2(b), we can conclude that the transmitted stream consists primarily of **K** electrons. The density profile at $E = 2\Omega$ displays a large amount of current trapped inside the bump [cf. Fig. 4(c)], thereby blocking any transmission through the setup. To assess the stability of the valley-polarized states near $E \simeq \Omega$ and $E \simeq 2\Omega$, in Fig. 2(b), we provide a contour plot of the valley polarization as a function of the energy E and the bump height h_0 in Fig. 5 around $E = 2\Omega$ (top) and $E = \Omega$ (bottom). We again choose $\alpha = 1/\sqrt{3}$ as this system best interpolates between graphene and the dice lattice. We omitted $h_0 < 5$ nm since the amplitude, which directly controls the interband coupling between the Floquet copies [cf. Fig. 1(b)], is too weak in this case. In both cases, the regions of high valley polarization are robust for a wide range of amplitudes h_0 and we can identify $h_0 \gtrsim 6$ as the optimal regime for polarization. While the polarized resonances around $E \simeq 2\Omega$ depend almost linearly on h_0, the valley polarization reaches nearly unity around $E \simeq \Omega$ for large $h_0 \simeq 9$ nm.

So far, in order to avoid problems with the rapidly increasing dimension of the Floquet space, we worked at a rather
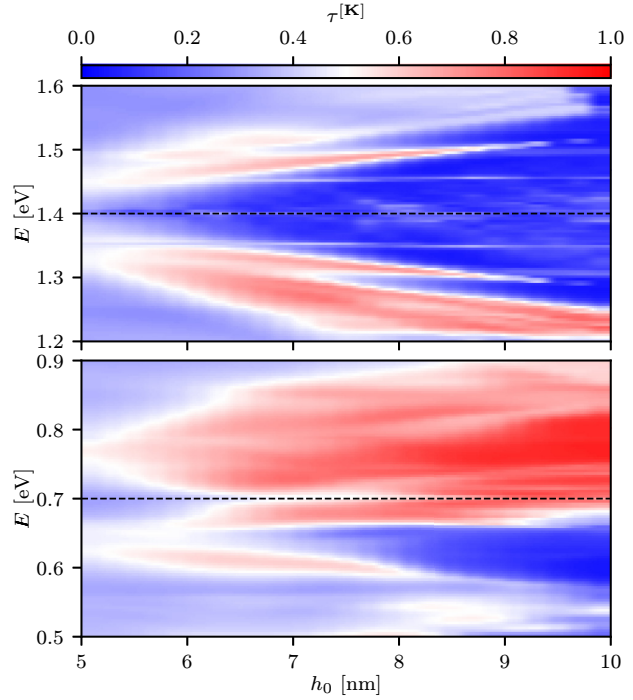

FIG. 5. Contour plot of the valley polarization for the $\alpha = 1/\sqrt{3}$ lattice as a function of E and h_0 for an oscillating Gaussian bump. Horizontal dashed lines mark $E = 2\Omega$ and $E = \Omega$, respectively.

large driving frequency. To demonstrate that the discussed valley-polarization effects persist for smaller frequencies, in Fig. 6, we show the valley polarization in the Ω-E plane for the $1/\sqrt{3}$ lattice. Obviously, the valley-polarized regimes induced by the dynamical strain for $E = \Omega$ and $E \simeq 2\Omega$ appear down to at least $\Omega = 0.1J$, albeit being slightly reduced. The static-like regime $E < \Omega$ deteriorates when $\Omega < 0.2J$ through

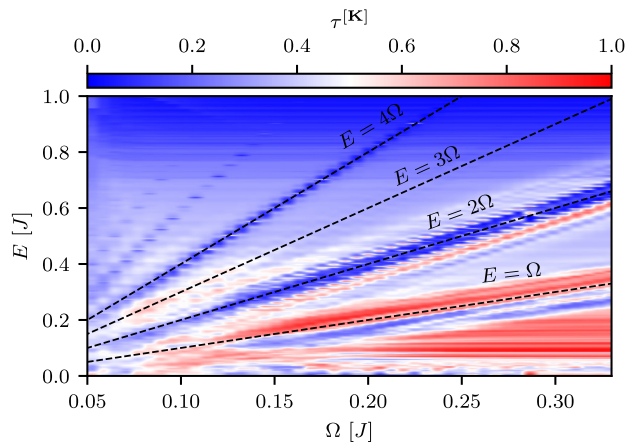

FIG. 6. Contour plot of the valley polarization in dependence on (quasi) energy and driving frequency for an oscillating Gaussian bump on the intermediate $1/\sqrt{3}$ lattice. The energy range is limited by the Van Hove singularity $E = J$ (=2.8 eV) since the valley degree of freedom can only be defined up to this point. Dashed lines mark $E = m\Omega$ for $m = 1, 2, 3,$ and 4, respectively.
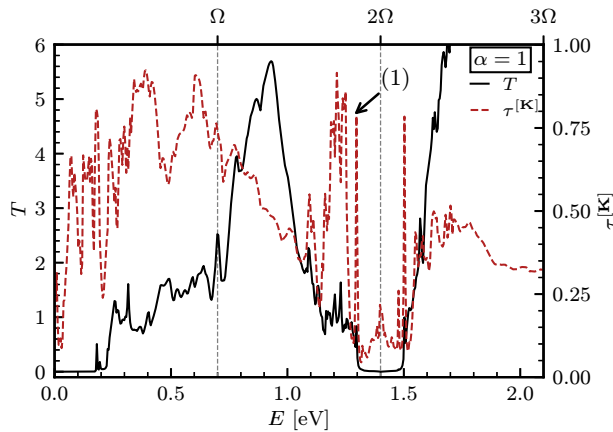
FIG. 7. Transmission and valley polarization in dependence on the (quasi) energy for an oscillating Gaussian bump on the dice lattice ($\alpha = 1$) with $h_0 = 12$ nm, $\sigma = 15$ nm, and frequency $\Omega = 0.25J$. Here, the Hall bar has $W = 30$ nm. Vertical dashed lines mark $E = \Omega$ and $E = 2\Omega$.

the overlap with $E = \Omega$ polarization regime. The gap Δ around $E = 2\Omega$ with the valley-polarized states [cf. Fig. 2(b), resonance (2)] persists until $\Delta = 2\Omega$, i.e., when the resonances will be located outside the first Floquet zone. Since the discussed frequency range 34–225 THz ($\Omega = 0.05J$–$0.33J$) could not be expected to be realized in graphene-based nano-electromechanical resonators [26,27], we rather envision an implementation of the α-$\mathcal{T}_3$ lattice in optical lattices, where dynamical strain also could be realized [75]. The main advantage of this route is, besides having direct access to the scaling paramter α, that the transfer amplitudes can be freely manipulated [76,77].

Finally, let us comment on the system-size dependence of our results. Figure 7 gives the transmission and valley polarization for a dice-lattice Hall bar with $W = 30$ nm, which corresponds to 1.5×10^5 sites and a 50% increase in the lead's width. We take $h_0/\sigma = 0.8$ and $\sigma/W = 0.5$ as in Fig. 1, i.e., $h_0 = 12$ nm and $\sigma = 15$ nm. The driving frequency remains $\Omega = 0.25J$. We find a pronounced band of resonances around (1) $E \simeq 1.3$ eV, where the valley polarization reaches almost unity. We note that the observed effects weaken when we analyze smaller systems (not shown). In any case, it is important that the use of larger system sizes enhances the valley polarization and the corresponding resonances near $E = 2\Omega$, which means that our results should be robust in the thermodynamic limit, i.e., for real-world devices. This is in accord with the arguments presented in Ref. [19], where the authors estimated the number of pseudo-Landau level subbands by counting the iso-field orbits that enclose an integer magnetic flux. By increasing W, the inhomogeneous PMF is spread over a larger region, thereby increasing the number of iso-orbits (and resonant states). Although the nature of driving-induced

valley-polarized states differs in our case, a similar mechanism is at work.

IV. SUMMARY

In this paper, we have shown how a time-periodic modulation of strain-induced Gaussian bumps allows for engineering the transport properties in α-$\mathcal{T}_3$ lattice Hall bars. To be more specific, we demonstrated the appearance of novel valley-polarized states and flat bands tunable by the driving frequency and the scaling parameter α. We discussed the role of the pseudoelectromagnetic fields in time-periodic Gaussian bumps in terms of analytical expressions for the time-dependent transfer amplitudes. Using the recursive Floquet Green-function algorithm with a circular slicing scheme, we obtained and examined the DC transmission, valley polarization, and the spatial distribution of the time-averaged local density of states and the current density profile in a four-terminal device. Depending on the scaling parameter α, we identified two transport regimes with distinct valley-polarization responses caused by the dynamic strain. For $\alpha < 1$, we detected a second plateau in the valley polarization at the boundary of the central and first Floquet sideband. In the time-averaged LDOS, we found a revival of the static "flowerlike" pattern mirroring the shape of the pseudomagnetic field due to the incoming electron flow with **K** polarization encircling the lobes of the external field. In the case of $\alpha > 0$, we noticed a vanishing transmission at about $2m\Omega$, which could be related to the flat bands of higher sidebands coupled to states in the zeroth sideband. The corresponding time-averaged LDOS pattern revealed a substantial spectral weight spread inside the bump, blocking any current through the device due to the zero group velocity of these flat-band states. In the vicinity of this transmission "gap," we found highly valley-polarized resonances where the incoming (**K**-polarized) electrons are focused along the zigzag orientation through the Gaussian bump by the pseudoelectric field. We confirmed that above a threshold amplitude of the out-of-plane oscillation, the device facilitates valley filtering of the incoming electrons in both regimes, $E \simeq \Omega$ and $E \simeq 2\Omega$, with different scaling behaviors. We enhanced the valley-filter efficiency and the resonance structure by considering larger system sizes. While previous works on nanodrums mainly examined the adiabatic limit, we here focused on a high-frequency regime and numerically studied the influence of the external field dynamics on transport. We found pronounced effects of the PEF, e.g., α-dependent Floquet gaps, novel valley-polarized states where the incoming electrons are focused, and flat-band states. Since Gaussian bumps in α-$\mathcal{T}_3$ lattices have promising valley-filtering capabilities in the adiabatic and anti-adiabatic limit, we believe that observed behavior is "generic", i.e., the used high frequencies are not a restraint. Moreover the proposed setup should be realizable in optical lattices, according to their tunability of hopping amplitudes.

[1] A. H. Castro Neto, F. Guinea, N. M. R. Peres, K. S. Novoselov, and A. K. Geim, Rev. Mod. Phys. **81**, 109 (2009).

[2] A. Rycerz, J. Tworzydło, and C. W. J. Beenakker, Europhys. Lett. **79**, 57003 (2007).

[3] D. Xiao, W. Yao, and Q. Niu, Phys. Rev. Lett. **99**, 236809 (2007).

[4] J. R. Schaibley, H. Yu, G. Clark, P. Rivera, J. S. Ross, K. L. Seyler, W. Yao, and X. Xu, Nat. Rev. Mater. **1**, 16055 (2016).

[5] R. V. Gorbachev, J. C. W. Song, G. L. Yu, A. V. Kretinin, F. Withers, Y. Cao, A. Mishchenko, I. V. Grigorieva, K. S. Novoselov, L. S. Levitov, and A. K. Geim, Science **346**, 448 (2014).

[6] D. R. da Costa, A. Chaves, S. H. R. Sena, G. A. Farias, and F. M. Peeters, Phys. Rev. B **92**, 045417 (2015).

[7] J. Jung, F. Zhang, Z. Qiao, and A. H. MacDonald, Phys. Rev. B **84**, 075418 (2011).

[8] C. Lee, X. Wei, W. Kysar, and J. Hone, Science **321**, 385 (2008).

[9] N. Levy, S. Burke, K. L. Meaker, N. Panlasigui, A. Zettl, F. Guinea, A. Neto, and M. Crommie, Science **329**, 544 (2010).

[10] R. Carrillo-Bastos, D. Faria, A. Latgé, F. Mireles, and N. Sandler, Phys. Rev. B **90**, 041411(R) (2014).

[11] M. Schneider, D. Faria, S. Viola Kusminskiy, and N. Sandler, Phys. Rev. B **91**, 161407(R) (2015).

[12] M. Settnes, S. R. Power, M. Brandbyge, and A.-P. Jauho, Phys. Rev. Lett. **117**, 276801 (2016).

[13] S. P. Milovanović and F. M. Peeters, Appl. Phys. Lett. **109**, 203108 (2016).

[14] V.-T. Tran, J. Saint-Martin, and P. Dollfus, Phys. Rev. B **102**, 075425 (2020).

[15] H. Yu, A. Kutana, and B. I. Yakobson, Nano Lett. **22**, 2934 (2022).

[16] D. Zhai and N. Sandler, Mod. Phys. Lett. B **33**, 1930001 (2019).

[17] N. N. Klimov, S. Jung, S. Zhu, T. Li, C. A. Wright, S. D. Solares, D. B. Newell, N. B. Zhitenev, and J. A. Stroscio, Science **336**, 1557 (2012).

[18] V. Torres, P. Silva, E. A. T. de Souza, L. A. Silva, and D. A. Bahamon, Phys. Rev. B **100**, 205411 (2019).

[19] D. Giambastiani, F. Colangelo, A. Tredicucci, S. Roddaro, and A. Pitanti, J. Appl. Phys. **131**, 085103 (2022).

[20] Y. Jiang, T. Low, K. Chang, M. I. Katsnelson, and F. Guinea, Phys. Rev. Lett. **110**, 046601 (2013).

[21] F. von Oppen, F. Guinea, and E. Mariani, Phys. Rev. B **80**, 075420 (2009).

[22] M. J. Wang, J. Wang, and J. F. Liu, Europhys. Lett. **121**, 47002 (2018).

[23] W. Ortiz, N. Szpak, and T. Stegmann, Phys. Rev. B **106**, 035416 (2022).

[24] E. Sela, Y. Bloch, F. von Oppen, and M. B. Shalom, Phys. Rev. Lett. **124**, 026602 (2020).

[25] J. Amasay and E. Sela, Phys. Rev. B **104**, 125428 (2021).

[26] J. S. Bunch, A. M. van der Zande, S. S. Verbridge, I. W. Frank, D. M. Tanenbaum, J. M. Parpia, H. G. Craighead, and P. L. McEuen, Science **315**, 490 (2007).

[27] M. Jung, P. Rickhaus, S. Zihlmann, A. Eichler, P. Makk, and C. Schönenberger, Nanoscale **11**, 4355 (2019).

[28] A. Raoux, M. Morigi, J.-N. Fuchs, F. Piéchon, and G. Montambaux, Phys. Rev. Lett. **112**, 026402 (2014).

[29] J. Vidal, R. Mosseri, and B. Douçot, Phys. Rev. Lett. **81**, 5888 (1998).

[30] J. Vidal, P. Butaud, B. Douçot, and R. Mosseri, Phys. Rev. B **64**, 155306 (2001).

[31] F. Wang and Y. Ran, Phys. Rev. B **84**, 241103 (2011).

[32] D. Bercioux, D. F. Urban, H. Grabert, and W. Häusler, Phys. Rev. A **80**, 063603 (2009).

[33] A. Filusch and H. Fehske, Eur. Phys. J. B **93**, 169 (2020).

[34] E. Illes, J. P. Carbotte, and E. J. Nicol, Phys. Rev. B **92**, 245410 (2015).

[35] T. Biswas and T. K. Ghosh, J. Phys.: Condens. Matter **28**, 495302 (2016).

[36] E. Illes and E. J. Nicol, Phys. Rev. B **95**, 235432 (2017).

[37] A. Filusch, C. Wurl, and H. Fehske, Eur. Phys. J. B **93**, 59 (2020).

[38] N. Weekes, A. Iurov, L. Zhemchuzhna, G. Gumbs, and D. Huang, Phys. Rev. B **103**, 165429 (2021).

[39] S. M. Cunha, D. R. da Costa, J. M. Pereira, R. N. Costa Filho, B. Van Duppen, and F. M. Peeters, Phys. Rev. B **105**, 165402 (2022).

[40] S. K. F. Islam and P. Datta, Phys. Rev. B **96**, 045418 (2017).

[41] M. Vigh, L. Oroszlány, S. Vajna, P. San-Jose, G. Dávid, J. Cserti, and B. Dóra, Phys. Rev. B **88**, 161413(R) (2013).

[42] Y.-R. Chen, Y. Xu, J. Wang, J.-F. Liu, and Z. Ma, Phys. Rev. B **99**, 045420 (2019).

[43] C.-Z. Wang, H.-Y. Xu, L. Huang, and Y.-C. Lai, Phys. Rev. B **96**, 115440 (2017).

[44] R. Soni, N. Kaushal, S. Okamoto, and E. Dagotto, Phys. Rev. B **102**, 045105 (2020).

[45] Z. F. Wang and F. Lui, Nanoscale **3**, 4201 (2011).

[46] T. Neupert, L. Santos, C. Chamon, and C. Mudry, Phys. Rev. Lett. **106**, 236804 (2011).

[47] X. Cheng, B. Zhou, B. Zhou, and G. Zhou, J. Phys.: Condens. Matter **33**, 215301 (2021).

[48] B. Dey and T. K. Ghosh, Phys. Rev. B **98**, 075422 (2018).

[49] M. A. Mojarro, V. G. Ibarra-Sierra, J. C. Sandoval-Santana, R. Carrillo-Bastos, and G. G. Naumis, Phys. Rev. B **101**, 165305 (2020).

[50] A. Iurov, L. Zhemchuzhna, G. Gumbs, D. Huang, and P. Fekete, Phys. Rev. B **105**, 115309 (2022).

[51] S. Cheng and G. Xianlong, Phys. Rev. Res. **4**, 033194 (2022).

[52] B. Dey and T. K. Ghosh, Phys. Rev. B **99**, 205429 (2019).

[53] H.-Y. Xu, L. Huang, D. Huang, and Y.-C. Lai, Phys. Rev. B **96**, 045412 (2017).

[54] F. Bouhadida, L. Mandhour, and S. Charfi-Kaddour, Phys. Rev. B **102**, 075443 (2020).

[55] W. Zeng and R. Shen, Phys. Rev. B **106**, 094503 (2022).

[56] A. Filusch, A. R. Bishop, A. Saxena, G. Wellein, and H. Fehske, Phys. Rev. B **103**, 165114 (2021).

[57] J. Sun, T. Liu, Y. Du, and H. Guo, Phys. Rev. B **106**, 155417 (2022).

[58] C. W. Groth, M. Wimmer, A. R. Akhmerov, and X. Waintal, New J. Phys. **16**, 063065 (2014).

[59] F. Qi, X.-T. Shi, F.-F. Liu, and D. V. Kruchinin, J. Appl. Anal. Comput. **7**, 857 (2017).

[60] *Table of Integrals, Series, and Products*, 8th ed., edited by D. Zwillinger, V. Moll, I. Gradshteyn, and I. Ryzhik (Academic Press, Boston, 2014).

[61] V. M. Pereira and A. H. Castro Neto, Phys. Rev. Lett. **103**, 046801 (2009).

[62] J. V. Sloan, A. A. P. Sanjuan, Z. Wang, C. Horvath, and S. Barraza-Lopez, Phys. Rev. B **87**, 155436 (2013).

[63] S. Kohler, J. Lehmann, and P. Hänggi, Phys. Rep. **406**, 379 (2005).

[64] M. Fruchart, P. Delplace, J. Weston, X. Waintal, and D. Carpentier, Phys. E **75**, 287 (2016).

[65] T. Kitagawa, T. Oka, A. Brataas, L. Fu, and E. Demler, Phys. Rev. B **84**, 235108 (2011).

[66] H. H. Yap, L. Zhou, J.-S. Wang, and J. Gong, Phys. Rev. B **96**, 165443 (2017).

[67] C. H. Lewenkopf and E. R. Mucciolo, J. Comput. Electron. **12**, 203 (2013).

[68] G. Thorgilsson, G. Viktorsson, and S. Erlingsson, J. Comput. Phys. **261**, 256 (2014).

[69] T. Stegmann and N. Szpak, 2D Mater. **6**, 015024 (2018).

[70] A. Weiße, G. Wellein, A. Alvermann, and H. Fehske, Rev. Mod. Phys. **78**, 275 (2006).

[71] B. Bäuml, G. Wellein, and H. Fehske, Phys. Rev. B **58**, 3663 (1998).

[72] H. Haug and A.-P. Jauho, *Quantum Kinetics in Transport and Optics of Semiconductors* (Springer, Berlin, Heidelberg, 2008).

[73] J.-S. Wang, J. Wang, and J. T. Lü, Eur. Phys. J. B **62**, 381 (2008).

[74] W. Magnus, Commun. Pure Appl. Math. **7**, 649 (1954).

[75] M. Jamotte, N. Goldman, and M. Di Liberto, Commun. Phys. **5**, 30 (2022).

[76] M. Weinberg, C. Staarmann, C. Ölschläger, J. Simonet, and K. Sengstock, 2D Mater. **3**, 024005 (2016).

[77] G. Jotzu, M. Messer, R. Desbuquois, M. Lebrat, T. Uehlinger, D. Greif, and T. Esslinger, Nature (London) **515**, 237 (2014).

Singular flat bands in the modified Haldane-Dice model

Alexander Filusch[a,*], Holger Fehske[a,b]

[a]*Institute of Physics, University Greifswald, , Greifswald, 17489, Germany*
[b]*Erlangen National High Performance Computing Center, , Erlangen, 91058, Germany*

ARTICLE INFO

ABSTRACT

Flat bands can be divided into singular and non-singular ones according to the behavior of their Bloch wave function around band-crossing points in momentum space. We analyze the flat band in the Dice model, which can be tuned by a uniaxial strain in the zigzag direction and a Haldane-type next-nearest neighbor interaction, and derive the topological phase diagram of the modified Haldane-Dice model to obtain all band-gap closings with the central band flat. We determine the compact localized state and classify the behavior of the flat band at all band-crossing points according to the quantum distance of its Bloch wave function. We find that the flat band remains singular for all band-touching points (topological phase transitions) with a maximal quantum distance and give expressions for the resulting non-contractible loop states on the real-space torus.

1. Introduction

Flat bands are dispersionless, i.e., have constant energy throughout the entire Brillouin zone, implying that their charge carriers have zero group velocity (or infinite effective mass) and a diverging density of states [1–3]. Because of the quenched kinetic energy, the charge carriers are then dominated by the electron-electron interaction, making flat-band systems an ideal platform to study the fractional quantum Hall effect [4, 5], superconductivity [6, 7], and Wigner crystallization [8]. Experimentally, various systems with perfectly flat energy bands have been accomplished in, e.g., optical [9, 10] and photonic lattices [11–13] or metamaterials [14].

The perfectly localized eigenstates of the flat band can be used for the classification of flat bands and their generators [15–18]. Due to the destructive interference, these compact localized states (CLS) have nonzero amplitude only inside a finite real-space region and remain intact under time-evolution [16, 19–21]. The basis of an isolated flat band in a lattice of N unit cells is spanned by the N linearly independent CLS generated by lattice translations. In the class of singular flat bands, however, this set is linearly dependent on a real-space torus (periodic boundaries) because dispersive bands cross the flat band in the Brillouin zone. Therefore the set of all CLS must be complemented by so-called non-contractible loop states (NLS), which extend around the torus along one spatial direction while being localized along the other and cannot be smoothly deformed by the CLS [21, 22]. The existence of CLS and NLS have been demonstrated for photonic Lieb and Kagome lattices [11–13, 23, 24]. Interestingly, the band crossing point is directly related to an immovable singularity in the Bloch wave function of the flat band in momentum space [3, 21] and is measured by the maximum Hilbert-Schmidt quantum distance [25].

This has direct consequences for systems with quadratic band-touching points, giving rise to anomalous Landau levels [26] and boundary modes through the bulk-interface correspondence [25]. The full quantum metric tensor, whose real part is the quantum distance, has recently attracted a lot of attention in the context of superconductivity [27–29], the geometric orbital susceptibility [30], and the dc linear conductivity [31].

Historically, the Dice (or $\mathcal{T}_3$) lattice [19, 32, 33], a honeycomb lattice with an extra atom C placed in the center of each hexagon and coupled to only one of the sublattices A or B [cf. Figure 1(a)], is perhaps the earliest example of a flat-band system. The spectrum of the Dice model consists of a strictly flat band, crossing the respective Dirac cones around the K and K' points inherited from graphene's band structure.

The chiral flat band has been shown to be stable against perturbations of the transfer amplitude like strain, magnetic fields, or boundary conditions due to the bipartite nature of the lattice and plays only a secondary role for the single-particle transport properties [19, 34–40], but its geometry and composition have not yet been discussed in detail.

In this paper, we address these issues, analyzing the Dice model under a uniaxial strain along the zigzag orientation with a Haldane-type next-nearest neighbor (NNN) interaction. The uniaxial strain breaks the threefold rotational (C_3) symmetry and trimerizes the model along the y-axis. The Haldane term breaks time-reversal symmetry without a net flux and drives a topological phase transition to Chern insulator in the Dice model characterized by the Chern number $c = \pm 2$ [41–43]. By studying the quantum distance in the vicinity of the band-crossing points at the phase transition of the suchlike modified Haldane-Dice model, we show that the singularity of the flat band is related to its geometry. We confirm this by showing that the set of the CLS is linearly dependent and presenting expressions for the NLS.

*Corresponding author

✉ alexander.filusch@uni-greifswald.de (A. Filusch);
fehske@physik.uni-greifswald.de (H. Fehske)
ORCID(s): 0000-0003-1581-9388 (A. Filusch); 0000-0003-2146-8203 (H. Fehske)

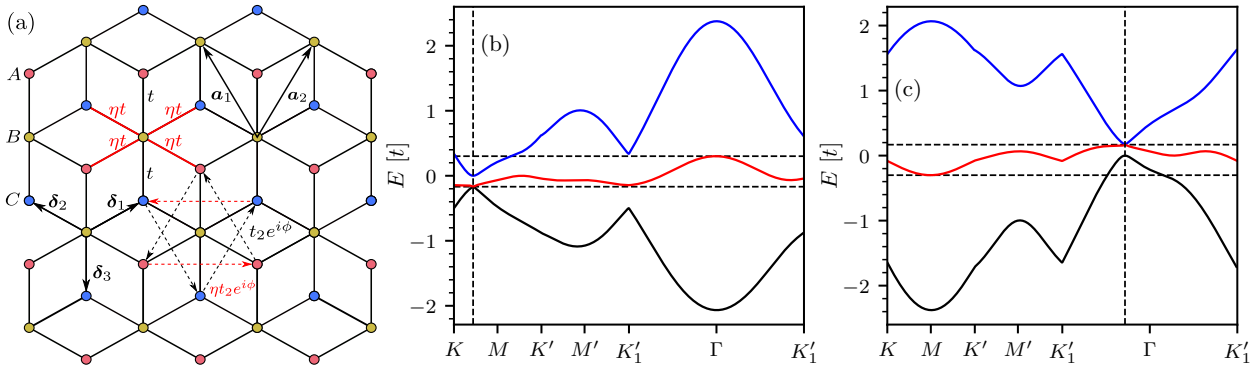Singular flat bands in the modified Haldane-Dice model

Figure 1: (a) Modified Haldane-Dice model with basis $\{A, B, C\}$ and Bravais lattice vectors $a_1 = (-\sqrt{3}/2, 3/2)$ and $a_2 = (\sqrt{3}/2, 3/2)$. The NN vectors connecting the B sites with C sites are given by $\delta_1 = (\sqrt{3}, 1)/2$, $\delta_2 = (-\sqrt{3}, 1)/2$ and $\delta_3 = (0, -1)$. (b),(c) Band structure along the high-symmetry directions with a Haldane flux $\phi = 0.3\pi$ at the topological phase transition $m_c(\phi, \eta)$ of Equation (5) between two valence-gapped phases for $\eta = 0.6$ (a) or between two conduction-gapped phases $\eta = -0.6$ (b). The vertical dashed line denotes the band-crossing point $\mathbf{k}_c$ in the Brillouin zone. Horizontal dashed lines denote the maximum and minimum of the central band.

2. Modified Haldane-Dice model and phase diagram

We start by introducing the Hamiltonian of the modified Haldane-Dice model (MHDM),

$$H_\eta = \left[\frac{1}{\sqrt{2}} \sum_{\langle i,j \rangle} t_{ij} c_i^\dagger c_j + \sum_{\langle\langle i,j \rangle\rangle} t_{2,ij} e^{-i\nu_{ij}\phi} c_i^\dagger c_j + \text{h.c.} \right]$$
$$+ m \sum \epsilon_i c_i^\dagger c_j, \tag{1}$$

obtained by applying uniaxial strain along the x direction. Here, the nearest-neighbor (NN) transfer amplitudes are $t_{ij} = t$ along the $\pm\delta_3$ direction and $t_{ij} = \eta t$ along the $\pm\delta_1$ and $\pm\delta_2$ direction [cf. Figure 1(a)]. The NNN couplings acquire an alternating magnetic phase accounted for by the sign $\nu_{ij} = 1$ (-1) when the hopping between A-A and C-C is clockwise (anti-clockwise). The NNN hoppings in the B sublattice are suppressed [42]. The value of the NNN transfer is $t_{2,ij} = \eta t_2$ $[t_2]$ along $a_3 = a_1 + a_2$ [a_1 and a_2]. By making the NN and NNN couplings unequal, the C_3 rotational symmetry is broken. The inversion-symmetry breaking on-site potential (Semenoff mass) is denoted by m, where $\epsilon_i = 1, 0, -1$ when i refers to the A, B or C sublattice, respectively. Throughout this work, we consider $\eta \in [-1, 1]$. In momentum space, the Hamiltonian becomes

$$H_\eta(\mathbf{k}) = 2t_2 h_0^\eta(\mathbf{k}) \cos(\phi) S_0 + \left[m - 2t_2 h_z^\eta(\mathbf{k}) \sin(\phi) \right] S_z$$
$$+ t f_\eta(\mathbf{k}) S_x, \tag{2}$$

where

$$f_\eta(\mathbf{k}) = \eta \left(e^{i\mathbf{k}\cdot\mathbf{a}_1} + e^{i\mathbf{k}\cdot\mathbf{a}_2} \right) + 1,$$
$$h_0^\eta(\mathbf{k}) = \eta \cos(\mathbf{k}\cdot\mathbf{a}_3) + \cos(\mathbf{k}\cdot\mathbf{a}_2) + \cos(\mathbf{k}\cdot\mathbf{a}_1),$$
$$h_z^\eta(\mathbf{k}) = \eta \sin(\mathbf{k}\cdot\mathbf{a}_3) + \sin(\mathbf{k}\cdot\mathbf{a}_2) - \sin(\mathbf{k}\cdot\mathbf{a}_1). \tag{3}$$

In Equation (2), the matrices S_x, S_z are the usual spin-1 matrices, and $S_0 = \text{diag}(1, 0, 1)$.

To determine the topological properties of the MHDM, we consider the Chern numbers for each band n [44],

$$c_n = \frac{1}{2\pi} \iint_{\text{BZ}} \Omega^{(n)}(k_x, k_y) \, dk_x \, dk_y, \tag{4}$$

where $\Omega(k_x, k_y) = \left[\nabla_\mathbf{k} \times \mathbf{A}^{(n)} \right]_z$ is the Berry curvature, $\mathbf{A}^{(n)} = \langle u_n(\mathbf{k})|i\nabla_\mathbf{k}|u_n(\mathbf{k})\rangle$ is the Berry connection, and $|u_n(\mathbf{k})\rangle$ denotes a Bloch state.

Although the gap-closings are identical to that of the modified Haldane model of graphene [45], the situation is slightly different due to the three-band character. Here, the finite NNN transfer generally distorts the central band, only a Haldane flux of $\phi_c = (2n + 1)\pi/2$ with integer n restores the flatness [42]. In this case, the flat band has always $c = 0$ [46]. Therefore, the band structure of the MHDM differentiates between the valence-band gapped, conduction-band gapped, and all-band gapped phases. For example, the valence-gapped phase has a direct gap between the central band and the valence band and an indirect overlap between the central band and the conduction band. Figure 1(b) [(c)] displays the band structure of the MHDM at the phase boundary between two valence-band gapped phases [conduction-band gapped phases]. In Figure 2, we show the Chern numbers obtained by the discretized Brillouin zone method of Fukui *et al.* [47] for the valence band in the valence-band and all-band gapped phases or for valence and flat band in the conduction-band gapped phase. For Fermi energies inside the indirect gap, the overlapping central and conduction/valence band gives the system a metallic character [cf. Figure 1(b) and (c)].

In the unmodified case ($\eta = 1$), the system undergoes a topological phase transition from a Chern insulator with $c = \pm 2$ to a trivial insulator when $m_c = \pm 3\sqrt{3} \sin\phi$ [42]. The band-gap closing occurs at the K or K' points since the Hamiltonian in Equation (2) is C_3 symmetric [42]. For

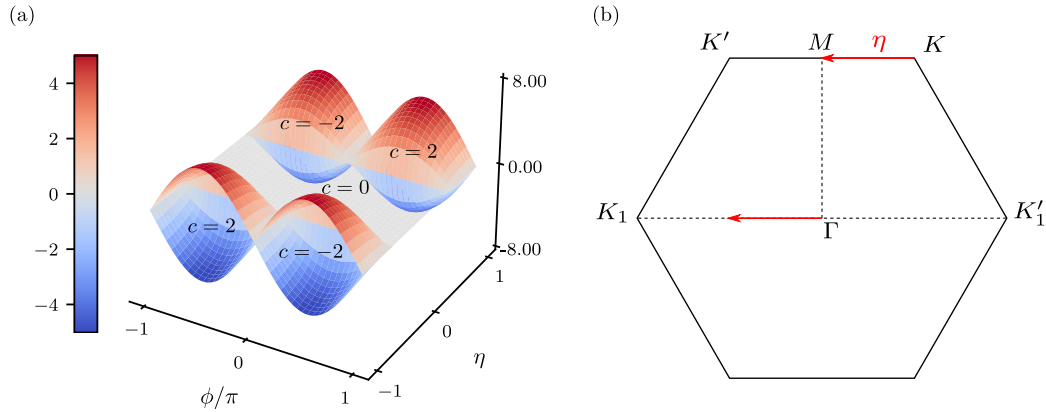Singular flat bands in the modified Haldane-Dice model

Figure 2: (a) Phase diagram of the modified Haldane-Dice model. The Chern numbers are displayed for the valence or valence and flat band. (b) Variation of the band crossing in the Brillouin zone for positive m_c in dependence on η.

$\eta \in [-1, -0.5) \cup (0.5, 1]$, we find that the surface

$$m_c(\phi, \eta) = \pm 3t_2 \sin\phi \sqrt{4 - \frac{1}{\eta^2}} \tag{5}$$

describes the gap-closing/reopening in the parameter space, separating the Chern-insulating phase of the MHDM with $c = \pm 2$ from a trivial insulator.

To understand the gap opening in terms of the strain, we monitor the position of the band crossings in the Brillouin zone. On the surface given by Equation (5), the MHDM has one or two band-crossing points depending on the time-reversal symmetry. For $\phi = \phi_c$, the system is a semimetal that hosts one pseudospin-1 Dirac node in the Brillouin zone. The presence of time-reversal symmetry ($\phi = 0, \pi$) enforces the appearance of two band-crossing points. In all cases, the position of the Dirac nodes depends merely on η. We find that the conduction or valence band touches the central band at $\mathbf{k}_c = \left[\text{sgn}(m_c)k_x^\eta, k_y^\eta\right]$, where

$$k_x^\eta = \frac{2}{\sqrt{3}} \arccos \frac{1}{2\eta} - \Theta\left(\frac{1}{2} - \eta\right)\frac{2\pi}{\sqrt{3}} \tag{6}$$

and $k_y^\eta = 2\pi/3$ for $\eta \geq 1/2$ and $k_y^\eta = 0$ for $\eta \leq -1/2$, respectively. The position of the band-crossings $\mathbf{k}_c$ is located on the symmetry-invariant lines $K'-M-K$ and $K_1-\Gamma-K_1'$ [cf. Figure 1(b) and (c)], and depends on the η parameter as illustrated in Figure 2(b) for positive m_c. By reducing $\eta \to 1/2$, the C_3 symmetry is broken and the Dirac node is no longer pinned to the symmetry point K and moves to M. At $\eta = 1/2$, the two Dirac nodes merge at the M point and gap out. The MHDM remains gapped for smaller η due to the trimerization. For $\eta = -1/2$, the Dirac node reappears at the Γ point and moves towards the K_1 point when $\eta \to -1$.

3. Singular band touchings

To determine whether the flat band is singular, we evaluate the Hilbert-Schmidt quantum distance [48]

$$d(\mathbf{k}_1, \mathbf{k}_2) = 1 - |\langle \Psi_{\text{FB}}(\mathbf{k}_1) | \Psi_{\text{FB}}(\mathbf{k}_2) \rangle|^2 \tag{7}$$

of the flat-band eigenstates in the vicinity of the band-touching points. Typically, the quantum distance vanishes for two eigenstates that are arbitrarily close to each other. In the singular case, however, this quantity is nonzero for $|\mathbf{k}_1 - \mathbf{k}_2| \to 0$ [26]. The maximum value of the quantum distance $d_{\max}$ has been recently taken as a measure of the singularity of the band-crossing point, where any $d_{\max} > 0$ implies the linear dependence of the CLS and the existence of NLS [3, 25, 26].

Let us now inspect the geometric properties of MHDM when the central band is flat, i.e., $E = 0$ [$\phi_n = (2n + 1)\pi/2$] at the phase transitions curves $m = m_c(\eta, \phi_n)$ [cf. Figure 3(a)]. In the following, we will show that a nonzero $d_{\max}$ also implies a singular flat band for Dirac semimetal phases. The eigenstate of the flat band in these cases is given by

$$|\Psi_{\text{FB}}(\mathbf{k})\rangle = \mathcal{N}_{\mathbf{k}} \begin{pmatrix} f_\eta(\mathbf{k}) \\ -(m_c - 2t_2 h_z^\eta(\mathbf{k})) \\ -f_\eta(\mathbf{k})^* \end{pmatrix}, \tag{8}$$

where $\mathcal{N}_{\mathbf{k}} = \left\{2|f_\eta(\mathbf{k})|^2 + (m_c - h_z^\eta(\mathbf{k}))^2\right\}^{-1/2}$ is the normalization constant. In general, the value of $d(\mathbf{k}_1, \mathbf{k}_2)$ depends on how we approach the singular point $\mathbf{k}_c$. Therefore we use the parameterization $\mathbf{k}_{1/2} = \mathbf{k}_c + \mathbf{q}_{1/2}(\cos\theta_{\mathbf{q}_{1/2}}, \sin\theta_{\mathbf{q}_{1/2}})$ and first consider $\eta \neq \pm 1/2$. In this case, we have $m_c - 2t_2 h_z^\eta(\mathbf{k}_{1/2}) = 0$ in the vicinity of $\mathbf{k}_c$ and the quantum distance for small $q_{1/2}$ is given by

$$d(\mathbf{k}_1, \mathbf{k}_2) = \sin^2\left(\Theta_{\mathbf{k}_1} - \Theta_{\mathbf{k}_2}\right), \tag{9}$$

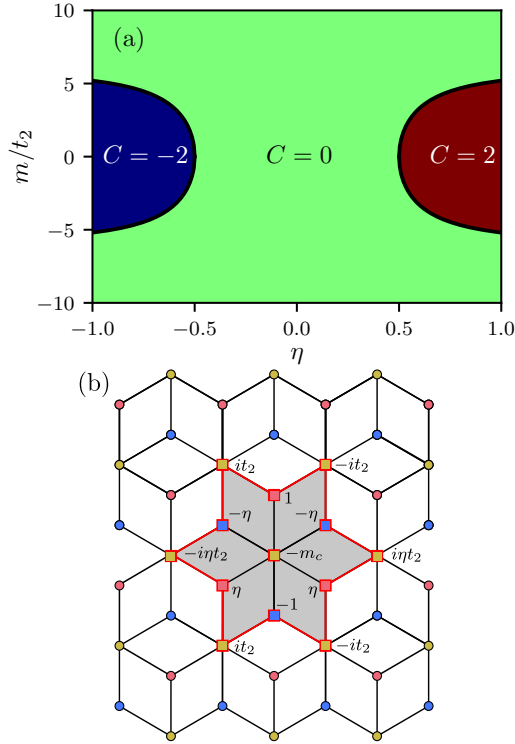Singular flat bands in the modified Haldane-Dice model

Figure 3: (a) Chern numbers in the Dirac semimetal phase ($\phi = \pi/2$) for the valence band. (b) Real-space distribution of the (unnormalized) compact localized state on the Dice lattice, where the squared site symbols denote its nonzero amplitude. The NNN couplings are not drawn for better visibility.

where $\Theta_{\mathbf{k}} = i \log f_\eta(\mathbf{k})/|f_\eta(\mathbf{k})|$. This is similar to neglecting the NNN interaction. However, at $\eta = \pm 1/2$, $m_c(\eta = \pm 1/2) = 0$, the full wave function has to be used which affects the angular dependence but not its maximum value. In the limit $q_{1/2} \to 0$, we find the unit maximum quantum distance $d_{\max} = 1$ for, e.g., $\theta_{\mathbf{q}_1} = \pi/2$ and $\theta_{\mathbf{q}_2} = (2j+1)\pi$ for integer j and independent of η.

At this point, we like to note that in the closely related α-$\mathcal{T}_3$ model [49], the parameter α interpolates between the honeycomb lattice ($\alpha = 0$) with a decoupled flat band and the Dice lattice ($\alpha = 1$) rescaling the hoppings between B and C sites by α. In this case, we find $d(\mathbf{k}_1, \mathbf{k}_2) = \sin^2(\Theta_{\mathbf{k}_1} - \Theta_{\mathbf{k}_2}) \sin^2 2\varphi$ with $\tan\phi = \alpha$. Thereby, the resulting $d_{\max} = \sin^2 2\varphi$ is a direct measure for the interband coupling between the flat band and the Dirac nodes.

To confirm the predictions by the maximal quantum distance, we consider a (Dice) lattice of N unit cells with $\phi_0 = \pi/2$ and $m = m_c(\eta, \phi_0)$, i.e., the MHDM where the conduction and valence band touch the perfectly flat band at $\mathbf{k}_c$. We construct the compact localized state of the flat-band states by combining all Bloch wave functions into new eigenfunctions,

$$|\chi(\mathbf{R})\rangle = \mathcal{N} \sum_{\mathbf{k} \in \text{BZ}} \alpha_{\mathbf{k}} e^{-i\mathbf{k}\cdot\mathbf{R}} |\Psi_{\text{FB}}(\mathbf{k})\rangle, \tag{10}$$

where $\mathcal{N}$ is a normalization constant and $\alpha_{\mathbf{k}}$ is a smooth function of the momentum. The Bloch eigenstate can be brought in the form

$$|\Psi_{\text{FB}}(\mathbf{k})\rangle = \frac{1}{\sqrt{N}} \sum_{\mathbf{R}'} e^{i\mathbf{k}\cdot\mathbf{R}'} u_{\mathbf{k},j} |\mathbf{R}', j\rangle, \tag{11}$$

where $u_{\mathbf{k},j}$ is the jth component of the normalized eigenvector of the flat band. By choosing $\alpha_{\mathbf{k}} = \mathcal{N}_{\mathbf{k}}^{-1}$, $\alpha_{\mathbf{k}} |\Psi_{\text{FB}}(\mathbf{k})\rangle$ is simply a sum of Bloch phases and we directly obtain the CLS real-space distribution centered around $\mathbf{R}'$,

$$\langle \mathbf{R}', j | \chi(\mathbf{R}) \rangle = \frac{1}{\sqrt{2 + 6\eta^2 + 4t_2^2 + m_c^2}}$$

$$\cdot \begin{pmatrix} \eta \left[\delta_{\mathbf{R}'-\mathbf{R}+a_1} + \delta_{\mathbf{R}'-\mathbf{R}+a_2} \right] + \delta_{\mathbf{R}'-\mathbf{R}} \\ -m_c - it_2 \sum_{i=1}^{3} \beta_i \left(\delta_{\mathbf{R}'-\mathbf{R}-a_i} - \delta_{\mathbf{R}'-\mathbf{R}+a_i} \right) \\ -\eta \left[\delta_{\mathbf{R}'-\mathbf{R}-a_1} + \delta_{\mathbf{R}'-\mathbf{R}-a_2} \right] - \delta_{\mathbf{R}'-\mathbf{R}} \end{pmatrix}, \tag{12}$$

where the amplitudes are $\beta_1 = \eta$ and $\beta_{i\neq 1} = 1$. Figure 2(a) displays the (unnormalized) CLS. Due to the NNN coupling, the CLS of the pristine Dice lattice [19] is extended by complex amplitudes on the outer B atoms. The additional nonzero amplitude on the central B atom compensates the sublattice-symmetry breaking Semenoff mass. The CLS $|\chi(\mathbf{R})\rangle$ can be considered as the extreme limit of localized Wannier functions [15].

For N unit cells, one would expect N eigenstates with zero energy from the flat band and two additional states stemming from the Dirac cone. In a system with periodic boundary conditions however, we can easily verify that $\sum_n e^{i\mathbf{k}_c \mathbf{R}_n} |\chi(\mathbf{R}_n)\rangle = 0$, which renders the set spanned by all CLS linearly dependent. Thus, we are left with a set of $(N-1)$ CLS, quite similar to the pristine case [22]. Therefore, we give expressions for the three missing zero-energy eigenstates in Figure 4 that complete the set. We find two NLS that extend along the a_3 and a_2 direction (or, equivalently, any two choices of the three a_i), which are displayed in Figure 4(a) and Figure 4(b), respectively. Each non-contractible loop state consists of a unit plaquette with nonzero amplitude on its edge sites (dashed box). The full non-contractible loop state is then generated by shifting the plaquette and multiplying by a phase factor $\exp\{i\mathbf{k}_c \cdot n a_{3/2}\}$. For the NLS along a_3 and a_2, this yields a phase factor of $e^{i\omega_\eta}$ and $-e^{i\omega_\eta/2}$, respectively. Additionally, we find an extended state in Figure 4(c) with nonzero amplitudes only on the B atoms. This state has been overlooked previously [22].

Finally, let us explicitly demonstrate that the NLS of Figure 4(a) is an exact eigenstate with zero energy by using the picture of destructive interferences. First, we consider the B site with weight $-m_c e^{i\omega_\eta/2}/3$ [cf. yellow square inside dashed box of Figure 4(a)]. Since this B site is only coupled to its NN [cf. Equation (1)] and H_η has no onsite potential on the B sublattice, applying H_η yields $\eta + \eta e^{i\omega_\eta} - e^{i\omega_\eta/2} = 0$ on this site. The remaining hoppings cancel each other, which
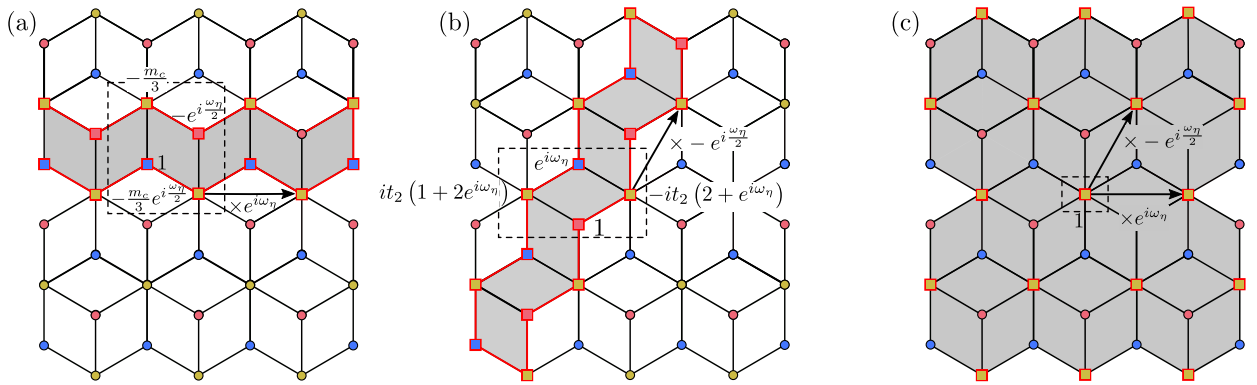
Singular flat bands in the modified Haldane-Dice model

Figure 4: (a),(b) Non-contractible loop states winding along a_3 and a_2, respectively, around the torus. The phase factor is defined by $\omega_\eta = 2\arccos(1/2\eta)$. All sites with nonzero amplitude are indicated by squares on the edges of the gray plaquettes. The values of the amplitudes are given for the unit plaquette (dashed box) and all other plaquettes can be constructed by shifting the unit plaquette via the phase factor along the arrow. (c) An extended state with nonzero amplitude only on the B sites. The remaining amplitudes on the B sites are obtained by shifting the nonzero amplitude in the dashed box by the phase factor along the two arrows.

can be seen by noting that $m_c = -3it_2\eta(e^{i\omega_\eta} - e^{-i\omega_\eta}) = -3it_2(e^{i\omega_\eta/2} - e^{-i\omega_\eta/2})$ and collecting the NN and NNN contributions. Due to translation symmetry, the NLS is then an eigenstate. Similarly, one can show that the NLS along a_2 is also an eigenstate.

4. Conclusions

In summary, we studied the Haldane-Dice model with broken $\mathcal{C}_3$ symmetry due to different couplings between NN and NNN sites particularly with regard to its topological properties and the geometry of the flat band. In experiments, this could be realized by applying uniaxial strain to related systems. We found the same topological phase diagram as in the modified Haldane model based on graphene, albeit with an increased Chern number $c = \pm 2$. From the phase diagram, we identified the parameters where the central band is dispersionless and determined the shape of the Bloch wave function and composition of the flat band. In particular, we demonstrated that a nonzero maximum Hilbert-Schmidt quantum distance around the band-crossing point in the Dirac semimetal phase directly leads to a linearly dependent set of all compact-localized states in the torus geometry. In this case, we found two non-contractible loop states winding around the torus along the symmetry directions and one extended state on the torus that has not been reported so far. Accordingly, the full physical significance of the quantum metric tensor and quantum distance in this system was open. In this regard, the α-$\mathcal{T}_3$ model and its singular flat band is certainly an ideal platform to study geometric contributions to interband coupling effects arising from the α-dependent quantum distance around the band-crossing points.

CRediT authorship contribution statement

Alexander Filusch: Conceptualization, Formal analysis, Investigation, Writing - Original Draft. **Holger Fehske:** Conceptualization, Writing - Reviewing and Editing, Supervision.

References

[1] M. Maksymenko, A. Honecker, R. Moessner, J. Richter, O. Derzhko, Flat-Band Ferromagnetism as a Pauli-Correlated Percolation Problem, Phys. Rev. Lett. 109 (2012) 096404.

[2] D. Leykam, A. Andreanov, S. Flach, Artificial flat band systems: from lattice models to experiments, Advances in Physics: X 3 (2018) 1473052.

[3] J.-W. Rhim, B.-J. Yang, Singular flat bands, Advances in Physics: X 6 (2021) 1901606.

[4] Y.-F. Wang, H. Yao, C.-D. Gong, D. N. Sheng, Fractional quantum Hall effect in topological flat bands with Chern number two, Phys. Rev. B 86 (2012) 201101.

[5] S. A. Parameswaran, R. Roy, S. L. Sondhi, Fractional quantum Hall physics in topological flat bands, Comptes Rendus Physique 14 (2013) 816–839.

[6] T. T. Heikkilä, G. E. Volovik, Dimensional crossover in topological matter: Evolution of the multiple Dirac point in the layered system to the flat band on the surface, JETP Letters 93 (2011) 59–65.

[7] L. Balents, C. R. Dean, D. K. Efetov, A. F. Young, Superconductivity and strong correlations in moiré flat bands, Nature Physics 16 (2020) 725–733.

[8] C. Wu, D. Bergman, L. Balents, S. Das Sarma, Flat Bands and Wigner Crystallization in the Honeycomb Optical Lattice, Phys. Rev. Lett. 99 (2007) 070401.

[9] M. Hyrkäs, V. Apaja, M. Manninen, Many-particle dynamics of bosons and fermions in quasi-one-dimensional flat-band lattices, Phys. Rev. A 87 (2013) 023614.

[10] S. Taie, H. Ozawa, T. Ichinose, T. Nishio, S. Nakajima, Y. Takahashi, Coherent driving and freezing of bosonic matter wave in an optical Lieb lattice, Science Advances 1 (2015) e1500854.

[11] R. A. Vicencio, C. Cantillano, L. Morales-Inostroza, B. Real, C. Mejía-Cortés, S. Weimann, A. Szameit, M. I. Molina, Observation of Localized States in Lieb Photonic Lattices, Phys. Rev. Lett. 114 (2015) 245503.

[12] S. Mukherjee, A. Spracklen, D. Choudhury, N. Goldman, P. Öhberg, E. Andersson, R. R. Thomson, Observation of a Localized Flat-Band State in a Photonic Lieb Lattice, Phys. Rev. Lett. 114 (2015) 245504.

[13] S. Xia, Y. Hu, D. Song, Y. Zong, L. Tang, Z. Chen, Demonstration of flat-band image transmission in optically induced lieb photonic

Singular flat bands in the modified Haldane-Dice model

lattices, Opt. Lett. 41 (2016) 1435–1438.

[14] Y. Nakata, T. Okada, T. Nakanishi, M. Kitano, Observation of flat band for terahertz spoof plasmons in a metallic kagomé lattice, Phys. Rev. B 85 (2012) 205128.

[15] N. Read, Compactly supported Wannier functions and algebraic k-theory, Phys. Rev. B 95 (2017) 115309.

[16] W. Maimaiti, A. Andreanov, H. C. Park, O. Gendelman, S. Flach, Compact localized states and flat-band generators in one dimension, Phys. Rev. B 95 (2017) 115135.

[17] W. Maimaiti, S. Flach, A. Andreanov, Universal $d = 1$ flat band generator from compact localized states, Phys. Rev. B 99 (2019) 125129.

[18] W. Maimaiti, A. Andreanov, S. Flach, Flat-band generator in two dimensions, Phys. Rev. B 103 (2021) 165116.

[19] B. Sutherland, Localization of electronic wave functions due to local topology, Phys. Rev. B 34 (1986) 5208–5211.

[20] H. Aoki, M. Ando, H. Matsumura, Hofstadter butterflies for flat bands, Phys. Rev. B 54 (1996) R17296–R17299.

[21] J.-W. Rhim, B.-J. Yang, Classification of flat bands according to the band-crossing singularity of Bloch wave functions, Phys. Rev. B 99 (2019) 045107.

[22] D. L. Bergman, C. Wu, L. Balents, Band touching from real-space topology in frustrated hopping models, Phys. Rev. B 78 (2008) 125104.

[23] S. Xia, A. Ramachandran, S. Xia, D. Li, X. Liu, L. Tang, Y. Hu, D. Song, J. Xu, D. Leykam, S. Flach, Z. Chen, Unconventional Flatband Line States in Photonic Lieb Lattices, Phys. Rev. Lett. 121 (2018) 263902.

[24] J. Ma, J.-W. Rhim, L. Tang, S. Xia, H. Wang, X. Zheng, S. Xia, D. Song, Y. Hu, Y. Li, B.-J. Yang, D. Leykam, Z. Chen, Observation of non-contractible loop states in a photonic kagome lattice of corbino-geometry, Conference on Lasers and Electro-Optics (2020) FW4A.3.

[25] C.-g. Oh, D. Cho, S. Y. Park, J.-W. Rhim, Bulk-interface correspondence from quantum distance in flat band systems, Communications Physics 5 (2022) 320.

[26] J.-W. Rhim, K. Kim, B.-J. Yang, Quantum distance and anomalous Landau levels of flat bands, Nature 584 (2020) 59–63.

[27] R. L. Klees, G. Rastelli, J. C. Cuevas, W. Belzig, Microwave Spectroscopy Reveals the Quantum Geometric Tensor of Topological Josephson Matter, Phys. Rev. Lett. 124 (2020) 197002.

[28] J. Herzog-Arbeitman, V. Peri, F. Schindler, S. D. Huber, B. A. Bernevig, Superfluid Weight Bounds from Symmetry and Quantum Geometry in Flat Bands, Phys. Rev. Lett. 128 (2022) 087002.

[29] K.-E. Huhtinen, J. Herzog-Arbeitman, A. Chew, B. A. Bernevig, P. Törmä, Revisiting flat band superconductivity: Dependence on minimal quantum metric and band touchings, Phys. Rev. B 106 (2022) 014518.

[30] F. Piéchon, A. Raoux, J.-N. Fuchs, G. Montambaux, Geometric orbital susceptibility: Quantum metric without Berry curvature, Phys. Rev. B 94 (2016) 134423.

[31] J. Mitscherling, T. Holder, Bound on resistivity in flat-band materials due to the quantum metric, Phys. Rev. B 105 (2022) 085154.

[32] J. Vidal, R. Mosseri, B. Douçot, Aharonov-Bohm Cages in Two-Dimensional Structures, Phys. Rev. Lett. 81 (1998) 5888–5891.

[33] J. Vidal, P. Butaud, B. Douçot, R. Mosseri, Disorder and interactions in Aharonov-Bohm cages, Phys. Rev. B 64 (2001) 155306.

[34] T. Biswas, T. K. Ghosh, Magnetotransport properties of the $\alpha\text{-}\mathcal{T}_3$ model, Journal of Physics: Condensed Matter 28 (2016) 495302.

[35] A. Ramachandran, A. Andreanov, S. Flach, Chiral flat bands: Existence, engineering, and stability, Phys. Rev. B 96 (2017) 161104.

[36] D. O. Oriekhov, E. V. Gorbar, V. P. Gusynin, Electronic states of pseudospin-1 fermions in dice lattice ribbon, Low Temperature Physics 44 (2018) 1313–1324.

[37] O. V. Bugaiko, D. O. Oriekhov, Electronic states of pseudospin-1 fermions in $\alpha\text{-}\mathcal{T}_3$ lattice ribbons in a magnetic field, Journal of Physics: Condensed Matter 31 (2019) 325501.

[38] A. Mallick, N. Chang, A. Andreanov, S. Flach, Anti-$\mathcal{PT}$ flatbands, Phys. Rev. A 105 (2022) L021305.

[39] A. Filusch, A. R. Bishop, A. Saxena, G. Wellein, H. Fehske, Valley filtering in strain-induced $\alpha\text{-}\mathcal{T}_3$ quantum dots, Phys. Rev. B 103 (2021) 165114.

[40] A. Filusch, H. Fehske, Tunable valley filtering in dynamically strained $\alpha\text{-}\mathcal{T}_3$ lattices, Phys. Rev. B 106 (2022) 245106.

[41] F. D. M. Haldane, Model for a Quantum Hall Effect without Landau Levels: Condensed-Matter Realization of the "Parity Anomaly", Phys. Rev. Lett. 61 (1988) 2015–2018.

[42] B. Dey, P. Kapri, O. Pal, T. K. Ghosh, Unconventional phases in a Haldane model of dice lattice, Phys. Rev. B 101 (2020) 235406.

[43] S. Mondal, S. Basu, Topological features of the Haldane model on a dice lattice: Flat-band effect on transport properties, Phys. Rev. B 107 (2023) 035421.

[44] D. J. Thouless, M. Kohmoto, M. P. Nightingale, M. den Nijs, Quantized Hall Conductance in a Two-Dimensional Periodic Potential, Phys. Rev. Lett. 49 (1982) 405–408.

[45] B. Wang, X. Zhou, H. Lin, A. Bansil, Higher-order topological insulator phase in a modified Haldane model, Phys. Rev. B 104 (2021) L121108.

[46] L. Chen, T. Mazaheri, A. Seidel, X. Tang, The impossibility of exactly flat non-trivial Chern bands in strictly local periodic tight binding models, Journal of Physics A: Mathematical and Theoretical 47 (2014) 152001.

[47] T. Fukui, Y. Hatsugai, H. Suzuki, Chern Numbers in Discretized Brillouin Zone: Efficient Method of Computing (Spin) Hall Conductances, Journal of the Physical Society of Japan 74 (2005) 1674–1677.

[48] V. V. Dodonov, O. V. Man'ko, V. I. Man'ko, A. Wünsche, Hilbert-Schmidt distance and non-classicality of states in quantum optics, Journal of Modern Optics 47 (2000) 633–654.

[49] A. Raoux, M. Morigi, J.-N. Fuchs, F. Piéchon, G. Montambaux, From Dia- to Paramagnetic Orbital Susceptibility of Massless Fermions, Phys. Rev. Lett. 112 (2014) 026402.

Bibliography

[1] K. S. Novoselov, A. K. Geim, S. V. Morozov, D. Jiang, Y. Zhang, S. V. Dubonos, I. V. Grigorieva, and A. A. Firsov, *Electric field effect in atomically thin carbon films*, Science **306**, 666–669 (2004).

[2] A. K. Geim and K. S. Novoselov, *The rise of graphene*, Nature Materials **6**, 183–191 (2007).

[3] S. Das Sarma, S. Adam, E. H. Hwang, and E. Rossi, *Electronic transport in two-dimensional graphene*, Rev. Mod. Phys. **83**, 407–470 (2011).

[4] V. N. Kotov, B. Uchoa, V. M. Pereira, F. Guinea, and A. H. Castro Neto, *Electron-electron interactions in graphene: current status and perspectives*, Rev. Mod. Phys. **84**, 1067–1125 (2012).

[5] O. Klein, *Die reflexion von elektronen an einem potentialsprung nach der relativistischen dynamik von dirac*, Z. Phys. **53**, 157–165 (1929).

[6] M. I. Katsnelson, K. S. Novoselov, and A. K. Geim, *Chiral tunnelling and the klein paradox in Â graphene*, Nature Physics **2**, 620–625 (2006).

[7] N. Stander, B. Huard, and D. Goldhaber-Gordon, *Evidence for klein tunneling in graphene $p-n$ Junctions*, Phys. Rev. Lett. **102**, 026807 (2009).

[8] K. S. Novoselov, A. K. Geim, S. V. Morozov, D. Jiang, M. I. Katsnelson, I. V. Grigorieva, S. V. Dubonos, and A. A. Firsov, *Two-dimensional gas of massless dirac fermions in graphene*, Nature **438**, 197–200 (2005).

[9] Y. Zhang, Y.-W. Tan, H. L. Stormer, and P. Kim, *Experimental observation of the quantum hall effect and berry's phase in graphene*, Nature **438**, 201–204 (2005).

[10] J. Tworzydło, B. Trauzettel, M. Titov, A. Rycerz, and C. W. J. Beenakker, *Sub-poissonian shot noise in graphene*, Phys. Rev. Lett. **96**, 246802 (2006).

[11] M. Z. Hasan and C. L. Kane, *Colloquium: topological insulators*, Rev. Mod. Phys. **82**, 3045–3067 (2010).

[12] S.-Y. Xu, I. Belopolski, N. Alidoust, M. Neupane, G. Bian, C. Zhang, R. Sankar, G. Chang, Z. Yuan, C.-C. Lee, S.-M. Huang, H. Zheng, J. Ma, D. S. Sanchez, B. Wang, A. Bansil, F. Chou, P. P. Shibayev, H. Lin, S. Jia, and M. Z. Hasan, *Discovery of a weyl fermion semimetal and topological fermi arcs*, Science **349**, 613–617 (2015).

[13] B. Bradlyn, J. Cano, Z. Wang, M. G. Vergniory, C. Felser, R. J. Cava, and B. A. Bernevig, *Beyond dirac and weyl fermions: unconventional quasiparticles in conventional crystals*, Science **353**, aaf5037 (2016).

[14] H. Weng, C. Fang, Z. Fang, and X. Dai, *Topological semimetals with triply degenerate nodal points in θ-phase tantalum nitride*, Phys. Rev. B **93**, 241202 (2016).

[15] H. Weng, C. Fang, Z. Fang, and X. Dai, *Coexistence of weyl fermion and massless triply degenerate nodal points*, Phys. Rev. B **94**, 165201 (2016).

[16] B. Dóra, J. Kailasvuori, and R. Moessner, *Lattice generalization of the dirac equation to general spin and the role of the flat band*, Phys. Rev. B **84**, 195422 (2011).

[17] T. T. Heikkilä and G. E. Volovik, *Dimensional crossover in topological matter: evolution of the multiple dirac point in the layered system to the flat band on the surface*, JETP Letters **93**, 59–65 (2011).

[18] D. Leykam, A. Andreanov, and S. Flach, *Artificial flat band systems: from lattice models to experiments*, Advances in Physics: X **3**, 1473052 (2018).

[19] A. Mielke and H. Tasaki, *Ferromagnetism in the hubbard model*, Communications in Mathematical Physics **158**, 341 (1993).

[20] H. Tasaki, *From nagaoka's ferromagnetism to flat-band ferromagnetism and beyond: an introduction to ferromagnetism in the hubbard model*, Progress of Theoretical Physics **99**, 489–548 (1998).

[21] L. Balents, C. R. Dean, D. K. Efetov, and A. F. Young, *Superconductivity and strong correlations in moiré flat bands*, Nature Physics **16**, 725–733 (2020).

[22] Y.-F. Wang, H. Yao, C.-D. Gong, and D. N. Sheng, *Fractional quantum hall effect in topological flat bands with chern number two*, Phys. Rev. B **86**, 201101 (2012).

[23] S. A. Parameswaran, R. Roy, and S. L. Sondhi, *Fractional quantum hall physics in topological flat bands*, Comptes Rendus Physique **14**, Topological insulators / Isolants topologiques, 816–839 (2013).

[24] Y. Cao, V. Fatemi, S. Fang, K. Watanabe, T. Taniguchi, E. Kaxiras, and P. Jarillo-Herrero, *Unconventional superconductivity in magic-angle graphene superlattices*, Nature **556**, 43–50 (2018).

[25] B. Sutherland, *Localization of electronic wave functions due to local topology*, Phys. Rev. B **34**, 5208–5211 (1986).

[26] J. Vidal, R. Mosseri, and B. Douçot, *Aharonov-bohm cages in two-dimensional structures*, Phys. Rev. Lett. **81**, 5888–5891 (1998).

[27] J. Vidal, P. Butaud, B. Douçot, and R. Mosseri, *Disorder and interactions in aharonov-bohm cages*, Phys. Rev. B **64**, 155306 (2001).

[28] A. Ramachandran, A. Andreanov, and S. Flach, *Chiral flat bands: Existence, engineering, and stability*, Phys. Rev. B **96**, 161104 (2017).

[29] A. Mallick, N. Chang, A. Andreanov, and S. Flach, *Anti-$\mathcal{PT}$ flatbands*, Phys. Rev. A **105**, L021305 (2022).

[30] D. F. Urban, D. Bercioux, M. Wimmer, and W. Häusler, *Barrier transmission of Dirac-like pseudospin-one particles*, Phys. Rev. B **84**, 115136 (2011).

[31] M. Vigh, L. Oroszlány, S. Vajna, P. San-Jose, G. Dávid, J. Cserti, and B. Dóra, *Diverging dc conductivity due to a flat band in a disordered system of pseudospin-1 Dirac-Weyl fermions*, Phys. Rev. B **88**, 161413 (2013).

[32] J. Wang, R. Van Pottelberge, W.-S. Zhao, and F. M. Peeters, *Coulomb impurity on a dice lattice: atomic collapse and bound states*, Phys. Rev. B **105**, 035427 (2022).

[33] A. Raoux, M. Morigi, J.-N. Fuchs, F. Piéchon, and G. Montambaux, *From Dia- to Paramagnetic Orbital Susceptibility of Massless Fermions*, Phys. Rev. Lett. **112**, 026402 (2014).

[34] D. Bercioux, D. F. Urban, H. Grabert, and W. Häusler, *Massless dirac-weyl fermions in a ⊔3 optical lattice*, Phys. Rev. A **80**, 063603 (2009).

[35] E. Serret, P. Butaud, and B. Pannetier, *Vortex correlations in a fully frustrated two-dimensional superconducting network*, Europhysics Letters **59**, 225 (2002).

[36] J Güttinger, F Molitor, C Stampfer, S Schnez, A Jacobsen, S Dröscher, T Ihn, and K Ensslin, *Transport through graphene quantum dots*, Reports on Progress in Physics **75**, 126502 (2012).

[37] P. Hewageegana and V. Apalkov, *Electron localization in graphene quantum dots*, Phys. Rev. B **77**, 245426 (2008).

[38] H.-Y. Xu and Y.-C. Lai, *Revival resonant scattering, perfect caustics, and isotropic transport of pseudospin-1 particles*, Phys. Rev. B **94**, 165405 (2016).

[39] C. Schulz, R. L. Heinisch, and H. Fehske, *Scattering of two-dimensional dirac fermions on gate-defined oscillating quantum dots*, Phys. Rev. B **91**, 045130 (2015).

[40] A. Filusch, C. Wurl, and H. Fehske, *Resonant scattering of dice quasiparticles on oscillating quantum dots*, The European Physical Journal B **93**, 59 (2020).

[41] A. Filusch and H. Fehske, *Electronic properties of $\alpha - \mathcal{T}_3$ quantum dots in magnetic fields*, Eur. Phys. J. B. **93**, 169 (2020).

[42] E. Illes, J. P. Carbotte, and E. J. Nicol, *Hall quantization and optical conductivity evolution with variable berry phase in the $\alpha - T3$ model*, Phys. Rev. B **92**, 245410 (2015).

[43] T. Biswas and T. K. Ghosh, *Magnetotransport properties of the α-$\mathcal{T}_3$ model*, Journal of Physics: Condensed Matter **28**, 495302 (2016).

[44] S. K. Firoz Islam and S. Datta, Phys. Rev. B **96**, 045418 (2017).

[45] H.-Y. Xu, L. Huang, D. Huang, and Y.-C. Lai, *Geometric valley hall effect and valley filtering through a singular berry flux*, Phys. Rev. B **96**, 045412 (2017).

[46] F. Bouhadida, L. Mandhour, and S. Charfi-Kaddour, *Magnetic fabry-pérot interferometer for valley filtering in a honeycomb-dice model*, Phys. Rev. B **102**, 075443 (2020).

[47] W. Zeng and R. Shen, *Pure crossed andreev reflection assisted transverse valley currents in $\alpha - \sqcup 3$ lattices*, Phys. Rev. B **106**, 094503 (2022).

[48] B. Dey and T. K. Ghosh, *Floquet topological phase transition in the $\alpha - \mathcal{T}_3$ lattice*, Phys. Rev. B **99**, 205429 (2019).

[49] S. Cheng and G. Xianlong, *Topological floquet bands in a circularly shaken dice lattice*, Phys. Rev. Research **4**, 033194 (2022).

[50] C. Lee, X. Wei, W. Kysar, and J. Hone, *Measurement of the Elastic Properties and Intrinsic Strength of Monolayer Graphene*, Science **321**, 385 (2008).

[51] N. Levy, S. Burke, K. L. Meaker, N. Panlasigui, A. Zettl, F. Guinea, A. Neto, and M. Crommie, *Strain-Induced Pseudo-Magnetic Fields Greater Than 300 Tesla in Graphene nanobubbles*, Science **329**, 544 (2010).

[52] C.-C. Hsu, M. L. Teague, J.-Q. Wang, and N.-C. Yeh, *Nanoscale strain engineering of giant pseudo-magnetic fields, valley polarization, and topological channels in graphene*, Science Advances **6**, eaat9488 (2020).

[53] A. Rycerz, J. Tworzydło, and C. W. J. Beenakker, *Valley filter and valley valve in graphene*, Nature Physics **3**, 172 (2007).

[54] D. Xiao, W. Yao, and Q. Niu, *Valley-contrasting physics in graphene: magnetic moment and topological transport*, Phys. Rev. Lett. **99**, 236809 (2007).

[55] J. R. Schaibley, H. Yu, G. Clark, P. Rivera, J. S. Ross, K. L. Seyler, W. Yao, and X. Xu, *Valleytronics in 2d materials*, Nat. Rev. Materials **1**, 16055 (2016).

[56] R. Carrillo-Bastos, D. Faria, A. Latgé, F. Mireles, and N. Sandler, *Gaussian deformations in graphene ribbons: flowers and confinement*, Phys. Rev. B **90**, 041411(R) (2014).

[57] M. Schneider, D. Faria, S. Viola Kusminskiy, and N. Sandler, *Local sublattice symmetry breaking for graphene with a centrosymmetric deformation*, Phys. Rev. B **91**, 161407(R) (2015).

[58] M. Settnes, S. R. Power, M. Brandbyge, and A.-P. Jauho, *Graphene Nanobubbles as Valley Filters and Beam Splitters*, Phys. Rev. Lett. **117**, 276801 (2016).

[59] S. P. Milovanović and F. M. Peeters, *Strain controlled valley filtering in multi-terminal graphene structures*, Applied Physics Letters **109**, 203108 (2016).

[60] D. Zhai and N. Sandler, *Electron dynamics in strained graphene*, Modern Physics Letters B **33**, 1930001 (2019).

[61] V.-T. Tran, J. Saint-Martin, and P. Dollfus, *Electron transport properties of graphene nanoribbons with gaussian deformation*, Phys. Rev. B **102**, 075425 (2020).

[62] H. Yu, A. Kutana, and B. I. Yakobson, *Electron optics and valley hall effect of undulated graphene*, Nano Letters **22**, 2934–2940 (2022).

[63] S. Hahn, K. Kim, K. Kim, X. Hu, T. Painter, I. Dixon, S. Kim, K. R. Bhattarai, S. Noguchi, J. Jaroszynski, and D. C. Larbalestier, *45.5-tesla direct-current magnetic field generated with a high-temperature superconducting magnet*, Nature **570**, 496–499 (2019).

[64] E. Illes and E. J. Nicol, *Klein tunneling in the $\alpha - T_3$ model*, Phys. Rev. B **95**, 235432 (2017).

[65] A. R. Akhmerov and C. W. J. Beenakker, *Boundary conditions for dirac fermions on a terminated honeycomb lattice*, Phys. Rev. B **77**, 085423 (2008).

[66] J. A. M. van Ostaay, A. R. Akhmerov, C. W. J. Beenakker, and M. Wimmer, *Dirac boundary condition at the reconstructed zigzag edge of graphene*, Phys. Rev. B **84**, 195434 (2011).

[67] D. O. Oriekhov, E. V. Gorbar, and V. P. Gusynin, *Electronic states of pseudospin-1 fermions in dice lattice ribbon*, Low Temperature Physics **44**, 1313–1324 (2018).

[68] O. V. Bugaiko and D. O. Oriekhov, *Electronic states of pseudospin-1 fermions in α-$\mathcal{T}_3$ lattice ribbons in a magnetic field*, Journal of Physics: Condensed Matter **31**, 325501 (2019).

[69] M. V. Berry and R. Mondragon, *Neutrino billiards: time-reversal symmetry-breaking without magnetic fields*, Proc. R. Soc. Lond. A, 53–74 (1987).

[70] C. W. Groth, M. Wimmer, A. R. Akhmerov, and X. Waintal, *Kwant: a software package for quantum transport*, New Journal of Physics **16**, 063065 (2014).

[71] S. Schnez, K. Ensslin, M. Sigrist, and T. Ihn, *Analytic model of the energy spectrum of a graphene quantum dot in a perpendicular magnetic field*, Phys. Rev. B **78**, 195427 (2008).

[72] M. R. Thomsen and T. G. Pedersen, *Analytical Dirac model of graphene rings, dots, and antidots in magnetic fields*, Phys. Rev. B **95**, 235427 (2017).

[73] M. Grujic, M. Zarenia, A. Chaves, M. Tadic, G. A. Farias, and F. M. Peeters, *Electronic and optical properties of a circular graphene quantum dot in a magnetic field: Influence of the boundary conditions*, Phys. Rev. B **84**, 205441 (2011).

[74] A. Weiße, G. Wellein, A. Alvermann, and H. Fehske, *The kernel polynomial method*, Rev. Mod. Phys. **78**, 275 (2006).

[75] H.-Y. Xu and Y.-C. Lai, *Anomalous in-gap edge states in two-dimensional pseudospin-1 Dirac insulators*, Phys. Rev. Research **2**, 023368 (2020).

[76] H. Suzuura and T. Ando, *Phonons and electron-phonon scattering in carbon nanotubes*, Phys. Rev. B **65**, 235412 (2002).

[77] G. G. Naumis, S. Barraza-Lopez, M. Oliva-Leyva, and H. Terrones, *Electronic and optical properties of strained graphene and other strained 2d materials: a review*, Reports on Progress in Physics **80**, 096501 (2017).

[78] A. L. Kitt, V. M. Pereira, A. K. Swan, and B. B. Goldberg, *Erratum: lattice-corrected strain-induced vector potentials in graphene [phys. rev. b 85, 115432 (2012)]*, Phys. Rev. B **87**, 159909 (2013).

[79] M. Settnes, S. R. Power, and A.-P. Jauho, *Pseudomagnetic fields and triaxial strain in graphene*, Phys. Rev. B **93**, 035456 (2016).

[80] J. Sun, T. Liu, Y. Du, and H. Guo, *Strain-induced pseudo magnetic field in the $\alpha - T3$ lattice*, Phys. Rev. B **106**, 155417 (2022).

[81] A. H. Castro Neto, F. Guinea, N. M. R. Peres, K. S. Novoselov, and A. K. Geim, *The electronic properties of graphene*, Rev. Mod. Phys. **81**, 109–162 (2009).

[82] V. M. Pereira and A. H. Castro Neto, *Strain engineering of graphene's electronic structure*, Phys. Rev. Lett. **103**, 046801 (2009).

[83] J. V. Sloan, A. A. P. Sanjuan, Z. Wang, C. Horvath, and S. Barraza-Lopez, *Strain gauge fields for rippled graphene membranes under central mechanical load: an approach beyond first-order continuum elasticity*, Phys. Rev. B **87**, 155436 (2013).

[84] T. Stegmann and N. Szpak, *Current splitting and valley polarization in elastically deformed graphene*, 2D Materials **6**, 015024 (2018).

[85] W. Ortiz, N. Szpak, and T. Stegmann, *Graphene nanoelectromechanical systems as valleytronic devices*, Phys. Rev. B **106**, 035416 (2022).

[86] D. Giambastiani, F. Colangelo, A. Tredicucci, S. Roddaro, and A. Pitanti, *Electron localization in periodically strained graphene*, Journal of Applied Physics **131**, 085103 (2022).

[87] T. Kitagawa, T. Oka, A. Brataas, L. Fu, and E. Demler, *Transport properties of nonequilibrium systems under the application of light: photoinduced quantum hall insulators without landau levels*, Phys. Rev. B **84**, 235108 (2011).

[88] H. H. Yap, L. Zhou, J.-S. Wang, and J. Gong, *Computational study of the two-terminal transport of floquet quantum hall insulators*, Phys. Rev. B **96**, 165443 (2017).

[89] C. H. Lewenkopf and E. R. Mucciolo, *The recursive green's function method for graphene*, Journal of Computational Electronics **12**, 203–231 (2013).

[90] G. Thorgilsson, G. Viktorsson, and S. Erlingsson, *Recursive green's function method for multi-terminal nanostructures*, Journal of Computational Physics **261**, 256–266 (2014).

[91] W. Magnus, *On the exponential solution of differential equations for a linear operator*, Communications on Pure and Applied Mathematics **7**, 649–673 (1954).

[92] Y. Jiang, T. Low, K. Chang, M. I. Katsnelson, and F. Guinea, *Generation of pure bulk valley current in graphene*, Phys. Rev. Lett. **110**, 046601 (2013).

[93] F. von Oppen, F. Guinea, and E. Mariani, *Synthetic electric fields and phonon damping in carbon nanotubes and graphene*, Phys. Rev. B **80**, 075420 (2009).

[94] M. Jamotte, N. Goldman, and M. Di Liberto, *Strain and pseudo-magnetic fields in optical lattices from density-assisted tunneling*, Commun Phys. **5**, 30 (2022).

[95] M Weinberg, C Staarmann, C Ölschläger, J Simonet, and K Sengstock, *Breaking inversion symmetry in a state-dependent honeycomb lattice: artificial graphene with tunable band gap*, 2D Materials **3**, 024005 (2016).

[96] G. Jotzu, M. Messer, R. Desbuquois, M. Lebrat, T. Uehlinger, D. Greif, and T. Esslinger, *Experimental realization of the topological haldane model with ultracold fermions*, Nature **515**, 237 (2014).

[97] H. Aoki, M. Ando, and H. Matsumura, *Hofstadter butterflies for flat bands*, Phys. Rev. B **54**, R17296–R17299 (1996).

[98] W. Maimaiti, A. Andreanov, H. C. Park, O. Gendelman, and S. Flach, *Compact localized states and flat-band generators in one dimension*, Phys. Rev. B **95**, 115135 (2017).

[99] J.-W. Rhim and B.-J. Yang, *Classification of flat bands according to the band-crossing singularity of bloch wave functions*, Phys. Rev. B **99**, 045107 (2019).

[100] J.-W. Rhim and B.-J. Yang, *Singular flat bands*, Advances in Physics: X **6**, 1901606 (2021).

[101] D. L. Bergman, C. Wu, and L. Balents, *Band touching from real-space topology in frustrated hopping models*, Phys. Rev. B **78**, 125104 (2008).

[102] C.-g. Oh, D. Cho, S. Y. Park, and J.-W. Rhim, *Bulk-interface correspondence from quantum distance in flat band systems*, Communications Physics **5**, 320 (2022).

[103] J.-W. Rhim, K. Kim, and B.-J. Yang, *Quantum distance and anomalous landau levels of flat bands*, Nature **584**, 59–63 (2020).

[104] S. Xia, Y. Hu, D. Song, Y. Zong, L. Tang, and Z. Chen, *Demonstration of flat-band image transmission in optically induced lieb photonic lattices*, Opt. Lett. **41**, 1435–1438 (2016).

[105] J. Li, T. P. White, L. O'Faolain, A. Gomez-Iglesias, and T. F. Krauss, *Systematic design of flat band slow light in photonic crystal waveguides*, Opt. Express **16**, 6227–6232 (2008).

[106] F. D. M. Haldane, *Model for a quantum hall effect without landau levels: condensed-matter realization of the "parity anomaly* , Phys. Rev. Lett. **61**, 2015–2018 (1988).

[107] B. Dey, P. Kapri, O. Pal, and T. K. Ghosh, *Unconventional phases in a haldane model of dice lattice*, Phys. Rev. B **101**, 235406 (2020).

[108] B. Wang, X. Zhou, H. Lin, and A. Bansil, *Higher-order topological insulator phase in a modified haldane model*, Phys. Rev. B **104**, L121108 (2021).

Scientific Contributions

Publications

(a) *Transport and Quantum Coherence in Graphene Rings: Aharonov–Bohm Oscillations, Klein Tunneling, and Particle Localization*, A. Filusch, C. Wurl, A. Pieper and H. Fehske, J Low Temp Phys (2018) 191:259–271

(b) *Resonant scattering of Dirac quasiparticles on oscillating quantum dots*, A. Filusch, C. Wurl and H. Fehske, *Eur. Phys. J. B* (2020) **93**: 59

(c) *Electronic properties of α-$\mathcal{T}_3$ quantum dots in magnetic fields*, A. Filusch and H. Fehske, *Eur. Phys. J. B* (2020) **93**: 169.

(d) *Valley filtering in strain-induced α-$\mathcal{T}_3$ quantum dots*, A. Filusch, A. R. Bishop, A. Saxena, G. Wellein and H. Fehske, *Phys. Rev. B* **103**, 165114 (2021).

(e) *Tunable valley filtering in dynamically strained α-$\mathcal{T}_3$ lattices*, A. Filusch and H. Fehske, *Phys. Rev. B* **106**, 245106 (2022)

(f) *Singular flat bands in the modified Haldane-Dice model*, A. Filusch and H. Fehske, submitted to Physica B: Condensed Matter (March 2023)

Declaration

Hiermit erkläre ich, dass diese Arbeit bisher von mir weder an der Mathematisch-Naturwissenschaftlichen Fakultät der Universität Greifswald noch einer anderen wissenschaftlichen Einrichtung zum Zwecke der Promotion eingereicht wurde.

Ferner erkläre ich, dass ich diese Arbeit selbständig verfasst und keine anderen als die darin angegebenen Hilfsmittel und Hilfen benutzt und keine Textabschnitte eines Dritten ohne Kennzeichnung übernommen habe.

_____
(Alexander Filusch)

Greifswald, 6. März 2023

Acknowledgment

I would like to take this opportunity to thank all those who have accompanied me over the last three and a half years and have significantly contributed to the success of this thesis. I am deeply indebted to Prof. Dr. Fehske for his continuing support, valuable advice and professional guidance throughout the entirety of my studies.

Thanks should also go to Lennard Berg, who contributed to the success of this work by sharing many coffee breaks and productive conversations. Lastly, I would like to recognize my (former) colleagues and friends from AG Fehske and AG Münzenberg, who have always accompanied and supported me. I am also thankful for the hospitality of AG Schweikhard, who gave shelter to a office-less student.

I would remiss in not mentioning my parents, who continued to encourage and support me in any possible way along my Ph.d studies. Finally, my most profound appreciation belongs to my dear girlfriend, who tirelessly strengthens and encourages me, regardless of how difficult the situation is.